Draft version July 23, 2020
Typeset using LaTeX default style in AASTeX62

High Resolution Infrared Spectroscopy of Hot Molecular Gas in AFGL 2591 and AFGL 2136: Accretion in the Inner Regions of Disks Around Massive Young Stellar Objects

Andrew G. Barr,[1] Adwin Boogert,[2,*] Curtis N. DeWitt,[3] Edward Montiel,[3] Matthew J. Richter,[4] John H. Lacy,[5] David A. Neufeld,[6] Nick Indriolo,[7] Yvonne Pendleton,[8] Jean Chiar,[9] and Alexander G. G. M. Tielens[1]

[1] *Leiden University*
Niels Bohrweg 2, 2333 CA Leiden,
The Netherlands
[2] *Institute for Astronomy*
University of Hawaii, 2680 Woodlawn Drive,
Honolulu, HI 96822, USA
[3] *USRA, SOFIA, NASA Ames Research Center,*
MS 232-11, Moffett Field,
CA 94035, USA
[4] *University of California, Davis,*
Phys 539, Davis,
CA 95616, USA
[5] *Department of Astronomy,*
The University of Texas at Austin,
2515 Speedway, Stop C1400, Austin,
TX 78712, USA
[6] *Johns Hopkins University,*
Baltimore,
MD 21218, USA
[7] *ALMA Project,*
National Astronomical Observatory of Japan,
National Institutes of Natural Sciences,
2-21-1 Osawa, Mitaka, Tokyo
181-8588, Japan
[8] *NASA Ames Research Center,*
Moffett Field,
CA 94035, USA
[9] *Diablo Valley College,*
321 Golf Club Rd, Pleasant Hill,
CA 94523, USA

(Accepted July 14, 2020)

Submitted to ApJ

ABSTRACT

We have performed a high resolution 4-13 μm spectral survey of the hot molecular gas associated with the massive protostars AFGL 2591 and AFGL 2136, utilising the Echelon-Cross-Echelle-Spectrograph (EXES) on-board the Stratospheric Observatory for Infrared Astronomy (SOFIA), and the iSHELL instrument and Texas Echelon Cross Echelle Spectrograph (TEXES) on the NASA Infrared Telescope Facility (IRTF). Here we present results of this survey with analysis of CO, HCN, C_2H_2, NH_3 and

Corresponding author: Andrew Barr
barr@strw.leidenuniv.nl

CS, deriving the physical conditions for each species. Also from the IRTF, iSHELL data at 3 μm for AFGL 2591 are presented that show HCN and C_2H_2 in emission. In the EXES and TEXES data, all species are detected in absorption, and temperatures and abundances are found to be high (600 K and 10^{-6}, respectively). Differences of up to an order of magnitude in the abundances of transitions that trace the same ground state level are measured for HCN and C_2H_2. The mid-infrared continuum is known to originate in a disk, hence we attribute the infrared absorption to arise in the photosphere of the disk. As absorption lines require an outwardly decreasing temperature gradient, we conclude that the disk is heated in the mid-plane by viscous heating due to accretion. We attribute the near-IR emission lines to scattering by molecules in the upper layers of the disk photosphere. The absorption lines trace the disk properties at 50 AU where a high temperature gas-phase chemistry is taking place. Abundances are consistent with chemical models of the inner disk of Herbig disks.

Keywords: astrochemistry — ISM: individual objects (AFGL 2591) — ISM: abundances — infrared: ISM — protoplanetary disks — ISM: individual objects (AFGL 2136)

1. INTRODUCTION

Massive star formation begins with the formation of a dense core, a so-called infrared dark cloud (Egan et al. 1998; Carey et al. 1998). This core becomes then gravitationally unstable and collapses, resulting in a central protostar embedded in a dusty cocoon (Zinnecker & Yorke 2007; Tan 2017). Because of excess angular momentum, much of the in-falling material is channeled into an accretion disk, which can feed the central protostar. This disk is heated by viscous dissipation in the mid-plane. For massive stars, hydrogen burning starts already during this accretion phase and the resulting high luminosity heats the gas and dust in the direct environment. This is the so-called Hot Core phase which is rich in complex organic molecules (van der Tak 2003; Beuther et al. 2007; Herbst & van Dishoeck 2009). Eventually, when the central star is hot enough to create ionising photons, a hyper compact HII region will form in the inflating material. Once the cocoon is thin enough, the ionising photons can escape, leading to the ultracompact and compact HII region phases (Beuther et al. 2007).

From an observational perspective, the understanding of these stages is hindered on several accounts. Distances to the nearest massive stars are larger than for low mass stars, meaning that higher angular resolution is required to study them at comparable physical scales as their low mass counterparts (Henning et al. 2002). Furthermore dust extinction is high ($\sim A_v = 200$) as massive stars remain deeply embedded in their natal envelope for a large fraction of their early evolution (Beuther et al. 2007). A 40 $M_\odot$ star will live for around a few million years with an embedded lifetime of around $1{\times}10^5$ yr. This contrasts to low mass stars that have an embedded lifetime of around 10^6 yr but a main sequence lifetime of over 10^9 yr. Therefore it is challenging to disentangle the protostar and its direct environment - circumstellar disk, hot core and surrounding molecular cloud (Zinnecker & Yorke 2007; Cesaroni et al. 2007).

During the star formation process, infalling material onto the central protostar forms a disk, with a bipolar outflow along the perpendicular axis (Zinnecker & Yorke 2007). Angular momentum is transported to the outer parts of the disk via viscous stresses and gravitational torques, and the disk expands (Lynden-Bell & Pringle 1974; Cassen & Summers 1983; Dullemond et al. 2007). As a result of this, material moves inward and accretes onto the central protostar. Theoretical models of dust disks come in varying degrees of complexity. One such model combines a hot, flared dust surface layer heated by stellar radiation, and viscous dissipation of gravitational energy due to accretion (D'Alessio et al. 1998). In this model one can see that for high accretion rates (10^{-7} - $10^{-6} M_\odot$/yr), three regimes arise in the disk. The surface region is irradiation dominated, the midplane of the disk is accretion dominated, and the two are connected by an intermediate zone. Here two temperature gradients can be distinguished, with an outwardly decreasing temperature gradient in the vertical direction in the accretion dominated region, and an inwardly decreasing temperature gradient in the vertical direction in the irradiation dominated zone (Dullemond et al. 2007).

Whilst disks around forming low mass young stellar objects (YSOs) are common (Williams & Cieza 2011), the number of detected disks around massive stars remains constrained to a handful, especially in the case of O-type stars (Patel et al. 2005; Kraus et al. 2010; Moscadelli & Goddi 2014; Johnston et al. 2015; Ilee et al. 2016; Moscadelli et al. 2019; Zapata et al. 2019; Maud et al. 2019). Commonly detected around massive stars are massive rotating toroids

* Staff Astronomer at the Infrared Telescope Facility, which is operated by the University of Hawaii under contract NNH14CK55B with the National Aeronautics and Space Administration.

likely to host stellar clusters (Cesaroni 2005; Sandell et al. 2003; Olmi et al. 2003; Beltrán et al. 2004; Sollins et al. 2005). The search for disks around O-B stars is undertaken with sub-millimetre (sub-mm) continuum or specific line tracers and infrared (IR) continuum/line observations, as well as maser studies, in order to penetrate the surrounding obscuring dust in these embedded regions. Sub-mm observations probe preferentially the outer parts of the disk and the envelope, while IR observations are sensitive to the innermost regions of the disk (Cesaroni et al. 2007; Dullemond et al. 2007). Inner regions of TTauri and Herbig disks are observed in molecular *emission* such as CO and H_2O at IR wavelengths (Mandell et al. 2012; Bast et al. 2013, 2011; Pontoppidan et al. 2011, 2019; Setterholm et al. 2019; Adams et al. 2019). These disks are illuminated by UV radiation from the central protostar under an irradiation angle, resulting in a PDR-like layered structure (Tielens & Hollenbach 1985), with a temperature gradient that decreases towards the mid-plane. The inner portions of massive disks have been studied mainly through atomic line and CO bandhead *emission* (Cooper et al. 2013; Ilee et al. 2013; Davies et al. 2010; Bik et al. 2006; Fedriani et al. 2020). In a survey of massive protostars, Ilee et al. (2013) model CO bandhead emission from 20 massive YSOs and find temperatures and densities consistent with emission from an accretion disk, close to the dust sublimation radius. For a further discussion on the inner regions of protoplanetary disks, see the review by Dullemond & Monnier (2010).

Observations of ro-vibrational lines in the mid-infrared (MIR) regime of star forming regions offer a unique view. Towards massive YSOs these lines are typically seen in absorption rather than emission. Since the IR source is very small, a very high angular resolution is achieved, comparable to the highest possible obtainable with emission studies (≈50mas). Furthermore, since the lines lie so close together, it is possible to observe many of these lines in one observational setting. Further details about studies of ro-vibrational lines at IR wavelengths can be found in Lacy (2013) along with the various issues that these kind of observations face. Finally, we emphasise that IR studies allow observations of CH_4, C_2H_2 and CO_2 that have no allowed rotational spectrum in the sub-mm.

We have carried out a high spectral resolution spectral survey of the 4-13 μm region towards AFGL 2591 and AFGL 2136. This article is an follow-up of a previous study (Barr et al. 2018) where we reported IR observations of CS in absorption towards the hot core AFGL 2591 VLA 3. Here we extend the discussion to other species detected in our spectra of AFGL 2591 VLA 3, as well as those in the hot core AFGL 2136 IRS1. In section 2 we present the observational details of the spectral survey, in section 3 we outline the analysis techniques used and section 4 contains the results for each molecular species identified. Section 5 discusses the results in the context of the physical structures of the sources, along with the origin of L-band emission lines and the calculation of the abundances. Finally the chemical implications are discussed as well as extending the discussion to other infrared studies of massive protostars.

2. OBSERVATIONS AND DATA REDUCTION

2.1. *Target Sources*

AFGL 2591 is a star forming region in the Cygnus X region, at coordinates $\alpha(J2000)$ = 20:29:24.8, $\delta(J2000)$ = +40:11:19.6. It is home to the massive protostar AFGL 2591 VLA 3 (hereafter AFGL 2591) which has a luminosity of 2×10^5 $L_\odot$ at a distance of 3.33±0.11 kpc (Rygl et al. 2012). It is an O-type star with a mass of ∼40 $M_\odot$ (Sanna et al. 2012) and powers a bipolar outflow seen in CO and H_2 (Bally & Lada 1983; Mitchell et al. 1991; Tamura & Yamashiti 1992). Radio continuum emission is observed at 3.6 cm and 1.3 cm towards AFGL 2591 which coincides with a cluster of maser emission in a helical shell around the outflow (Trinidad et al. 2003).

AFGL 2136 IRS1 is an O-type star and is the main IR source, in the star forming region of AFGL 2136, coordinates $\alpha(J2000)$ = 18:22:26.385, $\delta(J2000)$ = -13:30:11.97. The luminosity of AFGL 2136 IRS1 (hereafter AFGL 2136) is 1×10^5 $L_\odot$ at a distance of 2.2 kpc (Lumsden et al. 2013; Urquhart et al. 2012, 2014). AFGL 2136 is one of the few sources that has a clear signature of a Keplerian disk around a proto-O-type star (Maud et al. 2019) with a bipolar outflow in the perpendicular direction to the disk. There is also evidence for a disk wind from Brγ emission and SiO line emission (Murukawa et al. 2013; Maud et al. 2018). The surrounding environment of AFGL 2136 consists of a bipolar reflection nebula in a fan shape (Murakawa et al. 2008) and has deep ice bands associated with ice located in the envelope (Gibb et al. 2004).

2.2. *EXES*

AFGL 2591 and AFGL 2136 were observed with the EXES spectrometer (Richter et al. 2018) onboard the Stratospheric Observatory for Infrared Astronomy (SOFIA) flying observatory (Young et al. 2012) as part of SOFIA program 05_0041. In the full spectral survey of AFGL 2591 and AFGL 2136, EXES covered the range 5.5-8 μm and required 16 wavelength settings in its HIGH-LOW mode, where the high-resolution echelon grating is cross-dispersed with the R

1/2 LOW resolution echelle grating. For AFGL 2136, observations were taken over three EXES flight series. For the analysis in this paper, 8 spectral settings were used, covering wavelengths 6.7-8.0 μm (1249cm^{-1} - 1494cm^{-1}). These observations are summarised in Table 1. The slit width was 3.2″ for all settings, providing R=55,000 resolution. The fixed slit lengths used were either 3.1″ or 2.2″, depending on the wavelength setting. In order to remove background night sky emission and telescope thermal emission, the telescope was nodded to an off-source position 15″ away from the target coordinates every 1-2 minutes.

The EXES data were reduced with the SOFIA Redux pipeline (Clarke et al. 2015), which has incorporated routines originally developed for the Texas Echelon Cross Echelle Spectrograph (TEXES) (Lacy et al. 2003). The science frames were de-spiked and sequential nod positions subtracted, to remove telluric emission lines and telescope/system thermal emission. An internal blackbody source was observed for flat fielding and flux calibration and then the data were rectified, aligning the spatial and spectral dimensions. The wavenumber solution was calibrated using sky emission spectra produced for each setting by omitting the nod-subtraction step. We used wavenumber values from HITRAN (Rothman et a. 2013) to set the wavelength scale. The resulting wavelength solutions are accurate to 0.3 kms^{-1}. Where necessary, lines were divided by a local continuum which was fit as a straight line over the transition. This was done in cases where the continuum was uncertain due to fringing or poor atmospheric correction.

2.3. *TEXES*

Spectra were obtained of HCN, C_2H_2, and NH_3 from spectral surveys made with TEXES (Lacy et al. 2002). AFGL 2136 was observed with the Gemini North telescope on 2017 March 17 and 18 (UT) in the TEXES hi-lo spectral mode. In this mode the high resolution echelon grating is cross dispersed with a first order grating, providing a spectral coverage of $\delta\lambda \approx 0.25\mu m$ with typically 20-30 echelon spectral orders. To prevent order overlap on the detector array a short slit was required, which necessitated nodding the source off of the slit to observe the sky background. Between the two nights the 782-904 cm^{-1} region was covered with a total telescope time of 3^h 30^m including time for source acquisition, spectral setups, flat fields, nod delays, and sky observations. The on-source time at each spectral setting was typically 130 s, with some settings extended if clouds interfered. On the night of 2017 March 20 the spectral region of 1157-1195 cm^{-1} was observed in the TEXES hi-med spectral mode, in which the echelon is cross dispersed with an echelle, which was used in 6^{th} order. In this mode the spectral coverage in each setting is less, with $\delta\lambda \approx 0.006\lambda$, but a longer slit can be used so that the source can be nodded along the slit, improving the observing efficiency. The total telescope time was 40^m, and the on-source time at each spectral setting was 260 s. The data are publicly available from the Gemini archive.

AFGL 2591 was observed with TEXES on the NASA Infrared Telescope Facility (IRTF) on 2018 July 7 and 8, and 2018 Sep. 29 and 30. The 728-849 cm^{-1} spectral region was covered on July 7, the 849-999 cm^{-1} region was covered on July 8, and the 727-905 cm^{-1} region was covered on Sep. 18. These observations were in the TEXES hi-lo mode, with a total telescope time of 9^h and an on-source time per spectral setting of 130 s. The 1107-1120 cm^{-1} region was covered on July 8, the 1227-1250 cm^{-1} region on July 12, and the 751-841 cm^{-1} region on Sep. 30, all in hi-med mode. The total telescope time for these observations was 9^h 10^m. The on-source time per spectral setting was 972 s on July 8 and 12, and 583 s for most Sep. 30 observations, except that additional time was spent when clouds interfered.

No comparison sources for correction of telluric and instrumental features were available without spectral features and at least comparable in flux to the primary targets. Consequently, the observed spectra were divided by spectra of an ambient temperature black body and a model of the telluric absorption. The telluric model was based on measurements of atmospheric pressure, temperature, and water vapour from a weather balloon launched from Hilo each night and spectral parameters from the HITRAN database. The balloon data are available from the National Centres for Environmental Information Integrated Global Radiosonde Archive (IGRA) at ncdc.noaa.gov. The HITRAN database is available from cfa.harvard.edu. The atmospheric ozone is measured less frequently, and the measurement closest to the observation dates were used. They are available from the NOAA Earth System Research Laboratories at esrl.noaa.gov. The water vapour and ozone abundances in the telluric model were adjusted to give the best correction and the best fit to the observed telluric emission spectrum. Most spectral lines were corrected well, but instrumental fringing was not always removed as well, so the corrected spectra were divided by a polynomial baseline.

2.4. *iSHELL*

AFGL 2591 and AFGL 2136 were observed with iSHELL (Rayner et al. 2016) at the IRTF telescope on Maunakea at a spectral resolving power of 80,000. The observations are summarised in Table 1. The observations for AFGL 2591

were described in (Barr et al. 2018). AFGL 2136 was observed on UT 2018-10-10 from 05:45 to 06:52 at an airmass range of 1.55-1.80, during moderate weather conditions as part of program 2018B095. The target was nodded along the 15″ long slit to be able to subtract background emission from the sky and hardware. Spectra affected by clouds were discarded inthe data reduction. iSHELL's internal lamp was used to obtain flat field images. The spectra were reduced with the Spextool package version 5.0.1 (Cushing et al. 2004). Correction for telluric absorption lines was not done with a standard star but with the program Xtellcor model developed at the IRTF and makes use of the atmospheric models calculated by the Planetary Spectrum Generator (Villanueva et al. 2018). The Doppler shift of AFGL 2136 at the time of the observations was +37 kms^{-1} (including an assumed VLSR=+23 kms^{-1}), and thus telluric and target CO lines are well separated. The blaze shape of the echelle orders was corrected for using the flat fields. The continuum signal-to-noise ratio as measured from the scatter in the data points is ∼250 at the native sampling of 3 pixels per resolution element. AFGL 2591 was also observed with iSHELL's L1, L2, and L3 modes at R=80,000 on UT 2018-10-05 at 04:42-08:52 as part of program 2018B095. The airmass range was 1.08-1.20. The data reduction process was the same as for the M-band, although standard stars were used for the telluric absorption correction: BS 8830 (L1), and Vega (L2+L3). The continuum signal-to-noise values between the telluric lines ranges from ∼220 in L1 to ∼400 in the L2 and L3 modes. The Doppler shift of AFGL 2591 at the time of the L-band observations was -13 kms^{-1} (including an assumed VLSR=-6 kms^{-1}).

Table 1. Summary of Observations

Source	Telescope	Instrument	Date (UT)	Wavelength Range (μm)	Instrument Mode	Slit Width (″)	Resolving Power	Integration Time (min)
AFGL 2591	IRTF	iSHELL	2017-07-05	4.51-5.24	M1 & M2	0.375	80,000	51
	IRTF	iSHELL	2018-10-05	2.750-3.459	L1, L2 & L3	0.375	80,000	93
	SOFIA	EXES	2017-03-17	7.34-7.68	High-low	3.2	55,000	30
	SOFIA	EXES	2017-03-21	6.69-7.05	High-low	3.2	55,000	20
	SOFIA	EXES	2017-03-22	7.19-7.37	High-low	3.2	55,000	14
	SOFIA	EXES	2017-03-23	7.67-8.01 & 7.02-7.21	High-low	3.2	55,000	25
	IRTF	TEXES	2018-07-08	8.93-9.03	High-med	1.4	85,000	65
	IRTF	TEXES	2018-07-12	8-8.15	High-med	1.4	85,000	32
	IRTF	TEXES	2018-09-30	11.89-13.32	High-med	1.4	85,000	185
AFGL 2136	IRTF	iSHELL	2018-10-10	4.51-5.24	M1 & M2	0.375	80,000	42
	SOFIA	EXES	2017-03-17	7.34-7.69	High-low	3.2	55,000	53
	SOFIA	EXES	2017-03-21	6.69-6.88	High-low	3.2	55,000	43
	SOFIA	EXES	2017-03-23	7.67-7.85 & 8.87-7.05	High-low	3.2	55,000	90
	SOFIA	EXES	2017-05-25	7.19-7.37	High-low	3.2	55,000	30
	SOFIA	EXES	2019-04-24	7.83-8.01	High-low	3.2	55,000	36
	SOFIA	EXES	2019-04-26	7.19-3.37	High-low	3.2	55,000	41
	Gemini	TEXES	2017-03-17 to 2017-03-18	11.06-12.79	High-low	1.4	85,000	15
	Gemini	TEXES	2017-03-20	8.37-8.64	High-med	1.4	85,000	22

3. ANALYSIS

The detected absorption lines were fitted with one Gaussian line profile for each velocity component detected. The free parameters that were allowed to vary were the line strength, line width, line velocity and continuum level. The fitting was conducted in velocity space, therefore the fit was a function of the local standard of rest (LSR) velocity and full width at half maximum (FWHM) both in units of kms^{-1}. The fit was then converted into an optical depth profile, and then into a column density profile via:

$$\tau(v) = -\ln(flux/cont) \tag{1}$$

followed by,

$$\frac{dN_l}{dv} = \tau(v)\frac{g_l}{g_u}\frac{8\pi}{A\lambda^3} \tag{2}$$

where $\tau(v)$ is the optical depth profile as a function of velocity, g_l and g_u are the statistical weights of the lower and upper states respectively, A is the spontaneous emission coefficient for the transition and λ is the wavelength. The fit was then integrated in velocity space to derive a column density in the lower energy level of the transition.

Each state-specific column density was then plotted in a rotation diagram by plotting $\ln(N_l/g_l)$ against E_l, where N_l is the integrated column density in each transition and E_l is the energy of the lower level in Kelvin. The rotational temperature is given by the Boltzmann equation:

$$\ln \frac{N_l}{g_l} = \ln N - \ln Z(T) - \frac{E_l}{kT} \tag{3}$$

where the temperature is -1/gradient of the fit to the rotation diagram. Here Z is the partition function at the rotational temperature and N is the total column density of the species. In this way the excitation temperature of each species was calculated. Initially, column densities were calculated for both absorption and emission lines. However a more extensive analysis of the absorption lines was carried out using stellar atmosphere theory to calculate the abundances with respect to H, assuming a dust/H ratio, and this utilised the excitation temperatures derived from the initial rotation diagrams. The analysis process is discussed further in section 5.2. Results from the rotation diagram analysis are presented in Tables 2 & 3 and parameters of the gaussian fitting are given in Tables 4 and 5 in the Appendix.

The rotational diagrams reveal different behaviour for the low and high J lines. Averaged line profiles were obtained for high and low energy lines by the mathematical averaging of all normalised, unblended lines of a given species. The distinction between high and low energy was taken as low energy lines having $E_l \leq 90$ K. The weighted average of the line profiles was taken to give the average line profiles which are presented in Figures 1 and 2.

4. RESULTS

Line widths and centroid velocities quoted in this section are given as weighted averages for the lines detected of a given band. The line widths have been corrected for the resolving power of the different instruments used. In all cases, missing lines of a band are either lost in the wings of deep telluric lines, blended with other hot core lines or additionally, in the case of TEXES data, lost in order gaps. Some lines are affected by systematic error such as proximity to other hot core lines or poor baselines due to fringing or poor atmospheric correction. This makes it harder to put a constraint on the continuum of such lines. The result is that these lines exhibit a greater error in line parameters than that which is portrayed by the fitting routine.

Also, for the TEXES data, it can be the case that lines lie close to the edge of gaps between orders. Therefore these lines will be slightly underproduced as some of their flux gets lost at the edges of the detector. For the TEXES data of AFGL 2591, additional systematic errors affect the data such as spurious emission wings on the shoulders of absorption lines due to the removal of strong fringing, and also CO_2 atmospheric residuals beyond around 13 μm.

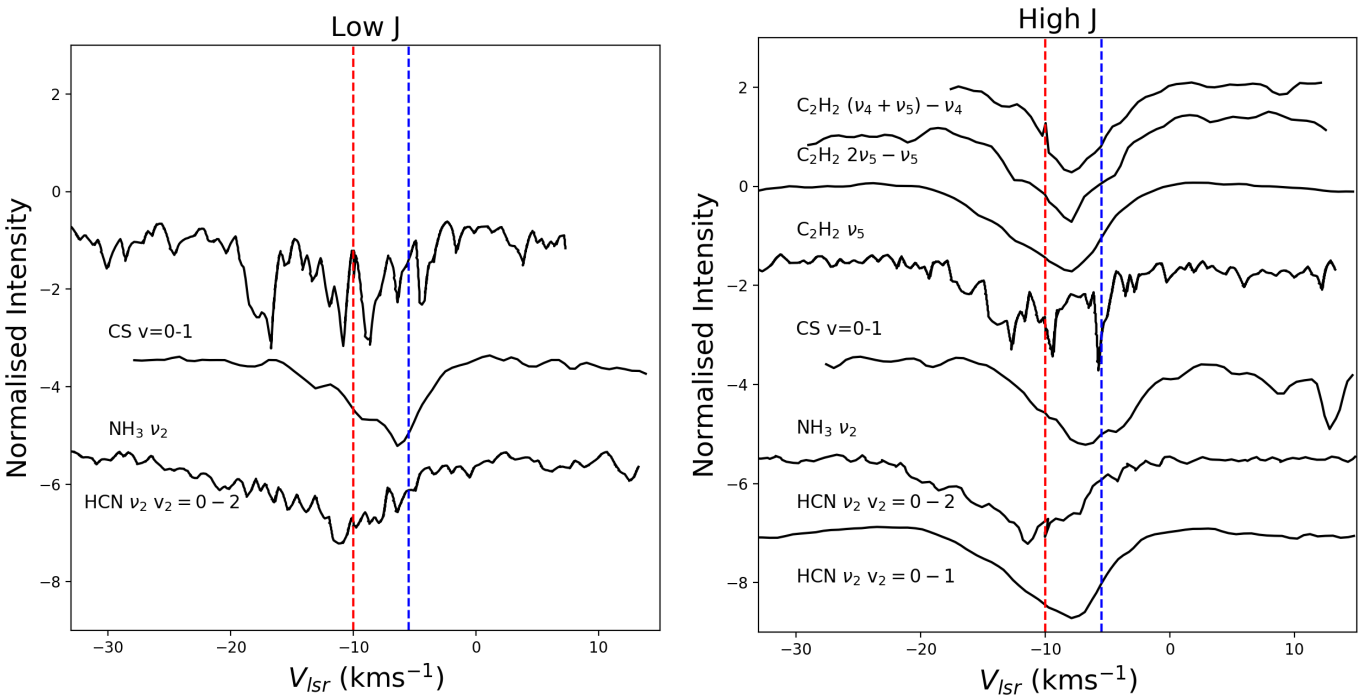

Figure 1. Normalised average line profiles for each band detected in AFGL 2591 plotted against the LSR velocity. Transitions are separated into high and low J levels before the average is calculated (high for E_l > 90 K). To guide the eye, we mark $v_{lsr} = -10$ km/s with a red dashed line in both panels. The blue dashed line denotes the systemic velocity of the source which is -5.5 kms^{-1}. CS and HCN v$_2$ = 0 − 2 transitions are detected with EXES at 7 μm whilst the other bands/species are detected with TEXES at 13 μm.

4.1. *AFGL 2591*

4.1.1. *CO*

AFGL 2591 shows a complex structure, with five velocity components of ^{13}CO detected. The scope of this paper will cover only the -10 kms^{-1} component, which has been previously discussed by Barr et al. (2018). These results are in agreement with a previous IR study of CO carried out by (Mitchell et al. 1989). We do not discuss the ^{12}CO v=0-1 transitions as they are saturated up until J=9. The rotation diagram for ^{13}CO at -10 kms^{-1} is shown in Figure 3. Furthermore, vibrationally excited ^{12}CO is detected with a single temperature component at -10 kms^{-1}, and we derive a vibrational temperature of 623±292 K. A comparison of line profiles from low and high J level is displayed in Figure 3 and detected unblended transitions of ^{13}CO v=0-1 and ^{12}CO v=1-2 are presented in Figure 4.

The rotation diagram of ^{13}CO in Barr et al. (2018) and Mitchell et al. (1989) shows two temperature components at -10 kms^{-1}. These two temperature components are also distinct physical components. This can be seen by comparing low and high J transitions around the dashed line in Figure 3. The line profile of the R(3) line is dominated by a narrow velocity component with a width of 1.5 kms^{-1} and peak velocity of -9.2 kms^{-1}. This component disappears past J=6 which is reflected in the R(9) transition (Fig 3) where we see a broad component uncovered with a width of 10.5 kms^{-1} centred on a velocity of -12 kms^{-1}. The temperatures of the narrow and broad components are 49 K and 671 K, respectively. Therefore we only show the hot component in the rotation diagram in Figure 3 and discuss only the high temperature component in the rest of the paper, the temperature of which is consistent with that of other species at the same velocity.

4.1.2. *CS*

CS is detected towards AFGL 2591 and has been discussed extensively by Barr et al. (2018). One velocity component is detected around -10 kms^{-1} and corresponds with one of the velocity components of ^{13}CO and the velocity of vibrationally excited ^{12}CO. Figure 5 shows that the rotation diagram reveals a CS temperature of 714±59 K which is

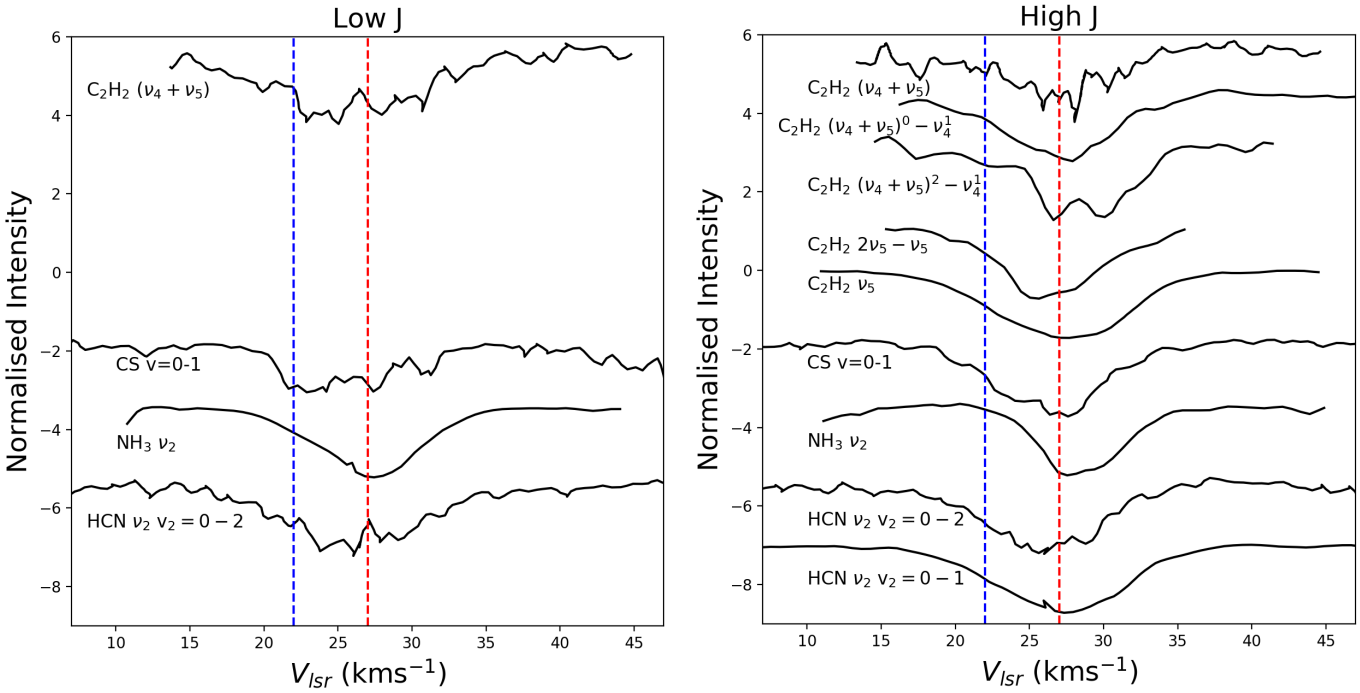

Figure 2. Normalised average line profiles for each band detected in AFGL 2136 plotted against the LSR velocity. Transitions are separated into high and low J levels before the average is calculated (high for $E_l > 90$ K). To guide the eye, we mark $v_{lsr} = 27$ km/s with a red dashed line in both panels. The blue dashed line denotes the systemic velocity of the source which is 22 kms^{-1} (van der Tak et al. 2003). CS, HCN $v_2 = 0-2$ and C_2H_2 ($\nu_4+\nu_5$) transitions are detected with EXES at 7 μm whilst the other bands/species are detected with TEXES at 13 μm. NH_3 transitions are detected from 10 to 13 μm.

consistent with the hot component of ^{13}CO at -10 kms^{-1} and ^{12}CO v=1-2. Line widths are in agreement for CS and hot ^{13}CO for equivalent energy level. Therefore CS and CO trace the same region of the hot core.

4.1.3. *HCN*

20 lines of the ν_2 band of HCN are detected in the v_2=0-1 transition with TEXES, spanning an energy range of 2500 K. From the rotation diagram, we derive a high temperature of 675±32 K. All line profile parameters are summarised in Tables 2 and 3.

A second vibrational transition of HCN is detected at shorter wavelengths with EXES, the v_2=0-2 transition in the ν_2 band. From the 22 lines, the rotation diagram reveals the presence of a temperature gradient (Figure 6) by a curving of the rotation diagram at low J level, as line profiles are consistent from low to high J (Fig 1). Thus the physical conditions derived from the rotation diagram may not be reflective of the true values for this species. This is observed in the v_2=0-2 transition of HCN while it is not seen in the v_2=0-1 transition. This may be because, in the v_2=0-1 transition, only lines with J≥7 are observed as our observations did not extend to long enough wavelengths. As no low J transitions are observed in the HCN v_2=0-1 band, we cannot ascertain the presence (or absence) of an upward curvature in the rotation diagram. Due to the non-linearity of the rotation diagrams, we derive physical conditions from a fit to the flat, or high energy, part of the rotation diagram. A temperature of 670±118 K is found, in good agreement with the rotational temperature derived for the v_2=0-1 transition of HCN, as well as CS and CO. The line widths of CO, CS and HCN are also in agreement.

The column density measured in the v_2=0-2 transition at 7 μm is larger than the column density of the v_2=0-1 transition at 13 μm by one order of magnitude, despite the fact that these two transitions both trace the ground state. Compared to the v_2=0-1 transition, the line widths agree but the velocity is blue-shifted by a few kms^{-1}, which is around the instrumental spectral resolution.

The R(0) line in the HCN v_2=0-2 band is offset in velocity from the other HCN lines and appears to be tracing cold foreground absorption. Hot HCN has been detected towards AFGL 2591 before via MIR absorption with Infrared Space

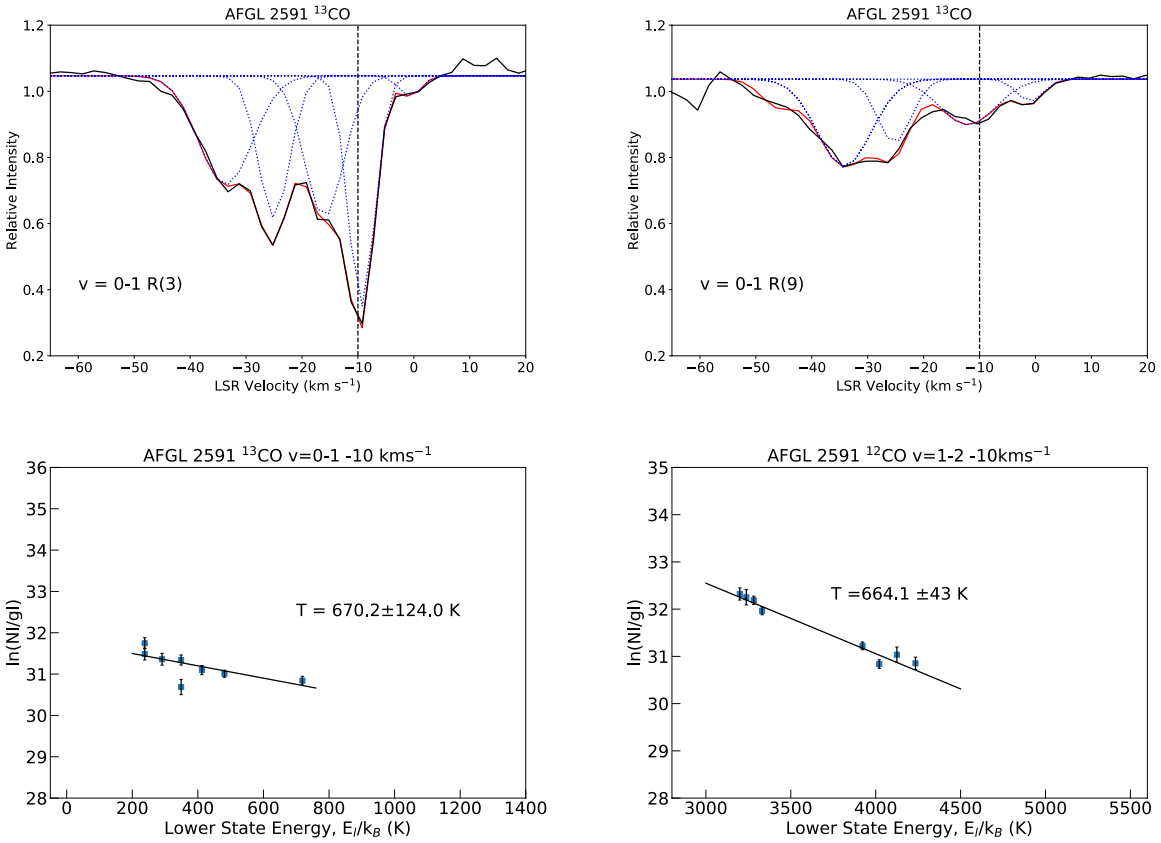

Figure 3. Individual line profiles for a high J (right) and low J (left) transition of ^{13}CO for AFGL 2591 detected with iSHELL at 4.5 μm. Blue dotted lines represent the individual gaussian fits and the red solid line is the overall fit. The black dashed line denoted -10 kms^{-1}. Rotation diagrams of ^{13}CO v=0-1 and ^{12}CO v=1-2 are also shown for the -10 kms^{-1} velocity component.

Observatory Short Wavelength Spectrometer (ISO-SWS) (Lahuis & van Dishoeck 2000). The derived temperature of 650^{+75}_{-50} K is in agreement with what we find at high spectral resolution.

HCN has also been detected in emission in the L-band spectrum of AFGL 2591. 21 lines tracing the ν_1 band are detected and the rotation diagram is also plotted in Figure 6. The velocity and line width are not in agreement with the HCN in absorption. The rotation diagram reveals a temperature of only 240±13 K, lower than the other two transitions seen in absorption.

4.1.4. *C_2H_2*

Several bands of C_2H_2 have been detected in AFGL 2591 with TEXES. Rotation diagrams have been constructed using statistical weights from the HITRAN database, which incorporates a factor of 3 difference between the statistical weights for the ortho- and para- states, due to nuclear spin degeneracy. Therefore the statistical weights of para- lines are 2J+1 however the statistical weights of the ortho- lines are 3(2J+1). We also use the partition function, Q, given in HITRAN, and incorporate the difference in statistical weights by taking Q(ortho) = 3/4 Q and Q(para) = 1/4 Q. Ortho- and para- states have been split up and treated as separate molecular species. All line parameters are summarised in Tables 2 and 3.

In AFGL 2591, 26 lines of the ν_5 fundamental band of C_2H_2 are detected. The temperature ($\simeq$ 600 K) derived from the rotation diagrams is consistent with the other species. This suggests that o-C_2H_2 and p-C_2H_2 in this band come from the same part of the hot core. We derive an apparent ortho-to-para ratio (OPR) of 2.1±0.3, and this will be discussed further in section 5.2. The ortho- lines are seen up to higher J level, which is reflected in the rotation diagram.

Two vibrationally excited bands of C_2H_2 are marginally detected in AFGL 2591, the $(\nu_4+\nu_5)^2-\nu_4^1$ and the $2\nu_5^2-\nu_5^1$ band, probing the ν_4 and ν_5 levels respectively. The rotation diagrams are shown in Figure 7. For the $(\nu_4+\nu_5)^2-\nu_4^1$

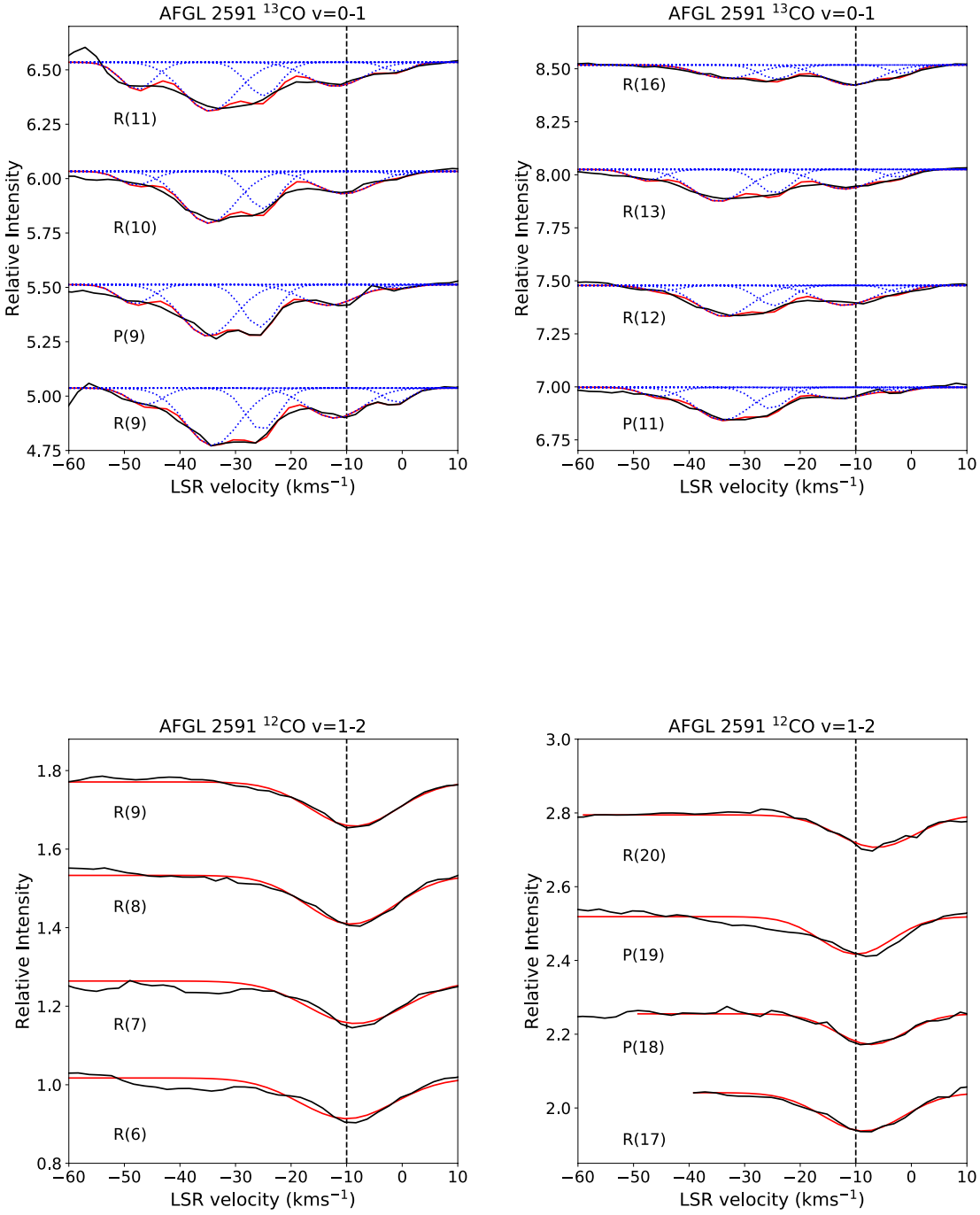

Figure 4. Lines of ^{12}CO v=1-2 and high J ^{13}CO v=0-1 in AFGL 2591 detected with iSHELL at 4.5 μm. The blue dotted lines represent the individual velocity components and the red solid lines show the overall fit. The black dashed line denotes -10 kms^{-1}.

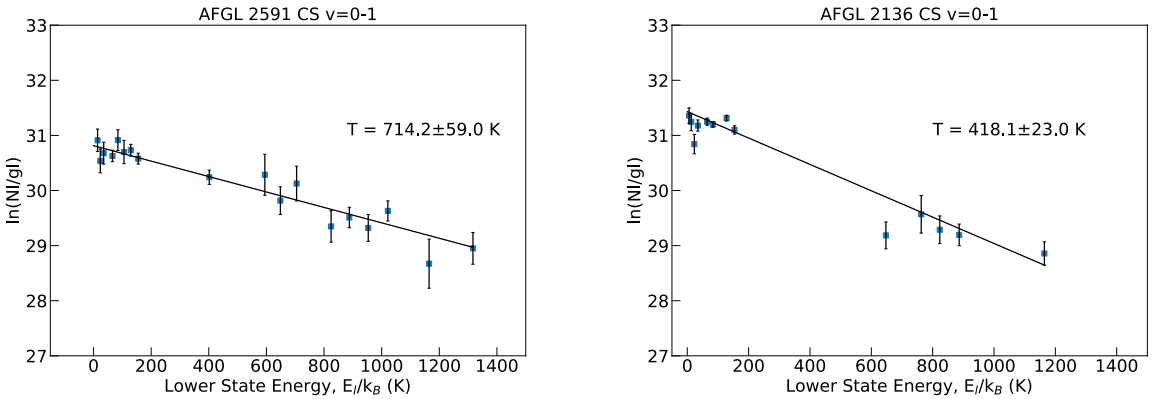

Figure 5. CS rotation diagrams for transitions in AFGL 2591 and AFGL 2136 detected with EXES. Rotational temperatures are shown.

band, the line widths of p-C_2H_2 and o-C_2H_2 agree well however the velocity of p-C_2H_2 is slightly lower than o-C_2H_2. The parameters derived for this band have a large uncertainty due to the weakness of the lines.

For the vibrationally excited $2\nu_5 - \nu_5$ band, we only observe o-C_2H_2 lines. We derive a rotational temperature of 596 K, in good agreement with the rotational temperature for the ν_5 band. The line profiles of this vibrationally excited band are consistent with those of the ν_5 fundamental band.

The $\nu_2 + (\nu_4 + \nu_5)$ band of C_2H_2 was detected in emission in the L-band towards AFGL 2591. The lines are narrower than the other C_2H_2 lines we observe in absorption by 4 kms^{-1}. Also, the velocity is clearly offset from the v_{lsr} of other species. The rotation diagram is shown in Figure 7. The rotation diagram gives a temperature of 454±151 K. Only o-C_2H_2 is detected in emission as the p-C_2H_2 lines are too weak.

The blended Q-branch of hot C_2H_2 has been detected in AFGL 2591 with ISO-SWS Lahuis & van Dishoeck (2000). The derived excitation temperature (900 K) is higher than what we observe with TEXES (Table 2). This may reflect the limited spectral resolution of ISO-SWS - hampering extraction of physical conditions from this blended line - and the severe fringing inherent to this instrument.

4.1.5. *NH_3*

For NH_3, we also treat ortho- and para- states as separate molecular species. We also take different partition functions as in the case for C_2H_2. For NH_3 the ortho states have K as a multiple of 3, and the para states have K=3n±1. The statistical weights of the o-NH_3 lines are a factor of 2 higher than the p-NH_3 lines (Šimečková et al. 2006). Since there are twice as many options for J for para states, this results in an equal number of ortho and para molecules. Thus we implement the partition functions as Q(ortho) = Q(para) = Q/2, where Q is the partition function for NH_3 given in HITRAN. For NH_3 the value of the OPR for high temperatures is equal to 1 (Faure et al. 2013).

For AFGL 2591, NH_3 is harder to detect than in AFGL 2136. This reflects the poorer data quality due to fringing and lower signal to noise. AFGL 2136 was observed with TEXES on Gemini and used Orion BN as a standard star to improve atmospheric and standing wave correction, while AFGL 2591 was observed with the IRTF without a standard star. Since the temperature that we measure for NH_3 gas is hotter than in AFGL 2136, the energy spreads out over more, weaker transitions. Then, since the column densities of NH_3 derived for the two sources are the same, the lines in AFGL 2591 will be weaker than those in AFGL 2136.

Both o-NH_3 and p-NH_3 lines are detected in the v_2=0-1 transition of the ν_2 band. The peak velocities are in agreement, however the line width of o-NH_3 is almost twice as large as p-NH_3. Temperatures are in agreement and a high temperature of around 875 K is derived. An OPR=1±0.4 is found for AFGL 2591, consistent with the high rotational temperature. The rotation diagram is shown in Figure 8.

4.2. *AFGL 2136*

4.2.1. *CO*

AFGL 2136 shows a much simpler morphology compared to AFGL 2591, with only two velocity components of CO observed, which correspond to two separate physical components. For ^{13}CO, one velocity component is detected at

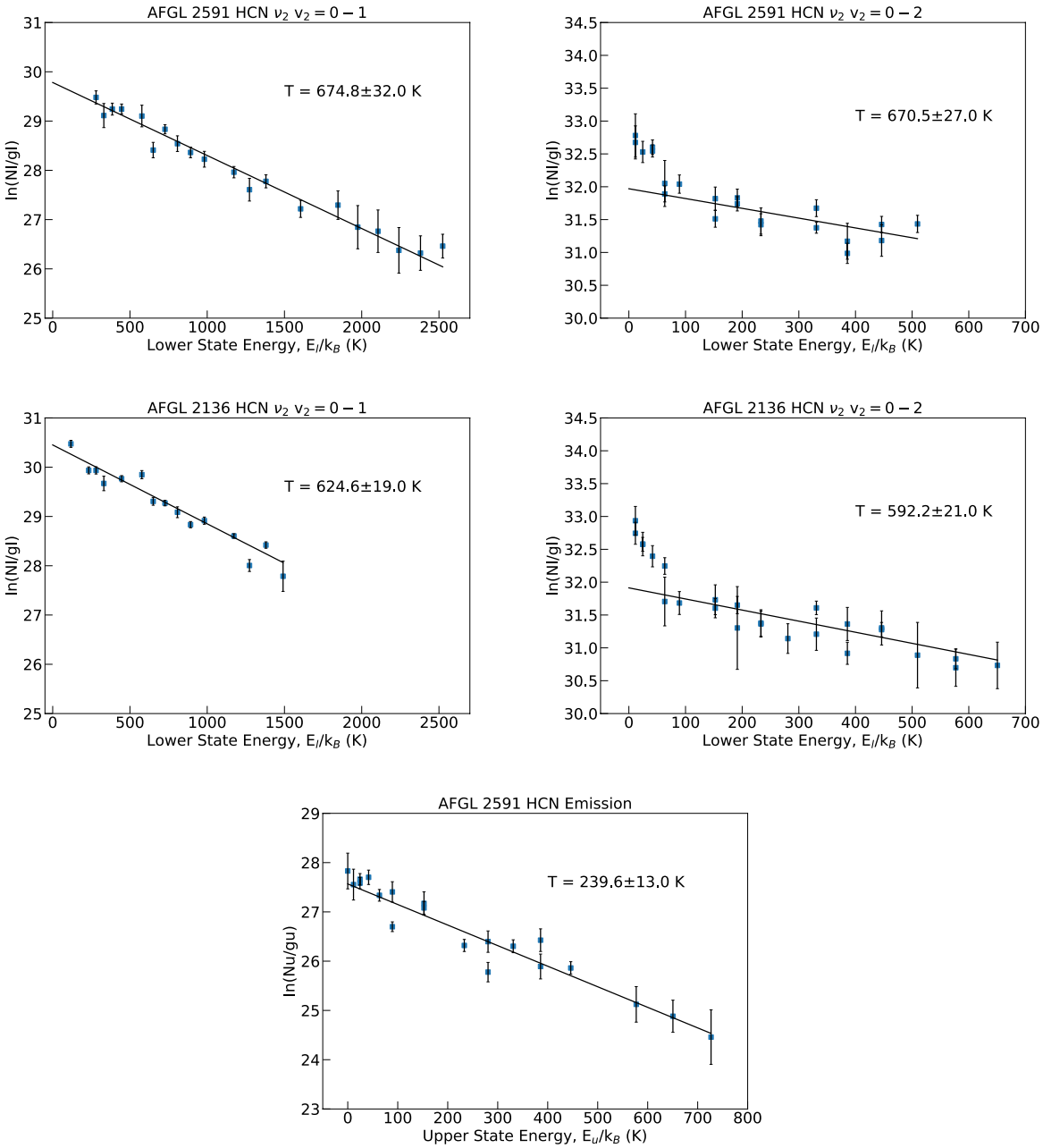

Figure 6. HCN rotation diagrams for AFGL 2591 and AFGL 2136. The v_2=0-1 transition is detected at longer wavelengths with TEXES. The v_2=2-0 transition comes from the EXES data. The rotation diagram for the HCN ν_1 band seen in emission is also shown which is detected with iSHELL.

22.3±0.2 kms^{-1} with a line width of 3.4±0.7 kms^{-1}. This velocity component is superimposed on a broader underlying velocity component centred at 26.5±0.3 kms^{-1}, which has a width of 13.2±0.9 kms^{-1}. In C^{18}O, the narrow and broad velocity components are also observed, with line widths and velocities consistent with ^{13}CO. ^{12}CO v=0-1 lines are saturated for J$\lesssim$ 6.

Separate rotation diagrams are made for each velocity component. Figure 9 shows the rotation diagrams for the broad component seen in ^{12}CO, ^{13}CO and C^{18}O plotted in the same panel. The four lines in the ^{12}CO v=0-1 rotation diagram between 1000 and 3000 K are overproduced since they are difficult to disentangle from the component at 22 kms^{-1}. For ^{12}CO v=0-1, the transitions are optically thick since the optical depth at line centre is > 1.

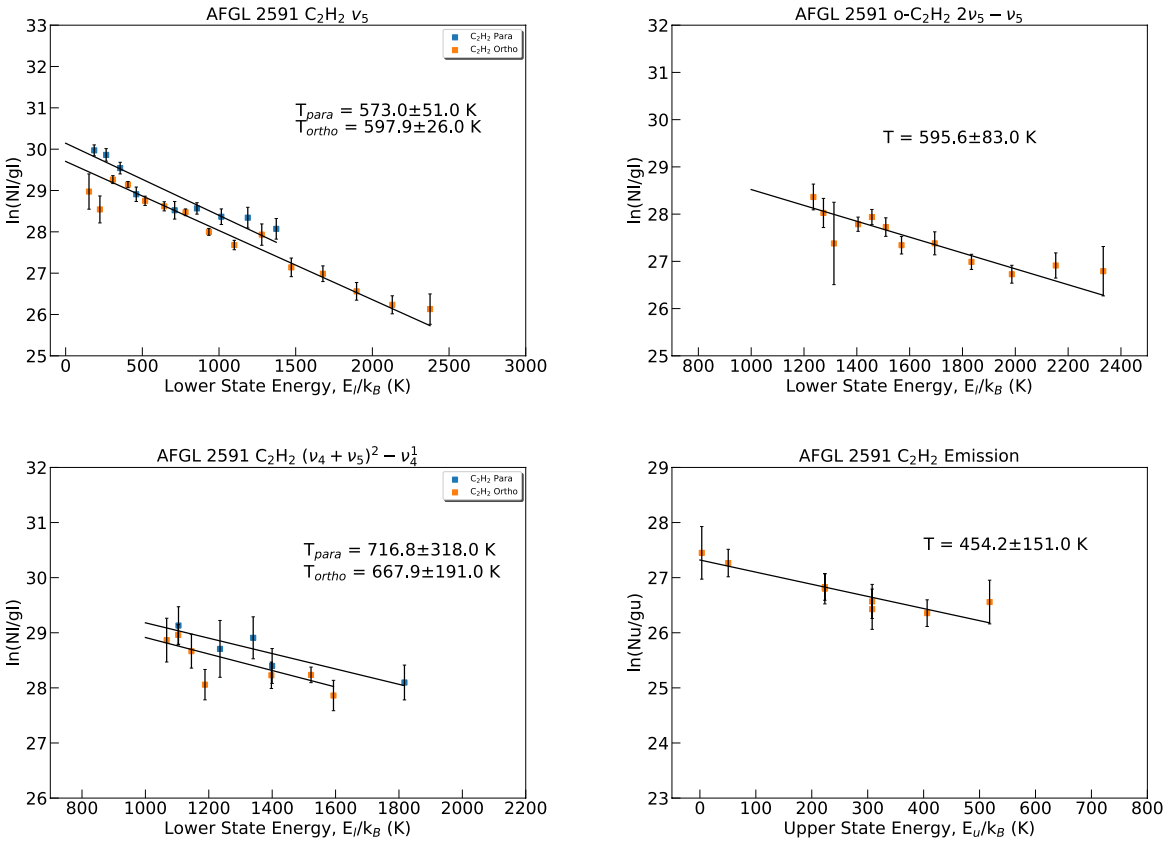

Figure 7. Acetylene rotation diagrams for the C_2H_2 bands detected in AFGL 2591 with TEXES. Ortho- and Para-C_2H_2 states are split into their corresponding ladders, and are shown as orange and blue respectively. The rotational temperatures for each are also given.

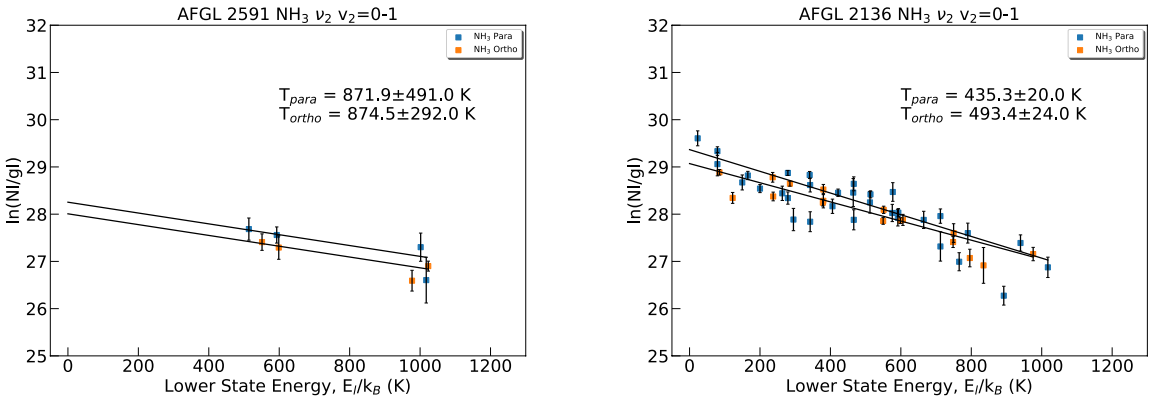

Figure 8. Rotation diagrams of the v_2=0-1 transition in the ν_2 band of NH_3 in AFGL 2591 and AFGL 2136 detected with TEXES. Both ortho- and para- states are detected and they are plotted in orange and blue respectively.

This is also the case for ^{13}CO, where low J lines of ^{13}CO and ^{12}CO overlap in the rotation diagram. For $E_l > 500$ K the ^{12}CO and ^{13}CO rotation diagrams start to separate, however the higher J lines for ^{13}CO remain to have an optical depth above 2/3.

As a result of this, we instead focus on the C^{18}O transitions which are optically thin, and the fits to the C^{18}O lines are shown in Figure 10. Comparing the line profiles between high and low J in C^{18}O (Fig 9) the broad component

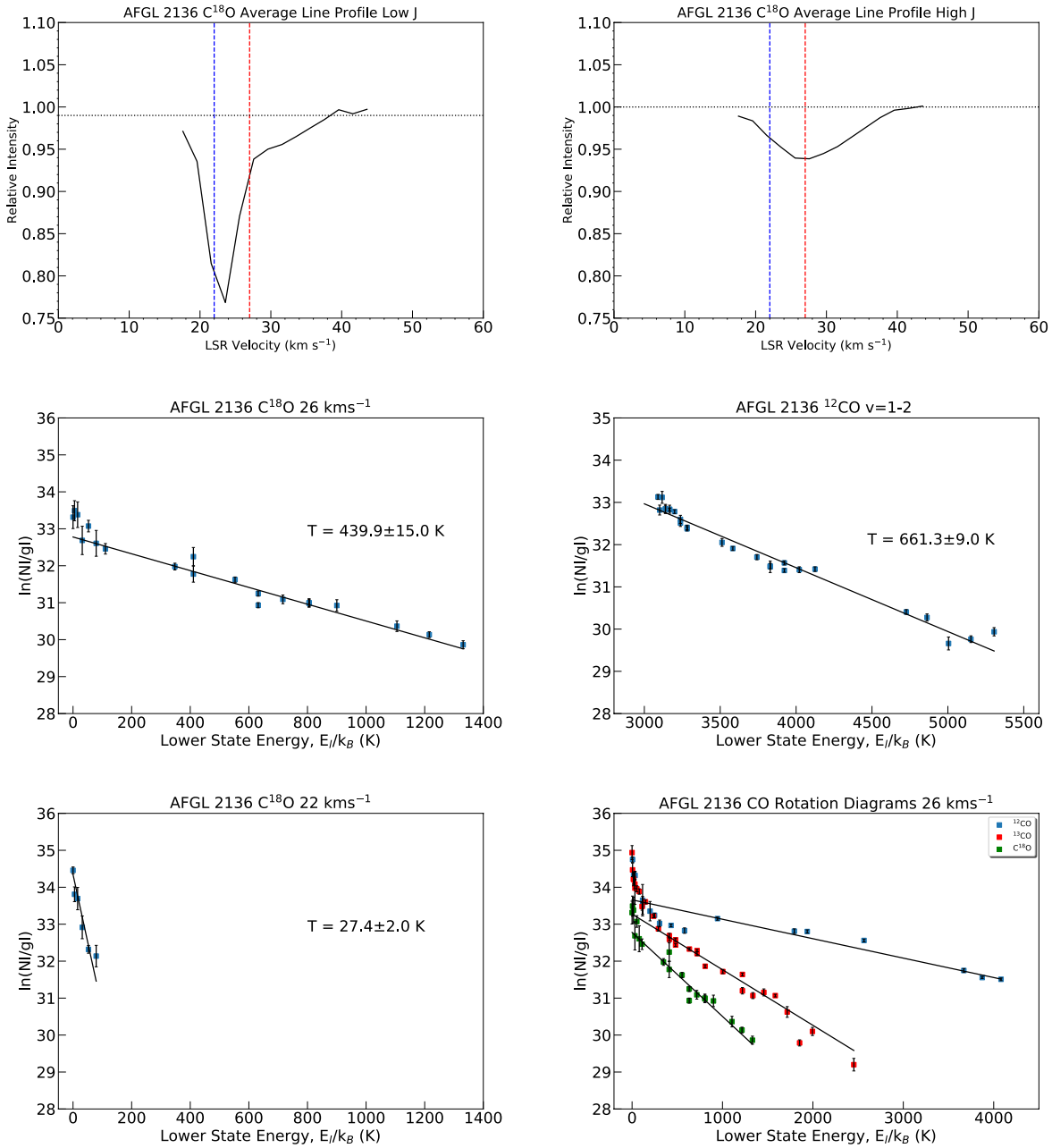

Figure 9. $C^{18}O$ v=0-1 rotation diagrams and average line profiles for high and low J, along with the rotation diagram for ^{12}CO v=1-2 in AFGL 2136. An additional plot for the hot component in AFGL 2136 is shown with ^{12}CO v=0-1, ^{13}CO v=0-1 and $C^{18}O$ v=0-1 rotation diagrams plotted on the same panel. Blue and red dashed lines correspond to the systemic velocity of the source and velocity of IR observations, respectively, which are 22 and 27 kms^{-1}, respectively. The black dotted line denotes the continuum level

centred on the red dashed line is present from low to high J, whilst the narrow component is present only at low J. This is a result of the fact that the two velocity components are also distinct in temperature, with the broad and narrow velocity components being hot and cold respectively. This distinction is seen also in ^{12}CO and ^{13}CO. Therefore the two velocity components trace different physical components. The focus of the rest of this article will be the broad component at 26 kms^{-1}, the line parameters of which are presented in Table 5.

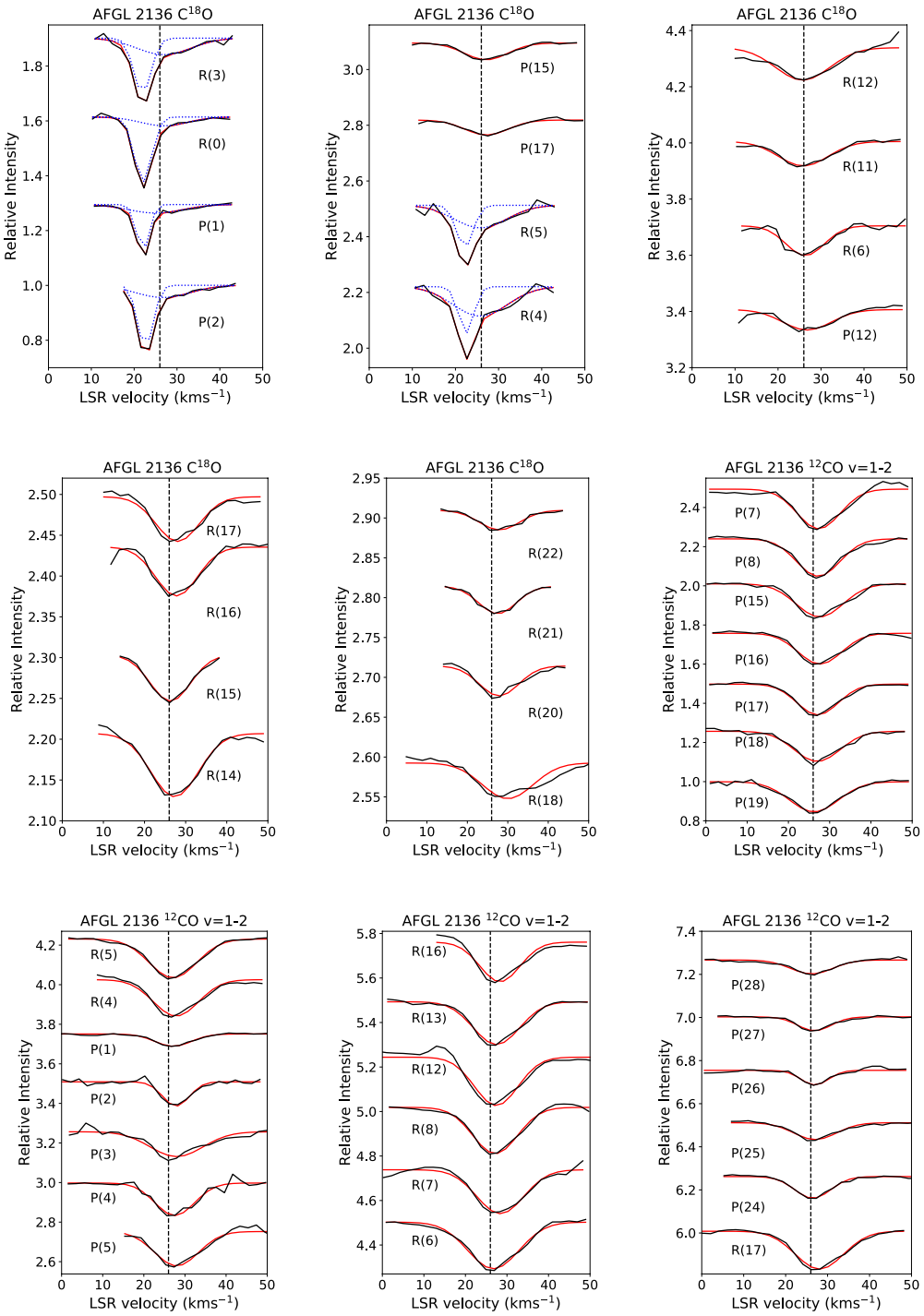

Figure 10. Multi-gaussian fitting of $C^{18}O$ v=0-1 and ^{12}CO v=1-2 line profiles in AFGL 2136 detected with iSHELL at 4.5 μm. The dashed line represents 27 kms^{-1}. The overall fit is shown in red and the individual gaussian components are in blue dotted lines.

$C^{18}O$ exhibits a straight line which suggests that the transitions are optically thin and that local thermodynamic equilibrium (LTE) is a good approximation. A temperature of 27±2 K and 440±15 K is derived for the cold and hot component, respectively. In the rotation diagram, several of the low J level lines in $C^{18}O$ appear overproduced. This is a result of blending between the 22 kms^{-1} and 26 kms^{-1} velocity components which are difficult to disentangle

since they are only separated by a small amount in velocity space, whereas for the higher energy lines, the narrow cold component at 22 kms^{-1} is not observed. Therefore these lines give a better handle on the real temperature of the gas.

26 lines of vibrationally excited ^{12}CO are also detected in AFGL 2136, and are presented in Figure 10. The transitions show a single velocity component at 27.1±0.3 kms^{-1} with a width of 12.1±0.7 kms^{-1}. This is in good agreement with hot C^{18}O. From Figure 9 we see that the rotation diagram is a straight line implying that the lines are optically thin and in LTE, with a rotational temperature of 661±9 K. We derive a vibrational temperature of 490±39 K.

The velocity derived from our observations of the hot CO component at 26 kms^{-1} is in agreement with what is found by Mitchell et al. (1990) for the v=0-1 band. They do not resolve the two velocity components in the CO line profiles. Therefore they fit two temperature components at the same velocity in the rotation diagram. The temperature of their hot component is consistent with what we find for fitting the ^{13}CO lines with E$_l$ above 100 K. The temperature that we derive for the narrow component at 22 kms^{-1} is higher than the temperature that they derive for their cold component. Mitchell et al. (1990) neglect the ^{12}CO v=0-1 transitions as they are strongly saturated and they do not discuss C^{18}O.

The two velocity components are also observed in the CO v=0-2 band at 2.3-2.4 μm(Goto et al. 2019). The temperatures for the hot component are in agreement within the errors, however for the cold component, Goto et al. (2019) measure a temperature of 16.3±2.4 K while we derive a temperature of 27±2 K for the v=0-1 band. This may be a result of uncertainty in disentangling the two velocity components since they are heavily blended. It is difficult to gauge whether or not the single gaussian fit to the 26 kms^{-1} component that we use is adequate for deriving state-specific column densities (Figs 9 & 10). This can be further seen from the line profiles of the CO v=0-2 band, where Goto et al. (2019) fit two velocity components to the hot CO component. In this case the high J CO lines may be doubly peaked as well, which is also true for the H$_2$O lines at 2.5 μm in this source (Indriolo et al. 2020).

4.2.2. *CS*

13 lines of CS are detected towards AFGL 2136 spanning an energy range of 7 to 1165 K. It is one of the species most readily detected in our spectra. One velocity component is detected at 26.1±0.4 kms^{-1} with a line width of 8.0±1.1 kms^{-1}. All lines are accounted for from J=2 to J=31 with non-detected lines being lost in strong telluric absorption or blending with other hot core lines. The CS velocity is consistent with that derived in CO, however the line width is narrower for equivalent energy levels.

Temperatures and column densities for CS are derived from the rotation diagram shown in Figure 5. A temperature of 418±23 K is measured, in good agreement with the temperature found for C^{18}O.

4.2.3. *HCN*

For AFGL 2136, 15 lines of the ν_2 band in the v$_2$=0-1 transition are detected spanning an energy range of only 1500 K. The rotation diagram gives a temperature of 625±19 K. 26 lines of HCN of the ν_2 band in the v$_2$=0-2 transition are detected in AFGL 2136. The linear part of the rotation diagram gives a temperature of 605±96 K. This is in good agreement with the temperature of the v$_2$=0-1 transition of HCN. The column density derived for the v$_2$=0-2 transition is a factor of 4 larger than the v$_2$=0-1 transition. The line profiles for the v$_2$=0-1 and v$_2$=0-2 transition are similar in AFGL 2136.

As for AFGL 2591, evidence for a temperature gradient is observed in the v$_2$=0-2 transition of HCN while it is not seen in the v$_2$=0-1 transition. The line profiles in the v$_2$=0-2 transition are consistent from low to high J (Fig 2). As in AFGL 2591, the R(0) line of the HCN v$_2$=0-2 band is offset in velocity from the other HCN lines and appears to be tracing cold foreground absorption. (Lahuis & van Dishoeck 2000) detected HCN with ISO towards AFGL 2136 and the derived temperature of 650^{+75}_{-50} K agrees between low and high spectral resolution.

4.2.4. *C_2H_2*

For the ν_5 fundamental band of C$_2$H$_2$ in AFGL 2136, 16 lines are detected. The temperature and line profiles are consistent with the other species in this source suggesting that they are co-spatial in this hot core. We derive an apparent OPR of 1.8±0.2.

We also detect vibrationally excited C$_2$H$_2$ in AFGL 2136 and rotation diagrams are shown in Figure 11. Similar to AFGL 2591, we only observe o-C$_2$H$_2$ in the $2\nu_5^2 - \nu_5^1$ band. A temperature of 480±41 K is derived, slightly lower than the ν_5 band but within the errors.

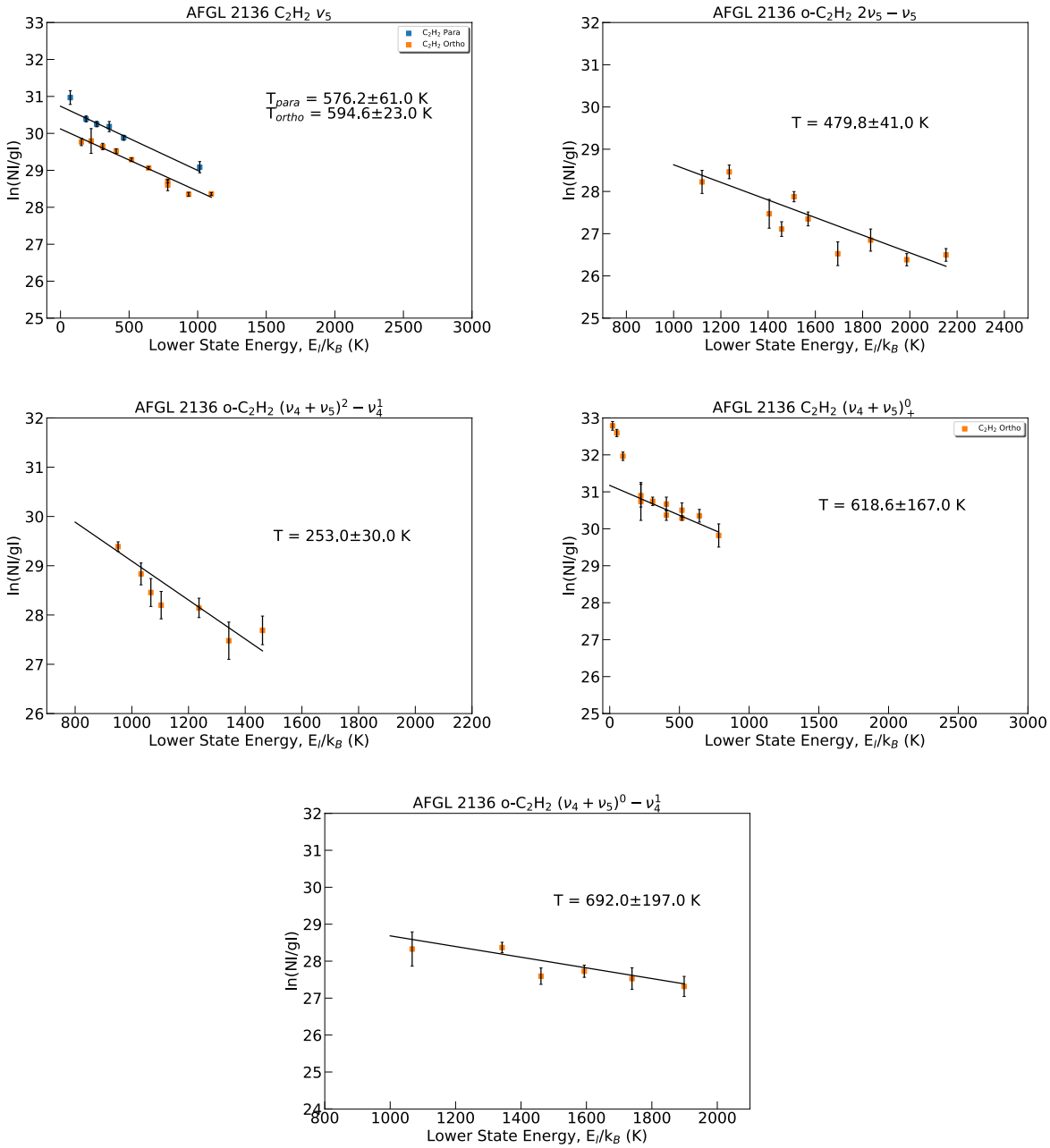

Figure 11. Acetylene rotation diagrams for the C_2H_2 bands detected in AFGL 2136 with TEXES. Ortho- and Para-C_2H_2 states are split into their corresponding ladders, and are shown as orange and blue respectively. The rotational temperatures for each are also given.

In AFGL 2136 we see an additional band, the $(\nu_4+\nu_5)^0 - \nu_4^1$ band. The line parameters are consistent with the $(\nu_4+\nu_5)^2 - \nu_4^1$ band of C_2H_2. The temperature of this band is comparable to the ν_5 band, with 692±197 K derived from the rotation diagram. The physical conditions derived from this band however are very uncertain.

In AFGL 2136, the $(\nu_4+\nu_5)$ band of o-C_2H_2 is detected in the EXES data around 7 μm. A column density of $5.0\pm0.1\times10^{16}$ cm^{-2} is derived. This is a factor of 4 higher than expected based on the column density of the ν_5 band, despite the fact that these bands trace the same lower vibrational energy level. The temperature derived for the $(\nu_4+\nu_5)$ band is measured only from the higher energy lines, since there is non-linearlity for the low energy lines, analogous to HCN at 7 μm. The derived temperature is equivalent to that found for the ν_5 band. Similar behaviour is

observed in HCN and the difference of the column density between the 7 and 13 μm C_2H_2 is of the same order as that found for HCN in AFGL 2136 (a factor of 4). We expect that non-linearity is also present in the ν_5 band, however we do not observe to long enough wavelengths to observe this trend. However it does appear that the R(6e) line is slightly overproduced in the ν_5 band. The $(\nu_4 + \nu_5)$ band of C_2H_2 is observed in AFGL 2136, but not in AFGL 2591.

C_2H_2 has been detected in AFGL 2136 with ISO-SWS with a temperature of 800 K (Lahuis & van Dishoeck 2000), higher than what we observe with EXES/TEXES. This may be a reflection of the much lower spectral resolution of ISO-SWS and the fringing inherent to this instrument.

4.2.5. *NH_3*

Figure 8 shows the rotation diagram for the v_2=0-1 transition in the ν_2 band of NH_3 in AFGL 2136. Approximately 50 lines are detected including both ortho and para states and the transitions cover an energy level range of over 1000 K. p-NH_3 and o-NH_3 have peak velocities and line widths that are in agreement, however the temperature derived from the rotation diagrams are slightly different with the o-NH_3 being higher. An OPR of 1±0.5 is derived, consistent with the high rotational temperature. NH_3 in AFGL 2136 is a very good example of the power of this method to detect many lines by only observing a handful of spectral settings. Another band of NH_3, the ν_4 band at 6 μm is included in our spectral range, but no transitions were apparent, consistent with Indriolo et al. (2020).

Table 2. Summary of Species in AFGL 2591

Species	Band	λ_0 (μm)	Number of Lines	Temperature (K)	N (cm^{-2})	Abundance (w.r.t H)	v_{lsr} (kms^{-1})	ΔV (kms^{-1})
^{13}CO	v=0-1	–	8	49 ±3	$3.8\pm0.2 \times 10^{16}$	$2.4\pm0.2 \times 10^{-6}$	-9.2±0.3	1.5
	v=0-1	–	8	671 ±124	$3.4\pm0.2 \times 10^{16}$	$2.8\pm1.0 \times 10^{-6}$	-12.0±0.6	10.5
^{12}CO	v=1-2	4.7	8	664 ±43	$1.5\pm0.6 \times 10^{16}$	$1.2\pm0.4 \times 10^{-6}$	-8.4±0.5	16.4±1.6
H_2O	ν_2 v_2=0-1	6.0	8	[a] 640 ± 80	[a] $3.7\pm0.8 \times 10^{18}$	–	-11.0	12.4
HCN	ν_2 v_2=0-2	7.0	16	671 ± 118	$2.4\pm0.2 \times 10^{17}$	$2.0\pm1.0 \times 10^{-5}$	-11.7±0.5	10.8±1.3
	ν_2 v_2=0-1	14.0	20	675 ±32	$2.7\pm0.2 \times 10^{16}$	$3.4\pm0.6 \times 10^{-6}$	-8.9±0.5	8.2±1.3
	ν_1 v=1-0	3.0	21	240±13	$7.9\pm0.5 \times 10^{15}$	–	-9.6±0.5	6.3±1.0
CS	v=0-1	7.8	18	713 ± 59	$1.6\pm0.1 \times 10^{16}$	$1.5\pm0.3 \times 10^{-6}$	-10.4±0.5	8.4±1.7
p-C_2H_2	ν_5	13.7	9	573±51	$4.8\pm0.5 \times 10^{15}$	$5.8\pm2.3 \times 10^{-7}$	-8.8±0.4	7.7±1.1
	$(\nu_4 + \nu_5)^2 - \nu_4^1$	13.7	5	717±318	$4.2\pm3.8 \times 10^{15}$	$4.9\pm4.4 \times 10^{-7}$	-9.6±0.9	8.8±2.5
o-C_2H_2	ν_5	13.7	15	598±26	$1.0\pm0.1 \times 10^{16}$	$1.2\pm2.3 \times 10^{-6}$	-9.0±0.4	8.7±1.1
	$2\nu_5^2$ - ν_5^1	13.7	12	596±83	$2.7\pm0.4 \times 10^{15}$	$3.5\pm1.5 \times 10^{-7}$	-8.7±0.6	8.3±1.8
	$(\nu_4 + \nu_5)^2 - \nu_4^1$	13.7	7	668±191	$7.7\pm6.9 \times 10^{15}$	$1.0\pm0.9\times10^{-6}$	-7.7±0.5	7.4±1.4
	$\nu_2 + (\nu_4 + \nu_5)$	3.0	8	454±151	$6.0\pm0.9 \times 10^{15}$	–	-7.4±0.5	3.7±1.2
p-NH_3	ν_2 v_2=0-1	9.5	4	872±491	$1.3\pm0.7 \times 10^{16}$	$1.6\pm0.9 \times 10^{-6}$	-6.9±0.6	6.2±1.5
o-NH_3	ν_2 v_2=0-1	9.5	4	875±292	$1.0\pm0.4 \times 10^{16}$	$1.4\pm0.5 \times 10^{-6}$	-7.3±0.4	7.8±1.1

Note: no abundances relative to H are given for H_2O because stellar atmosphere theory is not used in the analysis of Indriolo et al. (2015).

Note: no abundances for the HCN ν_1 and C_2H_2 $\nu_2 + (\nu_4 + \nu_5)$ emission bands are given since we measure column densities for these bands which are given in section 5.3.

[a] Indriolo et al. (2015)

Table 3. Summary of Species in AFGL 2136

Species	Band	λ_0 (μm)	Number of Lines	Temperature (K)	N (cm^{-2})	Abundance (w.r.t H)	v_{lsr} (kms^{-1})	ΔV (kms^{-1})
$C^{18}O$	v=0-1	–	6	27± 2	$8.7\pm0.7 \times 10^{15}$	$2.8\pm0.1 \times 10^{-6}$	22.2±0.3	2±0.8
	v=0-1	–	20	440± 15	$2.9\pm0.2 \times 10^{16}$	$1.9\pm0.1 \times 10^{-6}$	27.1±0.6	12.3±1.5
^{12}CO	v=1-2	4.7	26	661±9	$2.7\pm0.2 \times 10^{16}$	$1.7\pm0.4 \times 10^{-6}$	27.1±0.3	12.1±0.7
H_2O	ν_1 / ν_3	2.5	34	[a]502 ± 12	[a]$8.25\pm0.95\times10^{18}$	–	24.6±1.1	13.2±2.5
HCN	ν_2 v_2=0-2	7.0	18	592 ± 21	$1.8\pm0.2 \times 10^{17}$	$1.6\pm0.8 \times 10^{-5}$	26.2±0.5	8.5±1.6
	ν_2 v_2=0-1	14.0	15	625±19	$4.6\pm0.2 \times 10^{16}$	$5.3\pm0.4 \times 10^{-6}$	26.1±0.5	11.0±1.5
CS	v=0-1	7.8	13	418 ± 23	$1.6\pm0.1 \times 10^{16}$	$1.2\pm0.1 \times 10^{-6}$	26.1±0.4	8.0±1.1
p-C_2H_2	ν_5	13.7	6	576±61	$8.8\pm0.7 \times 10^{15}$	$1.0\pm0.4 \times 10^{-6}$	27.0±0.3	10.9±1.1
o-C_2H_2	ν_5	13.7	10	595±23	$1.6\pm0.1 \times 10^{16}$	$1.7\pm0.1 \times 10^{-6}$	27.2±0.3	11.3±0.9
	$2\nu_5^2$ - ν_5^1	13.7	10	480±41	$1.6\pm1.0 \times 10^{15}$	$2.3\pm0.1 \times 10^{-7}$	26.6±0.4	7.1±1.2
	$(\nu_4+\nu_5)^2-\nu_4^1$	13.7	7	253±30	$1.7\pm1.5 \times 10^{15}$	$1.3\pm1.3 \times 10^{-7}$	26.9±0.6	8.1±1.8
	$(\nu_4+\nu_5)^0-\nu_4^1$	13.7	6	692±197	$2.1\pm0.2 \times 10^{15}$	$2.3\pm2.0 \times 10^{-7}$	26.8±0.6	8.5±1.9
	$(\nu_4+\nu_5)$	7.5	12	618±176	$5.0\pm0.1 \times 10^{16}$	$7.0\pm0.8 \times 10^{-6}$	26.0±0.5	8.0±1.5
p-NH_3	ν_2 v_2=0-1	9.5	32	435±20	$1.0\pm0.5 \times 10^{16}$	$1.0\pm0.1 \times 10^{-6}$	28.1±0.4	6.7±1.0
o-NH_3	ν_2 v_2=0-1	9.5	17	493±24	$0.9\pm0.4 \times 10^{15}$	$9.7\pm0.5 \times 10^{-7}$	27.7±0.3	7.7±0.9

Note: no abundances relative to H are given for H_2O because stellar atmosphere theory is not used in the analysis of Indriolo et al. (2020).

[a] Indriolo et al. (2020)

4.3. *Comparison to Sub-millimetre Observations*

Absorption lines at IR wavelengths probe the hot core on very small spatial scales, comparable to the smallest achievable by sub-mm emission line studies (0.02″). On scales as large as 10″, differences in line widths, peak velocities, temperatures and column densities are observed between sub-mm emission and IR absorption studies. This is summarised in Figure 12, where we compare the results from our MIR line survey of AFGL 2591 with a line survey by Kaźmierczak-Barthel et al. (2014) from 480-1900 GHz (with respective beam sizes 10-40 ″), with *Herschel*/HIFI.

Temperatures compare on average with 700 K for IR absorption to 50 K in sub-mm emission. The temperature derived from the emission lines corresponds well with the temperature of the cold ^{13}CO absorption component (Table 2). For AFGL 2591 the velocity of the sub-mm emission lines agrees with the systemic velocity and is on average -5.5 kms^{-1}, consistent with other studies of this source in the sub-mm (Wang et al. 2012; Gieser et al. 2019; van der Tak et al. 2003). However from the IR absorption lines the velocity observed is -10 kms^{-1}. Furthermore the line widths of the absorption lines are around a factor of 2 higher than those measured in the sub-mm.

Towards AFGL 2591, 6 lines of HCN were detected in emission and a population diagram results in an estimate of the temperature of 35 K (Kaźmierczak-Barthel et al. 2014). In total, we detect 42 lines of HCN from 2 different transitions in the IR spanning an energy range of 0 to 2500 K in AFGL 2591. The large number of lines combined with the large span in energy range gives a good handle on the physical conditions and a temperature of 670 K is derived.

Although not many species have been detected towards AFGL 2136 at sub-mm wavelengths, CS has been detected by van der Tak et al. (2003). A velocity of 22.8 kms^{-1} and a line width of 3.1 kms^{-1} are derived for sub-mm emission lines. This contrasts with the IR absorption where we derive a v_{lsr} of 26.1 kms^{-1} and a width of 8 kms^{-1}. This is consistent with the two velocity components we see in CO presented in section 4.2.1. From a rotation diagram analysis we see that the narrow 22 kms^{-1} component is cold while the broad 26 kms^{-1} component is hot.

As mentioned in section 4.2.1, IR CO line profiles of AFGL 2136 reveal two velocity components in the same line of sight (Figure 9); a cold component with narrow lines centred at 22 kms^{-1} and a hot component with broad lines centred at 26 kms^{-1}. Maud et al. (2018) observed this source with the Atacam Large Millimetre Array (ALMA) and detected an unresolved disk-like structure in SiO and dust continuum, at 22 kms^{-1}. SiO emission is observed to be spatially extended at 22 kms^{-1}, which is the systemic velocity of the cloud as derived from previous sub-mm observations (van der Tak et al. 2003), suggesting that the velocity component we detect in the IR at 26 kms^{-1} is not spatially resolved by Maud et al. (2018).

However, recent very high angular resolution (20×15 mas) observations with ALMA by Maud et al. (2019) reveal that sub-mm observations can resolve this velocity component if the spatial resolution is high enough. Velocity maps of the H_2O $5_{5,0} - 6_{4,3}$ $\nu_2 = 1$ line show that a Keplerian disk is resolved which is centred at a velocity of 26 kms^{-1}.

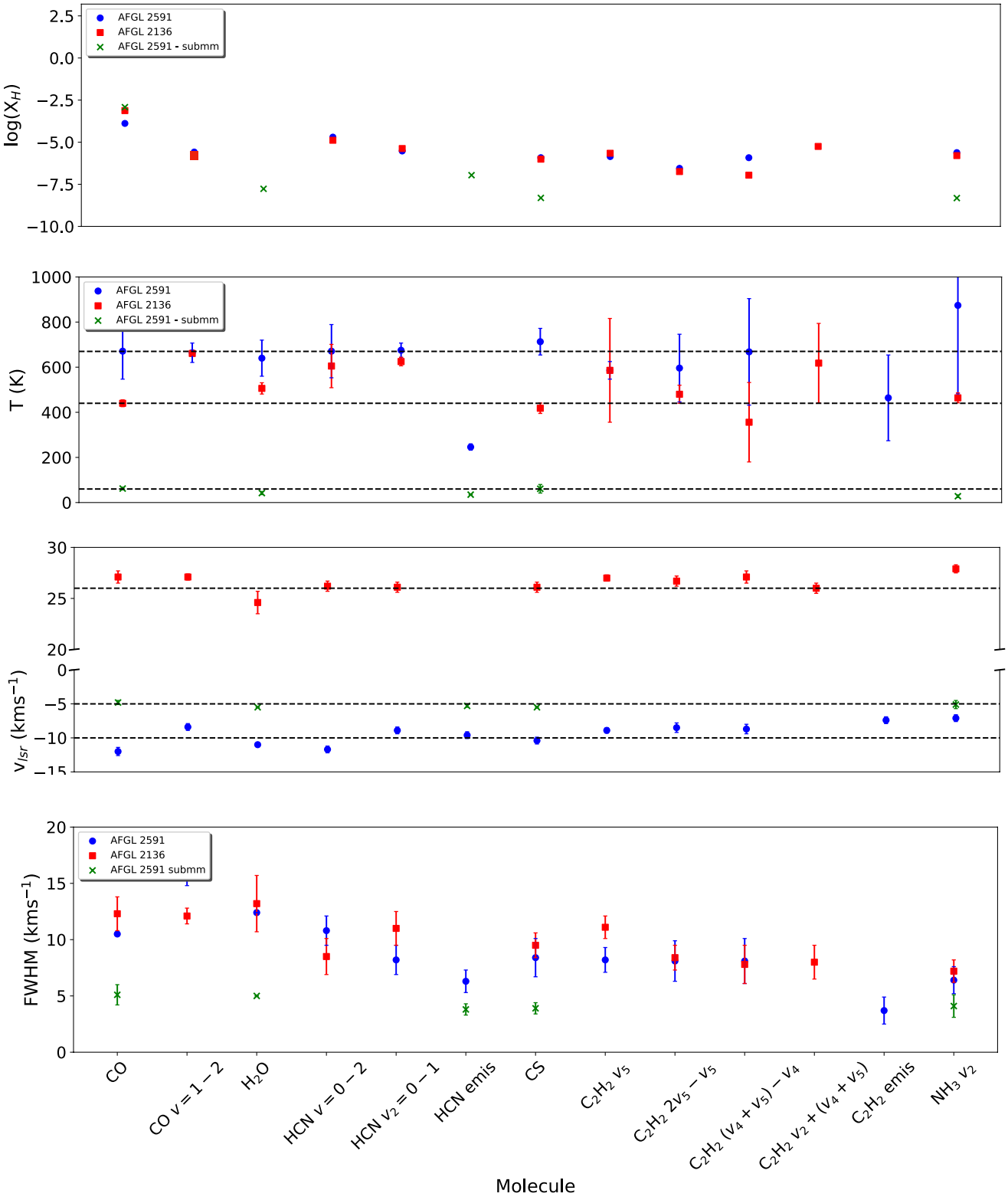

Figure 12. Scatter plots comparing the temperature, abundance w.r.t H, velocity and line width of selected molecules observed towards AFGL 2591 (blue circles) and AFGL 2136 (red squares), and also the literature values for AFGL 2591 (green crosses) observed in the sub-mm (Kaźmierczak-Barthel et al. 2014). For the sub-mm abundances, a H column of $\sim 1 \times 10^{22}$ cm^{-2} was assumed following Kaźmierczak-Barthel et al. (2014).

Furthermore, since this line lies 3461 K above ground, this gas must be hotter than the temperature estimates given by previous sub-mm studies, which is more consistent with the IR absorption lines.

A recent study of AFGL 2591, (Gieser et al. 2019) analyses chemical complexity in this hot core. The pure rotational CO J=2-1 line profile that is presented in their Figure 7 shows a complex velocity structure, analogous to that which we see in IR absorption. There is a broad, blue-shifted part of the line profile that appears to consist of several velocity components, one of which is centred around -10 kms^{-1}. There is also tentative evidence for this same velocity component being present in the emission line profile of SiO, however the other more blue-shifted velocity components are missing. This further indicates that it is possible to resolve in emission this inner part of the hot core that is so evident in IR absorption.

Overall, IR observations trace hot, dense gas at the centre of the hot core. Sub-mm observations, unless at very high angular resolution (0.02″), probe the surrounding envelope and cloud where temperatures are lower.

5. DISCUSSION

Summarising the observations presented in Section 4, MIR spectra of AFGL 2136 and 2591 show absorption bands of a number of molecular species, which can be analysed in terms of the velocity and temperature of the absorbing gases. There are a number of differences between IR and sub-mm wavelengths that provide further insight into the structure of these sources. The IR lines are typically seen in absorption and the sub-mm lines in emission, there is a peak velocity offset (Fig 12), and the line width is typically much larger (Fig 12) in the IR than in the sub-mm (van der Tak et al. 2003; Kaźmierczak-Barthel et al. 2014; Gieser et al. 2019). In addition, the IR lines originate from gas that is typically much warmer (400-600 K) than the sub-mm lines (20-200 K).

5.1. *General Structure of the Sources*

Very high angular resolution observations of AFGL 2136 in the N band with the mid-infrared interferometer (MIDI) instrument on the Very Large Telescope Interferometer (VLTI), H and K band polarisation studies with the Subaru telescope, sparse aperture Keck interferometry and sub-mm dust emission with ALMA reveal the presence of a geometrically thin circumstellar dust disk with an inner and outer radius of 30 and 120 AU respectively (Murakawa et al. 2008; Monnier et al. 2009; de Wit et al. 2011; Boley et al. 2013; Maud et al. 2019). The whole system is embedded in a dusty envelope. The circumstellar disk is optically thick in the MIR continuum and the N-band emission originates from a radius of ∼100 AU. Inside the dust sublimation radius (≤30 AU), the disk is thought to be gaseous. Recent ALMA observations at high spatial resolution in a highly excited H_2O line (E_u=3461.9 K) reveal the presence of a disk in Keplerian rotation around the central ∼45 $M_\odot$ protostar (Maud et al. 2019). The total disk mass, estimated from the sub-mm continuum, is somewhat sensitive to the adopted temperature but is of the order of 1 $M_\odot$ (Maud et al. 2019).

Both AFGL 2136 and AFGL 2591 have been imaged at 10.7 μm with the Keck telescope (Monnier et al. 2009). The physical structure of both of these sources is very similar at this wavelength. The MIR continuum is asymmetrically extended to the West around the disk, out to around 250 mas. However, the extended emission is an order of magnitude lower in intensity than the continuum emission from the compact disk. For AFGL 2136, the FWHM size of the MIR continuum is 125±5×115±3 mas for the major and minor axes, respectively. This is reasonably consistent with the size of the disk in the ALMA 1.3mm continuum image, 93×71 mas for the major and minor axes, respectively. This 25 % difference in size, and the somewhat flatter disk seen in the ALMA image, could be due to the fact that at 10 μm the observer looks less deep into the disk than at sub-mm wavelengths, making it appear more spherical and extended at 10 μm. The size of the MIR continuum in AFGL 2591 is 123±3×111±3 mas for the major and minor axes, respectively. Since the MIR continuum is dominated by the disk, we neglect envelope emission contributing to the continuum of our absorption lines.

At MIR wavelengths, both sources are characterised by extended emission incommensurate with the central protostar. The ALMA observations of AFGL 2136 reveal that the MIR emission coincides with a circumstellar disk in Keplerian rotation. In the following, we presume that this is also the case for AFGL 2591 and will discuss this more in section 5.6.2. As the MIR continuum emission is dominated by the disk, the absorption lines have to originate in the photosphere of this disk.

For AFGL 2136, the observed peak velocity of the IR absorption lines is in good agreement with that of the H_2O sub-mm emission line which clearly associates the absorbing gas within the disk (rather than the surrounding envelope or molecular cloud in which the source is embedded). The observed high temperatures also argue for a location in the

inner warm regions. The line width of the CO, HCN, C_2H_2 and NH_3 IR absorption lines are narrower than that of the H_2O sub mm emission line. This is also the case for H_2O absorption (Indriolo et al. 2020). Absorption may still be associated with the Keplerian disk if the absorption does not trace the full extent of the disk. This will be discussed in more detail in section 5.6.1.

The fact that the lines are in absorption implies that the disk surface behaves like a photosphere with a temperature which decreases outwards. Hence, rather than heating of the disk surface from the outside by impinging stellar (UV/visible) radiation, the disk is heated from the inside, and radiative diffusion sets up a temperature gradient decreasing outwards in the radial and vertical directions. We attribute the heating to rapid accretion in the mid-plane, which viscously heats the gas to high temperatures.

At the high densities of the disk, the dust and gas temperature will be closely coupled in this situation. Models for viscous disks imply a radial temperature gradient with an exponent in the range of -0.4 to -0.7 (Dullemond et al. 2007). Following the N-band continuum studies, we set the temperature of the dust disk photosphere to the sublimation temperature (1200 K) at 30 AU, which implies a dust temperature at 120 AU of 450 K. Hence, the disk would indeed be bright in mid-IR continuum and, given the much larger surface area, would outshine the dust photosphere of the protostellar cocoon.

As sketched in Figure 13, the observed spectrum will originate from "characteristic" regions in the disk, with shorter wavelengths coming from the inner regions and longer wavelengths predominantly from further out. For any region in the disk, at any wavelength, the observed flux will originate from a total optical depth $(\tau_L + \tau_c) = 2/3$, where τ_L and τ_c are the line and continuum optical depth respectively. The decreasing temperature towards the surface will then lead to an absorption line.

5.2. *Abundance Analysis*

Since we are dealing with an internally heated disk, and therefore an outwardly decreasing temperature gradient in the vertical direction, some further insight into the characteristics of these disks can be obtained by standard stellar atmosphere analysis of absorption lines. We will base this analysis on the radiative transfer equation in the grey approximation, $\kappa(\nu) =$ constant. It is likely that the dust has coagulated either during the preceding molecular cloud phase or in the disk and will have a grey-like opacity (Ormel et al. 2011). Using the Milne-Eddington solution to the equation of radiative transfer in a grey atmosphere applied to line formation (Mihalas 1978), the observed flux at any wavelength will originate from a total optical depth $(\tau_L + \tau_c) = 2/3$. This assumes an average over viewing angles through the atmosphere. The outward-decreasing temperature gradient will then give rise to an absorption line and, comparing absorption by different species, lines tend to be stronger when the line opacity is larger. The full details of the derivation of the Milne-Eddington solution, along with further information, can be found in the Appendix section A.

We conclude that for a weak line (relative to the continuum), the central depth (or equivalent width) is a measure of the relative column density in the lower level of the molecule. One important conclusion is then that the measured central depths can still be used in a Boltzmann diagram analysis, and the excitation temperatures used from the initial rotation diagram analysis still applies. The column density is relative to the continuum opacity, which itself is a measure of the hydrogen column density (and the dust absorption properties). In this way the line strength is a measure of the abundance with respect to H of the molecular levels, which can be used in a rotation diagram to derive the total abundance of the species. This conversion also involves the temperature gradient in the atmosphere through the coefficients a and b in the source function (see Appendix section A). Since the line opacity is much less than the continuum opacity, the molecules absorb continuum photons therefore coupling the gas and dust.

In the weak line approximation, we can use the curve of growth approach and for the linear portion we arrive at (Mihalas 1978 section 10.3):

$$\frac{W}{2Y\Delta\nu} = \eta_0 \frac{\sqrt{\pi}}{2} \tag{4}$$

with W the equivalent width in frequency space, $\Delta\nu$ is the line width in frequency space and Y a parameter which takes care of the gradient in the source function and is defined in the Appendix section A. Here the peak line-to-continuum ratio at line centre, η_0, is given by

$$\eta_0 = \frac{\kappa_L(\nu = \nu_0)}{\kappa_c} = \frac{A_{ul}\lambda^3}{8\pi\sqrt{2\pi}\sigma_v} \frac{g_u}{g_l} \frac{N_l}{\sigma_c N_H} \left(1 - \frac{g_l N_u}{g_u N_l}\right) \tag{5}$$

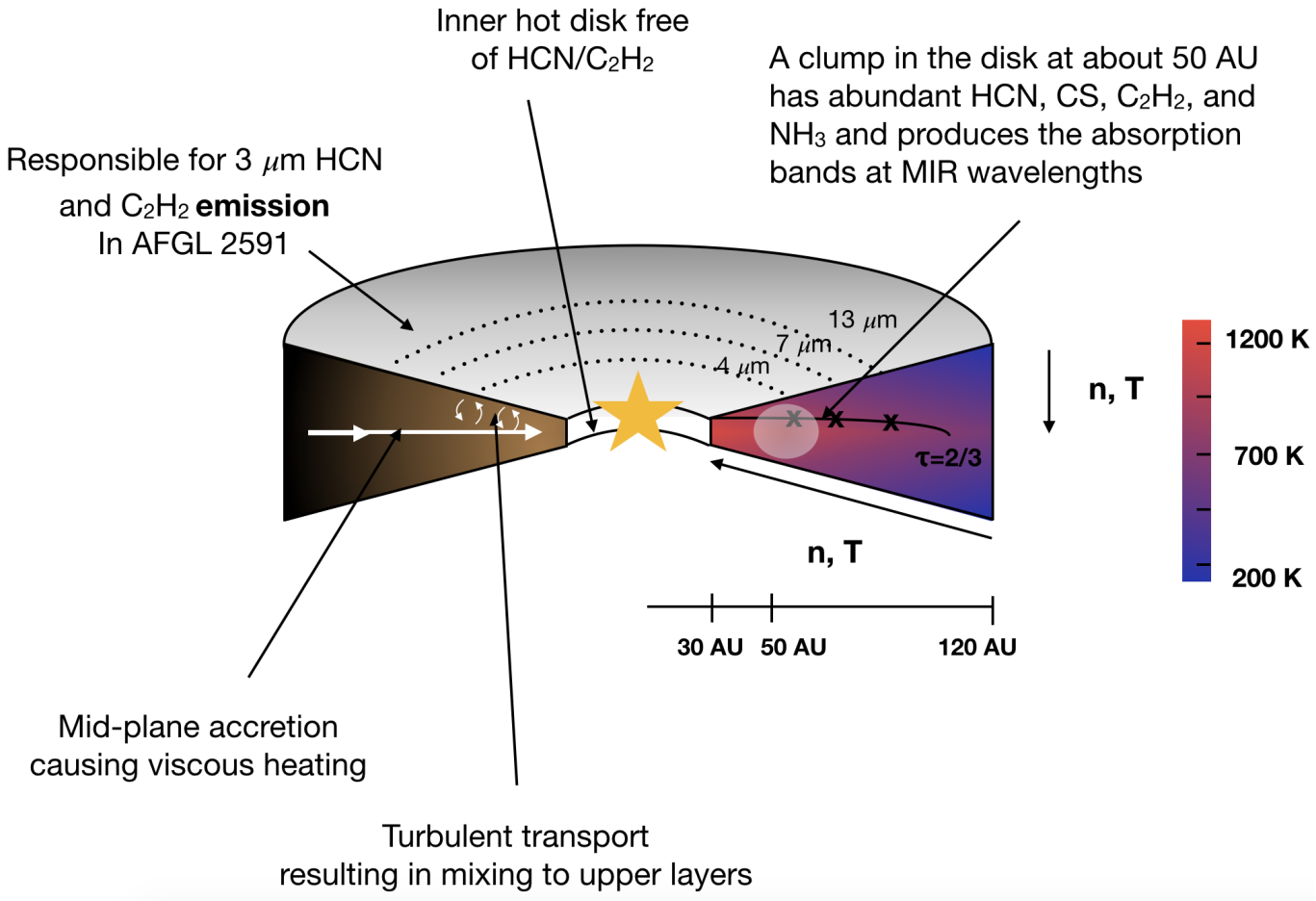

Figure 13. Slice of the disk showing the structure of the disk and the physical processes taking place. Dotted lines represent the extent of the disk at the $\tau = 2/3$ dust photospheres at 4, 7 and 13 μm. The black solid line indicates the $\tau = 2/3$ optical depth profile through the disk with wavelength, where crosses indicate the wavelength corresponding to the dotted lines. The blue/red colour scheme shows the temperature of the disk and is represented by the colourbar on the right. A physical scale is given indicating at what radii the given positions are. Temperature and density increase towards the mid-plane, and also towards the star in the centre. The transparent circle represents the dust clump at 50 AU from the protostar, that produces the absorption lines. The innermost region of the disk is free of HCN and C_2H_2 gas and dust. Turbulent mixing results in HCN and C_2H_2 gas being carried up to the cooler, upper layers of the disk where resonant scattering of the disk continuum causes emission lines.

where A_{ul} is the coefficient for spontaneous emission, g_u and g_l are the statistical weights for the upper and lower levels respectively, ν_0 is the line frequency and κ_L and κ_c are the line and continuum opacities respectively and N_l is the column density in the lower level of the line. σ_v is the dispersion in velocity space and σ_c the dust opacity per H-nucleus. For the latter we will adopt the value 7×10^{-23} cm^2/H-nucleus appropriate for coagulated interstellar dust (Ormel et al. 2011). This value is not very sensitive to the degree of coagulation. Here the expression for stimulated emission (the term in brackets) has been neglected since it is very close to unity.

The optical depth of the absorption lines is thus set against the continuum and therefore the level-specific column densities are calculated relative to the hydrogen column density. We measure the equivalent width of the absorption lines and thus calculate level specific abundances which, using equation 3, results in a total abundance for a given species (Tables 2 & 3).

We note the dependence on the adopted dust characteristics and hence the quoted absolute abundances carry that uncertainty. For lines that originate from the same spatial zone, derived abundances can still be directly compared. As the disk will show a strong radial temperature gradient in addition to the vertical temperature gradient, we recognise

that derived abundances for lines that originate from a wide zone in the disk are ill defined without a detailed model for the disk. Dilution by continuum from regions with low molecular abundances will also result in ill-defined averages of the abundance over the emitting disk surface. Thus, abundance comparisons have to be taken with caution. However, as we will argue below, the observations indicate that much of these molecular absorption lines originate from the same region of the disk.

In both hot cores, the measured OPRs for C_2H_2 are less than the statistical equilibrium value of 3 for high temperatures. An ortho to para ratio of 3 is expected for this molecule as the observed (excitation) temperature (600K) is well above the energy difference between these states and, as we will argue in section 5.7, the high observed abundance requires formation of this molecule in hot gas. However we measure 2.1±0.3 and 1.8±0.2 for AFGL 2591 and AFGL 2136 respectively. We attribute this slightly lower value for the C_2H_2 OPR to the finite optical depth of these transitions. The observed strength of a line is only a direct measure of the column density in the weak opacity limit. When the opacity increases, the temperature gradient comes into play. Ortho lines will have 3 times the column density of the para lines. Hence, if line optical depth becomes important relative to that of the dust, our observations of the ortho lines will trace gas slightly higher in the photosphere than the para lines, and hence derived abundances will be smaller than those of the para transitions. The fact that the OPR is not equal to 3 is evidence for temperature gradients. Detailed modelling will be necessary to fully disentangle the effects of gradients.

In the above analysis of the abundances of molecular species, several assumptions are made that are important to emphasise. We assume that the opacity is dominated by dust (weak line limit) and that albedo is small thus $\epsilon = 1$. Furthermore we assume that the dust and the gas are well coupled thermally, the level populations are in LTE and dust properties do not vary as a function of distance to the star. We also take a grey atmosphere, namely that the source function is linear, which has a number of assumptions that result in uncertainties in the abundances. These include the degree of dust-to-gas ratio (settling), the extent to which coagulation has proceeded and compaction (e.g., porosity) of the grains. This results in additional uncertainty in the absolute abundances of the molecules however it does not affect the relative abundances of the species, so the actual abundance relative to H will depend on the adopted value of dust opacity, but abundances between species are directly comparable.

Comparing the abundances to the sub-mm observations at high spatial resolution ($> 0.5''$), we see that the abundances calculated for the IR absorption lines in AFGL 2591 are higher by 2-3 orders of magnitude (Figure 12). This is also true of AFGL 2136 where van der Tak et al. (2003) detect CS from single-dish sub-mm observations and derive an abundance of 4×10^{-9} with respect to H_2. This compares to an abundance of 1.2×10^{-6} with respect to H from the IR absorption lines. For AFGL 2591, the derived abundance for ^{13}CO corresponds to a ^{12}CO abundance of $1.6\pm0.5\times10^{-4}$, assuming a $^{12}C/^{13}C$ ratio of 60. This agrees well with the typical CO abundance of 1×10^{-4}(Lacy et al. 1994). Taking a $^{16}O/^{18}O$ ratio of 500 (Asplund et al. 2009) we derive a $C^{16}O$ ratio of $9.4\pm5.0\times10^{-4}$ with respect to H for AFGL 2136. This is larger than the typical CO abundance which may reflect that the chosen dust opacity per H-atom in this source was too high. We will return to this issue in section 5.5

5.3. *Emission Lines of HCN and C_2H_2 in AFGL 2591*

While the 4 to 14 μm window exclusively shows molecular absorption lines, the 3 μm region of the spectrum of AFGL 2591 shows emission lines of HCN and C_2H_2. One major conclusion from these emission lines is that the abundance of HCN and C_2H_2 are very low in the innermost, warm region that is responsible for the 3 μm continuum. The absence of broad HCN and C_2H_2 absorption lines in the 3 μm region implies that there is an HCN/C_2H_2 free region in the innermost parts of the disk (Figure 13). This should be contrasted with CO which does show absorption lines in the (v=0-2) overtone in the K band (R. Smith 2020, private communication). Hence, the CO abundance must be high throughout the entire disk and produce absorption features, which greatly overwhelm scattered photons from the cooler portions of the disk.

The emitting gas is characterised by low temperatures (250 K) and small line width (3-6 kms^{-1}). The line profiles in Figure 14 reveal that the velocities of the emission and absorption lines of HCN are the same, firmly associating this gas with the disk. This is also true of C_2H_2, suggesting that emission of HCN and C_2H_2 in the disk originates from the same radial part as the corresponding absorption. As the 3 μm continuum emission likely arises from a region of the disk further in than the longer wavelength emission, we attribute these emission lines to resonant scattering by C_2H_2 and HCN molecules high up in the photosphere of the disk at the same radial location that is responsible for the 7 and 13 μm absorption lines. This would in a natural way explain the relatively low temperatures and the small line widths. For this to occur, at 3 μm there must be an optically thin gas layer in the upper photosphere of the

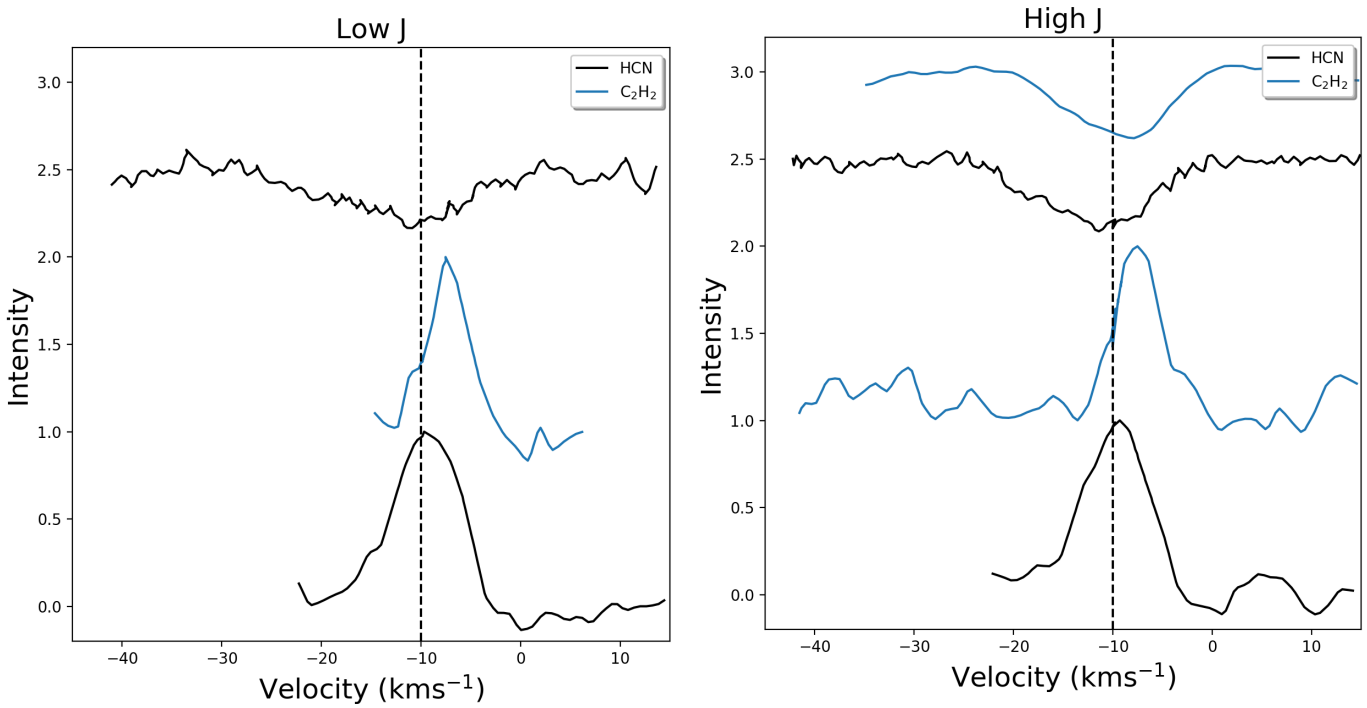

Figure 14. Average line profiles comparing HCN and C_2H_2 emission and absorption line profiles in AFGL 2591 plotted in velocity space. The HCN absorption transition is ν_2 v$_2$=0-2 and the C_2H_2 absorption band is the ν_5. Transitions are separated into high and low J levels before the average is calculated (high for E_l < 90 K). The black dashed line denotes -10 kms^{-1}.

disk, indicative of dust settling in the disk. Likely, the disk is flaring at large scale heights and the gas is turbulently brought up to high altitudes where it is exposed to near-IR pumping continuum photons from the warm inner disk.

Consider a disk with size R_{out} which emits continuum (black body) radiation at 3 μm over a small region with surface area A. The flux seen by gas, at a distance R from this continuum source to the gas is then

$$F_R = \frac{L}{2\pi R^2} = \frac{A\pi B}{2\pi R^2} = \frac{AB\,(T)}{2R^2} \quad . \tag{6}$$

where we have included an extra factor of 0.5 in the denominator since the disk sees half of the flux. The flux scattered into our direction by gas in an annulus, dR, is then,

$$dF_s = 2\pi R F_R N_s \frac{d\sigma}{d\Omega} dR \quad , \tag{7}$$

where N_s is the column density of scattering molecules along the line of sight from the continuum source to the emitting gas, and $d\sigma/d\Omega$ is the differential scattering cross section, approximated by $\sigma/4\pi$. We find then for the line to continuum ratio that the observer sees,

$$\frac{F_s - F_c}{F_c} = \frac{F_L}{F_c} = \frac{\tau_s}{4\pi} \ln\left[R_{out}/R_{in}\right] \tag{8}$$

where τ_s is the (scattering) optical depth given by,

$$\tau_s = \frac{c^3}{8\pi\sqrt{2\pi}\sigma_v \nu^3} A_{ul} N_u \left(\frac{g_u N_l}{g_l N_u} - 1\right) \tag{9}$$

where σ_v is the line standard deviation of the line in velocity space and N_u is the column density in the upper level. In this derivation, we have assumed that the density is low enough that collisional deactivation and thermalisation of the scattered photon energy is unimportant. We neglect the effect of stimulated emission.

After subtracting the continuum, the required HCN scattering optical depth is 0.03 which results in a total column density of $7.9\pm0.5\times10^{15}$ cm^{-2}. This is not relative to the continuum since the continuum origin is not in the same part of the disk. The temperature of the resonant scattering HCN is only 240±13 K which is lower than the temperature derived from the HCN absorption lines (670±118 K). For C_2H_2 we derive a scattering column density of $6.0\pm0.9\times10^{15}$ cm^{-2} and a temperature of 464±190, and again we measure a higher temperature from the absorption lines (600±50 K). If we assume the abundance of HCN as derived from the absorption lines, this column density would result in a H column of 3×10^{22} cm^{-2}. Therefore the optical depth in the continuum of this layer would be a few times 10^{-2}.

5.4. *Abundance Gradients in the Disk*

Consider the energy level diagrams for HCN and C_2H_2 shown in Figure 15. For both species, we measure two transitions originating from the same ground state levels, yet the derived abundances are very different, by up to a factor of 10. Specifically, the abundance of HCN derived from the 13 μm transition (v_2=0-1) is much lower than that derived from the 7 μm transition (v_2=0-2). The same holds for C_2H_2 in AFGL 2136 where the abundance derived from the ground state to the $\nu_4+\nu_5$ level at 7 μm is a factor of 4 higher than the abundance derived from the ground state to the ν_5 level. As the 13 μm continuum originates from further out in the disk than the 7 μm continuum, this suggests the presence of an abundance gradient with higher abundances in the photosphere of the inner, warmer disk, out to 50 AU (Fig 13).

However, the excitation temperature derived from the rotational diagram analysis is very similar for the transitions probed at 13 μm and at 7 μm. Most importantly, the observed line profiles are similar (Figs 1, 2 & 12). The observed line width will be dominated by Keplerian rotation and suggests absorption by gas at about the same radial location. Thus we locate the absorption in all of these ro-vibrational transitions from HCN and C_2H_2 to originate from the same gas at about the same depth in the disk photosphere, at about the same radial distance from the protostar. The derived gas temperatures of these transitions are ∼600 K which is higher than the dust temperature that is characteristic for 13 μm continuum, which traces the outer regions of the disk (∼400 K assuming a radial temperature gradient $\propto T^{-0.7}$) This implies a location of the absorbing gas in the warmer inner regions. At 13 μm however, due to the lack of absorbing species, the outer disk will contribute to the continuum, and only very little to the absorption feature. This dilution by continuum emission will lead to an underestimate of the abundance of the absorbing species (Fig 13). Detailed models will be required to assess the importance of this effect.

In their pioneering study of C_2H_2 absorption lines in the spectrum of Orion IRC2, Evans et al. (1991) noted a similar effect with a 3 times higher column density derived from the $\nu_4+\nu_5$ (7 μm) transition than from the ν_5 (13 μm) transition. They located the absorbing material in the protostellar photosphere and attributed this difference to a higher continuum (dust) opacity at 13 μm than at 7 μm. This would locate the C_2H_2 gas absorbing at 13 μm higher up in the photosphere where the abundance could be lower. This means that extinction can only explain around a factor of 2 difference and not the factor of up to 10 we observe. Furthermore it does not explain the similar line profile and temperatures observed at 7 and 13 μm. Barentine & Lacy (2012) have seen the same effect for C_2H_2 absorption in the spectrum of NGC 7538 IRS9. They attributed this to a filling in of absorption by resonant scattering which would be more important for the fundamental (ν_5) band than for the combination band ($\nu_4+\nu_5$) (Fig 15). However, for material along the line of sight towards the continuum source, resonant scattering does not play a role as this line scattering process emits into 2π steradians. Moreover, even in the depth of the absorption band, the photon emission is dominated by continuum processes rather than line transitions because the continuum opacity is much larger than the line opacity.

The rotation diagrams of HCN and C_2H_2 at 7 μm reveal non-linearity. Line profiles of low and high J of these species are consistent with each other which implies that these lines originate from the same physical component (Figs 1 & 2). We attribute this to the presence of a temperature gradient in the disk with colder gas higher up in the disk photosphere absorbing more predominantly in the lowest rotational transitions. The fact that this is only observed in these two species, and not, for example, in CS, suggests that these species have a more extended vertical distribution in the disk measuring a relatively steep vertical temperature gradient along the disk photospheres. This could reflect that CS absorption is more concentrated close to $\tau_c = 2/3$ than HCN and C_2H_2. A full chemical and radiative transfer modelling effort would be required to ascertain the exact structure of the disk photospheres, however this is beyond the scope of this paper.

In AFGL 2591, all species are at the same temperature. It is therefore plausible that absorption by all species originates in the same gas. For AFGL 2136 however, a scatter of rotational temperatures of the molecules, indicative

of the scatter seen in ISO-SWS studies (Boonman et al. 2003; Boonman & van Dishoeck 2003; Keane et al. 2001; Lahuis & van Dishoeck 2000), reveals complex temperature variations with wavelength. This is a reflection of the interplay between the vertical and radial temperature gradients which will require radiative transfer modelling to disentangle. As a result of the grey atmosphere in the disk, all wavelengths will probe to the same depth in the disk. However, due to a combination of the disk being larger at longer wavelengths, and a decrease in the density with increasing radius from the central star, the photosphere layer structure is such that longer wavelengths probe to deeper layers of the mid-plane where the temperatures are higher (Figure 13)

In contrast to C_2H_2 and HCN, the spectra do not show absorption lines associated with the N-H bending mode of NH_3 in the EXES data range. As the umbrella mode (at 10 μm) is 5 times stronger than the N-H bending mode, the inferred abundance derived from the 10 μm would not give rise to discernible absorption features at 6 μm. However, we can exclude much higher NH_3 abundances in the region responsible for the 6 μm continuum emission. So, unlike for C_2H_2 and HCN, NH_3 does not show a strong increase in abundance in the radial (inwards) direction.

In the discussion of 3 & 6 μm H_2O absorption lines, Indriolo et al. (2020) already emphasised that absorption lines originate from a total optical depth of 2/3 which for strong lines is higher up in the disk photosphere than for weaker lines. Our complete 5-8 μm spectra of these two sources contains hundreds of H_2O lines. This will allow a much more detailed analysis of the origin and distribution of H_2O in the disk photosphere and we will come back to this in Barr et al. 2020 (in prep).

5.5. *Vibrationally Excited Absorption*

As presented in section 4.1.1 and 4.21, the vibrational temperatures for ^{12}CO are 623±292 K and 490±39 K for AFGL 2591 and AFGL 2136, respectively. These are in agreement with the rotational temperatures for ^{13}CO and $C^{18}O$ which suggests that CO is in vibrational equilibrium. The vibrational temperatures for the ν_5 band of C_2H_2 are 670±95 K and 494±139 K for AFGL 2591 and AFGL 2136, respectively. Again these are in agreement with the rotational temperatures which suggests that this band is in vibrational equilibrium. Knez et al. (2009) noted the presence of vibrationally excited transitions (C_2H_2 $2\nu_5 - \nu_5$) in their spectrum of NGC 7538 IRS1 and concluded that this must imply very dense gas.

Collisional coupling of the rotational population to the temperature of the gas requires densities in excess of $\sim 10^{10}$ cm^{-3}. This limit is consistent with densities in protoplanetary disks, therefore the presence of such high density gas would further imply the presence of a dust disk that dominates the continuum emission for this source. The scale height of the disk is given by $H = C_s/\Omega_k$ with C_s the sound speed ($\sim$ 2 kms^{-1} for 600 K) and $\Omega_k = v_k/r$ with v_k the Keplerian velocity and r the distance to the star. v_k is 30 kms^{-1} at a distance of 50 AU from a 50 $M_\odot$ star. This scale height would correspond to a dust optical depth of unity or $\sim 7{\times}10^{22}$ H-nuclei/cm^2. This results in a density of

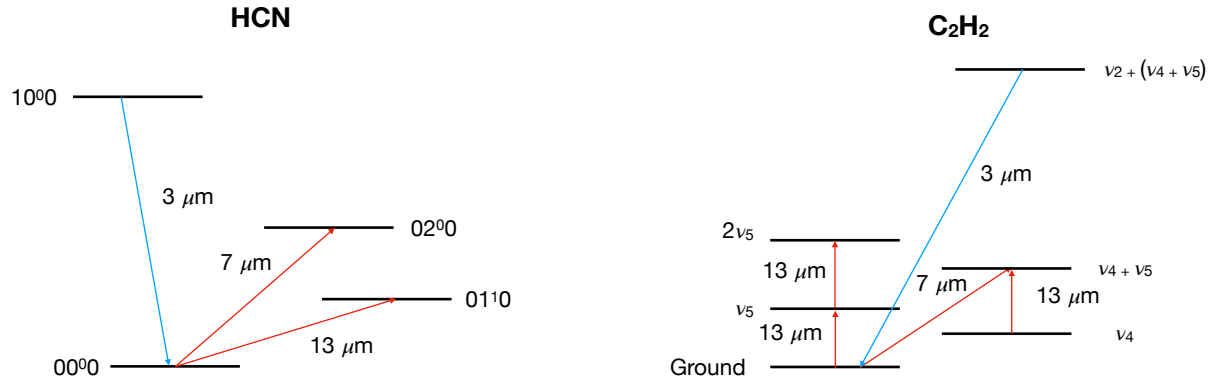

Figure 15. Energy level diagrams indicating the observed transitions of HCN (left) and C_2H_2 (right). The wavelength at which each vibrational transition is observed is indicated. Red arrows indicated transitions seen in absorption and blue arrows transitions seen in emission.

$\sim 1{\times}10^9$ cm^{-3}. Hence, the radiation field plays an important role in the population of the molecular gas. As gas in the photosphere of the disk receives only radiation from 2π steradians, the molecular excitation temperature is given by (Tielens 2005),

$$T_x/T_R = 1 + (kT_x/h\nu)\ln[2] \tag{10}$$

in the absence of collisions. T_x is the excitation temperature and T_R is the radiation temperature. As a result, the excitation temperature will be about 25 % lower than the radiation field temperature. For a reduced black body, collisional excitation dominates over radiative pumping if:

$$\frac{W}{exp(h\nu/kT_R)} \lesssim \frac{n}{n_{crti}} \tag{11}$$

where W is the dilution factor, n is the density and n_{crit} is the critical density (Tielens 2005). For $W = 0.5$, this occurs for $n > 1.7 \times 10^{10}$ cm^{-3} for the species considered here. As the actual density is likely only 10^9 cm^{-3}, the radiation field couples the level populations of these species to the continuum (dust) temperature. This implies that we observe weak scattering lines in our spectra.

In both sources, the ^{12}CO v=0-1 transitions go close to zero, with the low J lines being saturated. Therefore these are strong scattering lines and the ^{12}CO v=0-1 scattering line opacity is strong compared to the continuum opacity. This implies that collisional de-excitation is unimportant and hence the density is much less than the critical density for the v=0-1 ro-vibrational transitions of CO (10^{10} cm^{-3}).

For AFGL 2136, we derived a C^{16}O abundance that was higher than the typical value of $1{\times}10^{-4}$ based on the C^{18}O abundance. Since the ^{12}C^{16}O absorption lines are saturated in this source, we can make an estimate on what the dust opacity per H-atom should be for these values to agree. If we set the line-to-continuum ratio equal to 1, using equation 5 we calculate a dust opacity per H-atom of $5.3{\times}10^{-22}$ cm^2/H-nucleus. Taking this value instead of that quoted in section 5.2 would reduce the calculated absolute abundances in AFGL 2136 by an order of magnitude.

5.6. *The Schematic Structure of AFGL 2136 and AFGL 2591*

5.6.1. *AFGL 2136*

In order to place our results in context with respect to the specifics of each source, we outline a proposed schematic in Figure 16. For AFGL 2136, as mentioned in section 4.3, at a spatial resolution of 0.2″, an unresolved disk-like structure is observed in SiO emission at the systemic velocity, 22 kms^{-1}, which traces a disk wind out to 250 AU (Maud et al. 2018, 2019). At higher spatial resolution however, of 0.02″, SiO kinematics are observed to follow the H_2O Keplerian disk (Maud et al. 2019) on scales <120 AU.

In the H_2O velocity map and position-velocity diagrams that are presented by Maud et al. (2019), this disk is centred at around 26 kms^{-1} and is seen almost edge-on. The IR absorption that we detect at 26 kms^{-1} is associated with gas in the centre of the Keplerian disk. Therefore we propose that our IR absorption observations trace the minor axis of the disk seen in H_2O emission. This is further supported by the high temperatures that we measure of around 400-600 K (Table 3) which suggest that gas seen in the IR comes from warm gas close to the protostar.

H_2O emission is present across the entire extent of the dust disk. The line width of the 232 GHz H_2O line is broader than the line widths of the absorption lines, which would suggest that the absorption actually probes regions further out in the disk. This may be reconciled however by considering the 1.3 mm continuum image in Figure 1b of Maud et al. (2019) where clumps are observed to occur in the disk along the minor axis. These clumps are observed as peaks in the 1.3 mm continuum image. Indriolo et al. (2020) propose that, assuming the continuum structure is the same in the MIR as it is in the sub-mm, locating the H_2O absorption in these clumps would explain the difference in line width between the disk absorption and emission. One of these clumps coincides with the velocity of the absorption lines (26 kms^{-1}) of the species we discuss here and occurs about 50 AU from the protostar. It should be noted that there is no obvious sign of the 33 kms^{-1} clump, which is present in H_2O absorption and 1.3mm continuum, for any of the other molecules except perhaps CO, as seen from the v=2-0 band at 2 μm (Goto et al. 2019) and marginally in a handful of the lines in Figure 10.

Since the sub-mm observations show the H_2O $5_{5,0} - 6_{4,3}$ $\nu_2 = 1$ line is in emission (Maud et al. 2019), the disk will be optically thin at sub-mm wavelengths. For interstellar dust properties at 230 GHz, $N_H = N(H) + 2N(H_2)$ must be less than $2{\times}10^{26}$ cm^{-2} to be in the optically thin regime (Draine 2003). This line provides support for the presence of strong temperature gradients in the disk. It originates from a level $\sim$ 3500K above the ground and its emission peaks

at a radius of about 50 AU. The very high energy required to excite the H_2O emission line requires that it is produced in a very hot environment. This suggests that the line emission originates in the mid-plane of the disk where viscous heating originates, while the absorption lines that we study at the optically thick, mid-IR wavelengths originate from about the same radial location but then in the much cooler, disk photosphere.

The line width of the 22 kms^{-1} velocity component of CO absorption is narrow (2 kms^{-1}; Fig 9). Combined with the low temperature of only 27 K and difference in peak velocity, this suggests that this contribution comes from the cloud or surrounding envelope but not the disk.

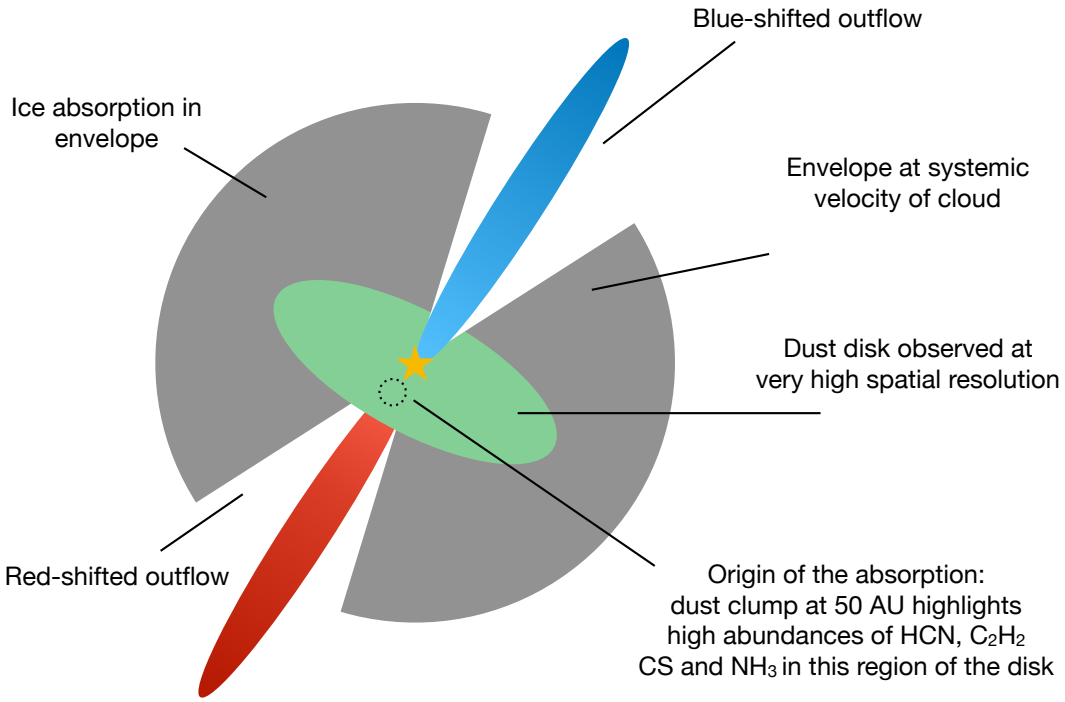

Figure 16. Cartoon schematic illustrating the different physical components in the large scale environs of the hot cores discussed. Drawing is not to scale.

5.6.2. *AFGL 2591*

In the case of AFGL 2591 the picture is less clear. We observe 5 different velocity components of ^{13}CO in absorption. This points to a complex environment in this hot core, which has been previously illustrated by van der Tak et al. (1999). These authors suggest that the different CO components are picked up along the cavity walls excavated by the outflow which points towards the observer, implying that any disk in this source would be seen face-on. The main velocity component in the IR at -10 kms^{-1} is seen in all of the species presented in section 4.1, not just CO. There have been several studies that point towards the presence of a disk in AFGL 2591, despite no disk being spatially resolved (Wang et al. 2012; van der Tak 2006; Preibisch et al. 2003; van der Tak & Menten 2005). Sub-mm observations at 0.5″ spatial resolution suggest the presence of a disk wind (Wang et al. 2012). Line profiles best match sub-Keplerian motion along with a contribution from expansion which Wang et al. (2012) attribute to a disk structure with a wind blowing across the surface layer. van der Tak (2006) find evidence for a face-on disk in H_2O and dust emission on scales of $<$ 800 AU. In this study, the emission lines are still centred at -5.5 km^{-1} with a line width of up to 5.4 kms^{-1}. The beam size of the observations was 2-0.9″, and combined with the line profiles shows that the -10 kms^{-1} component is not resolved at these scales.

We propose that we are viewing AFGL 2591 down to the base of the blue-shifted outflow close to the protostar, the same as Indriolo et al. (2015) suggest for H_2O absorption towards AFGL 2591 and Barr et al. (2018) suggest for

CS. Due to the similarity in the IR absorption properties of both hot cores, and the tentative evidence for a disk in AFGL 2591, although no disk has been clearly imaged in this source, we propose a similar scenario as for AFGL 2136. The -10 kms^{-1} velocity component seen in IR absorption traces a clump in a circumstellar disk around a high mass protostar(s). It is fortuitous that this clump would also arise from close to the zero point velocity of the disk, as in AFGL 2136, and not at the extreme velocities in the disk, placing the absorption around 50 AU from the protostar. This disk is heated from the inside by viscous heating due to accretion in the mid-plane. van der Tak & Menten (2005) see tentative evidence for a compact ionised accretion flow onto the protostar for AFGL 2591, although results may also be consistent with dust emission from a disk. We propose that the other velocity components seen in CO are also due to dust clumps in the disk, as in AFGL 2136. These are present only in CO which is omnipresent throughout the disk.

In a recent sub-mm study of rotational transitions of COMs by Gieser et al. (2019), the temperature and density structure of AFGL 2591 is modelled along with chemical complexity. The authors find that, at a spatial resolution of 0.5″, the source is not resolved below 700 AU. They conclude that no disk structure is observed. Gieser et al. (2019) also show, based on modelling of the temperature distribution in AFGL 2591, that a temperature of around 700 K is reached at a radius of 56 AU from the central star, in agreement with predictions of the source size based on the CS column density and critical density (Barr et al. 2018). This is consistent with inner disk extent estimates from chemical modelling of Herbig disks (Agúndez et al. 2018; Walsh et al. 2015). For the many other simple and complex species that are detected by Gieser et al. (2019), low temperatures are derived compared to the results in Table 2, with a maximum of 212 K for HC_3N. Furthermore, the systemic velocity of -5.5 kms^{-1} is observed for all species. This would place the emission from these species in the surrounding envelope of the hot core, likely at the location of the sublimation temperature of the ices.

In the line profiles in Figure 1, NH_3 absorption is seen to occur at a peak velocity of -7 kms^{-1}, slightly more red-shifted compared to the other absorption lines. This is still blue-shifted with respect to the systemic velocity, associating the NH_3 absorption with the disk. This is supported by the high temperature that we derive for NH_3 absorption, of 870 K. The line width is also observed to be narrower than the other absorption lines. Furthermore, from Figure 1, we see that HCN and C_2H_2 absorption are slightly shifted in velocity space with respect to each other. These line profiles point towards compositional gradients in a clumpy distribution in the disk. It is difficult to ascertain the exact kinematical nature of the disk without an image of it from the sub-mm, therefore very high spatial resolution ($\lesssim 0.05$) observations of AFGL 2591 will be necessary for this.

The hot core phase in the evolution of massive stars ends when ionising radiation breaks out of the cocoon around the protostar itself and creates a hypercompact HII region. At that point, EUV and FUV photons will start to illuminate the photosphere of the disk and the temperature gradient can then be reversed. At that point, the absorption lines will disappear and gas in the upper regions of the disk will radiate in emission lines. We note that several sources in the neighbourhood of AFGL 2591 are connected with ionised gas (Johnston et al. 2013) and hence have already entered in this subsequent phase. We surmise that low mass protostars in the class 0 phase will also show molecular absorption lines in their mid-IR disk spectrum. Finally, we note that ultra-luminous infrared galaxies (ULIRGS) show molecular absorption lines in their mid-IR spectrum (Spoon et al. 2013) also indicative of an outwardly decreasing temperature gradient in an optically thick, grey atmosphere.

5.7. *Chemistry in the warm and dense disk photosphere*

The chemistry of the inner regions of TTauri and Herbig disks has been modelled extensively, including HCN, C_2H_2, NH_3 CH_4, CS and H_2O (Markwick et al. 2002; Willacy & Woods 2009; Walsh et al. 2010; Agúndez et al. 2008, 2018), with high abundances of these species predicted to arise due to high temperature gas phase chemistry (Agúndez et al. 2018; Walsh et al. 2015). For Herbig disks, the high abundance region is expected to be larger and extend to further out regions of the disk than TTauri disks due to the higher temperatures involved, although this is contrary to observations (Pontoppidan et al. 2010; Fedele et al. 2011). Detailed modelling studies of the chemistry of massive disks have not been carried out, yet. These would need to be undertaken to determine the exact nature of the chemistry in these disks which may be quite different due to the much higher masses and luminosities of the central object, and also the different heating mechanism which results in an outwardly decreasing temperature gradient in the vertical direction. However, if the same trend of increasing abundance with mass of the disk applies, we can expect that massive disks will show even larger abundances to further out distances in the disk from the protostar, compared with Herbig and TTauri disks.

High abundances of C_2H_2 and HCN are characteristic of chemistry in warm, dense gas (Agúndez et al. 2008; Bast et al. 2013). When C and N are broken out of their main reservoir, CO and N_2, high temperatures will allow the reaction of C with H_2 to CH to dominate the chemistry and a rich chemistry ensues with high abundances of C_2H_2 and HCN, as well as CH_4 and NH_3. The chemical models of TTAuri and Herbig disks rely on UV and X-ray photons to break the C and N out of their very stable main parent species. That is relevant for these objects where the stellar photons freely impinge on the photosphere of the disk. However, as the presence of absorption lines attests, disks around these massive stars do not have a photon-dominated region (PDR) surface. The destruction of N_2 and CO must therefore rely on cosmic ray ionisation. Cosmic ray ionisation of H_2 will lead to protonated H_2 and this proton can be handed over to CO and N_2. However, dissociative recombination of these protonated species will merely reform the parent species without breaking the strong bonds involved. The formation of C and N atoms requires then cosmic ray ionisation of helium.

We can then derive a minimum timescale for the disk by requiring that each cosmic ray ionised helium atom leads to either C_2H_2 or HCN. This results in

$$\tau_{chem} = \frac{X\,(C2H2) + X\,(HCN)}{X\,(He)\,\zeta_{CR}} \quad , \tag{12}$$

where $X\,(i)$ is the abundance of species i and ζ_{CR} is the cosmic ray ionisation rate for which we take the nominal value of 3×10^{-17} s^{-1} commonly adopted for molecular clouds. Adopting a He abundance of 0.06 (Peimbert et al. 2007) we derive a timescale of $7.3\pm0.5 \times 10^5$ yr and $6.2\pm0.5 \times 10^5$ yr for AFGL 2591 and AFGL 2136 respectively. These timescales are consistent with these two objects being similar in evolutionary stage (Boonman & van Dishoeck 2003). With the recently modelled values for the cosmic ray ionisation rate towards hot cores being up to 10 times greater than the value we have adopted here (Barger & Garrod 2020; Padovani et al. 2015, 2016), we place an upper limit on these calculated chemical timescales. This timescale compares to an age of 2×10^4 yr based on chemical modelling of AFGL 2591 on scales of $> 0.4\,''$ (Doty et al. 2002; Gieser et al. 2019).

Indriolo et al. (2013, 2020) detect H_2O absorption in the K band in AFGL 2136 which means that this innermost region still has H_2O present. We expect that H_2O and CO will be omnipresent throughout the disk photosphere, tracing the entire extent of the disk seen in H_2O emission at 232 GHz, and do not show abundance gradients. H_2O gas-phase formation at high temperature has a low energy barrier of 1736 K (McElroy et al. 2013). Enhanced abundances of H_2O are predicted to occur for temperatures greater than 250 K (Charnley 1997; Doty et al. 2002).

The abundance of HCN and C_2H_2, however, will be strongly influenced by chemistry. Both HCN and C_2H_2 require high temperature gas for their formation as the first step in the chemical pathway to either of these species (the conversion of C to hydrocarbons through reaction C+H_2 -> CH + H) has a high activation barrier of 12,000 K (Bast et al. 2013). Thus, due to the lower temperature in the outer regions of the disk, chemical enhancement is confined to the inner region only. In the inner dense warm gas regions, however, three body reactions will dissociate H_2 and atomic H will break OH out of H_2O. The OH radical will eventually burn these hydrocarbons to CO (Kress et al. 2008). Hence, we expect that HCN and C_2H_2 will occupy a small region in the disk limited on the inside by this burning process and on the outside by kinetics in the low temperature gas (Fig 13).

However, since the size of the dust disk gets larger with wavelength, the continuum source will be larger at 13 μm than at 7 μm (Fig 13). The longer wavelength continuum will be dominated by lower temperature regions further out in the disk. The consequent abundance gradient will result in a filling in of absorption lines at these wavelengths by dust emission from the photosphere in the outer regions, which has low abundances of absorbing molecules. This results in a dilution of the observed flux at 13 μm, affecting the relative strength of 7 and 13 μm absorption bands (cf., section 5.4), hence we infer a strong radial gradient in the HCN and C_2H_2 abundance.

Agúndez et al. (2008, 2018) and Walsh et al. (2015) find that the chemistry of HCN and C_2H_2 in the inner region of disks is similar, therefore it is expected that, since these species exhibit similar chemical behaviour at high temperature, it is likely that they also exhibit similar physical behaviour. Indeed, the derived gas temperatures of these bands are similar (∼600 K), both species show behaviour in the rotation diagrams characteristic of a temperature gradient, and both species exhibit an abundance gradient with wavelength. Furthermore, L-band data of AFGL 2591 show that HCN and C_2H_2 are detected in emission and NH_3 is not detected.

Upper limits of NH_3 emission from the inner disks of TTauri disks suggests that NH_3 is efficiently destroyed in the inner disk and that the main N-carriers are N_2 followed by HCN (Pontoppidan et al. 2019). Disk models, on the other hand, with full nitrogen chemical networks predict gas-phase NH_3 abundances of 10^{-5} or 10^{-6} with respect to H for

the majority of N originating in NH_3 or N_2 respectively (Schwarz & Bergin 2014). We have very accurately determined the NH_3 abundance in the disks of both AFGL 2591 and AFGL 2136. High abundances (10^{-6}) suggest that NH_3 is one of the main N-carriers, along with HCN and most likely N_2, in the inner region.

5.8. *Molecular absorption lines in the IR spectra of massive protostars*

This study focuses on AFGL 2136 and AFGL 2591, however several other hot cores have been observed before at high spectral resolution at MIR wavelengths using a few specifically chosen settings. These studies reveal MIR transitions in absorption towards hot cores (Mitchell et al. 1989, 1990; Evans et al. 1991; Knez et al. 2009; Barentine & Lacy 2012; Rangwala et al. 2018; Dungee et al. 2018; Indriolo et al. 2013, 2015, 2020). Hot cores have also been observed at low spectral resolution in the MIR with ISO (Lahuis & van Dishoeck 2000; Keane et al. 2001; Boonman et al. 2003; Boonman & van Dishoeck 2003).

All theses studies conclude that absorption lines in the IR originate in a region in very close proximity to the illuminating protostar. In the past, molecular absorption lines in the mid-IR spectra of high mass protostars have been interpreted in terms of either a disk, or small foreground blobs along the line of sight towards the star. However, if the continuum emission is associated with a circumstellar disk, as in the case for AFGL 2136, these blobs must by necessity cover a substantial fraction of the disk surface. Moreover, as the rotational temperature is very high, this gas must be located close to a heating source. It is then likely that this gas is really associated with the surface layers of an internally heated disk. This also explains, in a natural way, the observed peak velocity and width of these absorption lines.

In view of the presence of absorption lines, a temperature gradient of the form we proposed in section 5.1 must also apply to these other hot cores. Viscous heating from the mid-plane up results in a vertically decreasing temperature gradient. These results are in contrast to TTauri stars and Herbig AeBe stars whose MIR spectra are dominated by strong molecular emission lines (Carr & Najita 2011) indicative of an inwardly decreasing temperature gradient in the vertical direction. The high abundances measured indicate the presence of a hot gas-phase chemistry, which has been discussed in section 5.7. This chemistry implies a timescale for these hot cores between 7×10^4 yr and 7×10^5 years. We speculate that during the deeply embedded phase of low mass protostars, the Hot Corino gas (Ceccarelli 2008) is characterised by mid-IR absorption lines with a disk with an outwardly decreasing temperature gradient in the vertical direction.

Several massive YSOs show hot CO v=2-0 emission at NIR wavelengths which is best described as arising from a circumstellar disk. This emission arises from within the dust sublimation radius where the disk is gaseous (Ilee et al. 2013). One of the hot cores in this survey, AFGL 4176, shows CO v=2-0 bandhead emission, as well as H_2O and CO absorption at 2.5 μm and 4.6 μm respectively (A. Karska et al. 2020, in preparation). The absorption is indicative of an outwardly decreasing temperature gradient in the vertical direction, therefore this may be a general characteristic possessed by disks around massive stars, which would suggest that these disks are accreting.

6. CONCLUSIONS

We have presented here results of the first ever full spectral survey of the 4.5-13 μm region at high spectral resolution towards a hot core, which utilises EXES, TEXES and iSHELL. MIR ro-vibrational lines are observed to be in absorption in CO, CS, HCN, C_2H_2 and NH_3. However HCN and C_2H_2 in the L-band are seen in emission towards AFGL 2591. A rotational diagram analysis reveals that the absorption lines probe high temperature gas of the order of 600 K. Line profiles reveal a difference in line width and peak velocity when compared to the surrounding envelope which is traced by sub-mm emission lines. IR absorption lines are broader and offset by several kms^{-1} with respect to sub-mm lines seen by single-dish telescopes.

A disk around AFGL 2136 has been inferred at MIR wavelengths and has recently been resolved as a Keplerian disk with ALMA. There is also evidence for a potential disk around AFGL 2591. We propose that the IR absorption lines trace this circumstellar disk and due to the presence of absorption lines, we propose that this disk is characterised by an outwardly decreasing temperature gradient in the vertical direction, with viscous heating due to accretion originating in the mid-plane. Temperatures and line profiles are consistent with clumps in these disks at a distance of 50 AU from the protostar.

We have derived abundances for all species detected using stellar atmosphere theory to account for the temperature gradient in the disk. We derive high abundances for all species, of the order 10^{-6} with respect to H. In view of the lower temperature of the emission lines in the L-band, we conclude that these lines trace gas higher up in the photosphere of the disk.

Differences of up to an order of magnitude in the abundances of transitions that trace the same ground state level are measured for HCN and C_2H_2 in both hot cores. The abundance derived from the transition at 7 μm is higher than that at 13 μm, however the temperature and line profiles of the two transitions are in agreement. We conclude that the transitions originate from the same gas, whilst we attribute the abundance difference to filling in of absorption lines by dust continuum emission from the outer part of the disk where the abundance of these species is low. The extent of the outer part of the disk increases with wavelength, thus diluting the gas at 13 μm more than at 7 μm. Thus abundance gradients exist in the disk with the high abundance material constrained to the inner 50 AU of the disk.

The location of the absorption coming from 50 AU from the protostar is supported by chemical models of TTauri and Herbig Ae/Be disks, where high temperatures and abundances are derived for all species observed. Comparison to these models is limited however due to the different physical structure of the disks. In the case of these massive disks, we suggest that C and N are broken out of their main reservoirs by cosmic ray ionisation. The presence of HCN and C_2H_2 emission at 3 μm implies that these species may be destroyed by OH radicals in the innermost regions of the disk resulting in a depleted region of HCN and C_2H_2 gas. Turbulent mixing then transports HCN and C_2H_2 gas to the upper, cooler layers of the disk photosphere where it is illuminated by the warm inner disk and resonant scattering produces emission lines. High abundances of NH_3 implies that this is one of the main N-bearing species at radii of around 50 AU from the central object, along with HCN and likely N_2.

Finally, MIR absorption lines have been observed along sight lines towards several other hot cores. All of these studies observe high abundances of detected species. These observations are consistent with the scenario that we propose in this paper for AFGL 2591 and AFGL 2136. Therefore MIR absorption lines indicating high rotational temperatures towards hot cores may be an indication of massive disks at the centre of these sources.

Based [in part] on observations made with the NASA/DLR Stratospheric Observatory for Infrared Astronomy (SOFIA). SOFIA is jointly operated by the Universities Space Research Association, Inc. (USRA), under NASA contract NAS2-97001, and the Deutsches SOFIA Institut (DSI) under DLR contract 50 OK 0901 to the University of Stuttgart. A.G.G.M.T thanks the Spinoza premie of the NWO. D.A.N gratefully acknowledges the support of an USRA SOFIA grant, SOF05-0041. The authors also thank Rachel Smith and Agata Karska for their helpful contributions to this paper, as well as the anonymous referee for the constructive suggestions for improving the manuscript.

APPENDIX

A. DERIVATION OF MILNE-EDDINGTON SOLUTION

We will adopt a linear source function on the continuum optical depth scale, τ_c:

$$S = a + b\tau_c = a + p_\nu \tau_\nu \tag{A1}$$

where $p_\nu = b/(1+\eta_\nu)$ transforms the continuum optical depth scale to the total line plus continuum optical depth scale, τ_ν. Here η_ν is the line-to-continuum opacity ratio at frequency ν. Ignoring scattering in the continuum, the Milne-Eddington approximation leads to the residual flux of an absorption line (Mihalas 1978):

$$R_\nu = \frac{F_\nu}{F_c} = \frac{2(p_\nu + \sqrt{3\lambda_\nu}a)}{(1+\sqrt{\lambda_\nu})(b+\sqrt{3}a)} \tag{A2}$$

Examining this solution we see that, in the case of a pure absorption line, the residual flux will not be equal to 1, even for a strong line. For a pure absorption line, $\epsilon = 1$ and $\lambda_\nu = 1$, where the thermalisation length is:

$$\lambda_\nu = \frac{1+\epsilon\eta_\nu}{1+\eta_\nu} \tag{A3}$$

where ϵ ranges from 0 to 1 and is a measure of the thermalisation of the line, such that the fraction of scattered and absorbed photons during line formation is $(1-\epsilon)$ and ϵ, respectively (see section B for further definition).

For a weak line the residual flux is given by,

$$R_\nu = \frac{\sqrt{3}a + b/(1+\eta_\nu)}{\sqrt{3}a + b} \tag{A4}$$

This leads to a central depth of

$$A_0 = 1 - R_\nu = \frac{b(1-(1+\eta_\nu)^{-1})}{b+\sqrt{3}a} \tag{A5}$$

For weak lines ($\eta_\nu << 1$), we can use the Taylor expansion to arrive at,

$$A_0 \simeq \frac{\eta_\nu}{1+\sqrt{3}a/b} \tag{A6}$$

Thus the strength of the line scales with η_ν. For a strong line ($\eta_\nu \to \infty$), the central depth of the line is given by,

$$A_0 = \frac{b}{b+\sqrt{3}a} \tag{A7}$$

Thus, if the column density is large enough, lines will go down to the same value, A_0, independent of the line column density. In this case, the continuum optical depth will be small and hence the stellar atmosphere approximation will break down as the line opacity will be much larger than the continuum opacity.

The expression in eqn A6 is the same for the weak line approximation in a pure scattering line (Collins 2003). This is because for weak lines the opacity is dominated by the continuum and a scattered photon is lost to the continuum opacity process (thermalisation). So, line scattered photons do not stray from the place where they initially interacted and we will still measure the flux at a depth of $\tau = \tau_c + \tau_l = 2/3$. Strong scattering lines, however, will go to 0 residual flux as photons at any depth will wander around until they are lost.

If we consider equation 4 in section 5.2, the source function gradient is given by $Y = (1 + 3a/2b)^{-1}$ (Mihalas 1978). For a we will adopt the Planck function at the temperature derived from the rotation diagram and $b = 3/8X_0a$, where X_0 is given by eqn A9 below. For a grey atmosphere, we can evaluate the source function gradient to arrive at (Mihalas 1978, section 10.2),

$$Y = \frac{X_0}{X_0 + 4} \tag{A8}$$

with

$$X_0 = \frac{h\nu_0/kT_0}{1 - e^{-h\nu_0/kT_0}} \tag{A9}$$

with T_0 the temperature at the depth where the continuum originates and ν_0 the frequency of the lines. At the frequency of the absorption lines ($\sim 5 \times 10^{13}$ Hz) and the excitation temperature derived from the rotation diagrams, X_0 is in the range 3-19.

B. DERIVATION OF STELLAR ATMOSPHERE PARAMETERS

Let us consider the equation of radiative transfer:

$$\mu \frac{dI_\nu(\mu)}{dx} = (\kappa_\nu^c + \kappa_\nu^L + \sigma)I_\nu - \epsilon_\nu^c - \epsilon_\nu^L - \sigma J_\nu \tag{B10}$$

where κ_i are the absorption coefficients and ϵ_i are the emission coefficients. σ is the scattering contribution to the total absorption coefficient. Assuming that we have LTE in the continuum ($\epsilon_\nu^c/\kappa_\nu^c = B_\nu(T)$) and that scattering is negligible in the continuum ($\sigma << \kappa_\nu^c$), we come to:

$$\mu \frac{dI_\nu}{dx} = (\kappa_\nu^c + \kappa_\nu^L)\big[I_\nu - \frac{\kappa_\nu^c}{\kappa_\nu^c + \kappa_\nu^L}B_\nu - \frac{\kappa_\nu^L}{\kappa_\nu^c + \kappa_\nu^L}S_\nu^L\big] \tag{B11}$$

Now let us define $\eta_\nu = \dfrac{\kappa_\nu^L}{\kappa_\nu^c}$ and $\lambda_\nu = \dfrac{1+\epsilon\eta_\nu}{1+\eta_\nu}$. Making a change of variables from x to τ_ν:

$$d\tau_\nu = (\kappa_\nu^c + \kappa_\nu^L)dx = k_\nu^c(1+\eta_\nu)dx \tag{B12}$$

for the equation of radiative transfer we arrive at the Milne-Eddington approximation:

$$\mu \frac{dI_\nu}{d\tau_\nu} = I_\nu - \lambda_\nu B_\nu - (1-\lambda_\nu)\int_0^\infty \phi_\nu J_\nu d\nu \tag{B13}$$

The definition of the thermalisation of the line ϵ used in equations A7 and A4 is:

$$\epsilon = \frac{\kappa_c}{\kappa_c + \sigma} \tag{B14}$$

where κ_c is the continuum opacity and σ the term from equation B10. Note that this is not the same as the emission coefficient in the equation of radiative transfer, ϵ_ν^c (Eqn B10), but rather this ϵ without a subscript is that from section 5.2. When scattering is important, $\sigma \to \infty$, thus ϵ becomes 0. When scattering is negligible, $\sigma = 0$ therefore $\epsilon = 1$.

REFERENCES

Adams, S. C., Ádámkovics, M., Carr, J. S., Najita, J., & Brittain, S. D. 2019, ApJ, 871, 173

Agúndez, M, Roueff, E., LePetit, F & Le Bourlot, J. 2018, A&A, 616, A19

Agúndez, M., Cernicharo, J & Goicoechea, J. R. 2008, A&A, 483, 831

Asplund, M., Grevesse, N., Sauval, A. J., & Scott, P. 2009, ARA&A, 47, 481,

Bally, J., Lada, C. J. 1983, ApJ, 265, 824

Bast, J. E., Brown, J. M., Herczeg, G. J., van Dishoeck, E. F., & Pontoppidan, K. M. 2011, A&A, 527, A119

Bast, J. E., Lahuis, F., van Dishoeck, E. F., & Tielens, A. G. G. M. 2013, A&A, 551, A118

Barentine, J & Lacy, J. 2012, ApJ, 757, 111

Barger, C. J., & Garrod, R. T. 2020, ApJ, 888, 38

Barr, A. G., Boogert, A., DeWitt, C. N., Montiel, E., et al. 2018, ApJL, 868, L2

Beltrán M. T., Cesaroni R., Neri R., Codella C. 2004, ApJ, 601, L187

Beuther, H., Churchwell, E. B., McKee, C. F., & Tan, C. J. 2007, Protostars and Planets V, ed. Reipurth, Bo., Jewitt, David., & Keil, Klaus, University of Arizona Press, Tucson, 951

Bik, A., Kaper, L., & Waters, L. B. F. M. 2006, A&A, 455, 561

Boley, P. A., Linz, H., van Boekel, R., et al. 2013, A&A, 558, A24

Boonman, A. M. S., van Dishoeck, E. F., Lahuis, F., & Doty, S. D. 2003, A&A, 399,1063

Boonman, A. M.S., van Dishoeck, E. F. 2003, A&A, 403, 1003

Carey, S. J., Clark, F. O., Egan, M. P., et al. 1998, ApJ, 508, 721

Carr, J. S., Evans, N. J., Lacy, J. H., & Zhou, S. 1995, ApJ, 450, 667

Carr, J. S., Najita, J.R. 2011, ApJ, 733, 102

Cassen, P., & Summers, A. 1983, Icarus, 53, 26

Ceccarelli, C. 2008, Organic Matter in Space Proceedings IAU Symposium, No. 251, 2008, S. Kwok & S. Sandford, eds.

Cesaroni, R. 2005, Ap&SS, 295, 5

Cesaroni, R., Galli, D., Lodato, G., Walmsley, C. M. & Zhang, Q. 2007, Protostars and Planets V, ed. Reipurth, Bo., Jewitt, David., & Keil, Klaus, University of Arizona Press, Tucson, 197

Charnley, S. B. 1997, ApJ, 481, 396

Clarke, M., Vacca, W. D., & Shuping, R. Y. 2015, Astronomical Society of the Pacific Conference Series, Vol. 495, Astronomical Data Analysis Software anSystems XXIV (ADASS XXIV), ed. A. R. Taylor & E. Rosolowsky, 355

Collins, G. W. 2003, The Fundamentals of Stellar Astrophysics, (Web Edition; pg 345)

Cooper, H. D. B., Lumsden, S. L., Oudmaijer, R. D., et al. 2013 MNRAS, 430, 1125

Cushing, M. C., Vacca, W. D., & Rayner, J. T. 2004, PASP, 116, 362

D'Alessio, P., Cantó, J., Calvet, N., & Lizano, S. 1998, ApJ, 500, 411

Davies, B., Lumsden, S. L., Hoare, M. G., et al. 2010, MNRAS, 402, 1504

de Wit, W. J., Hoare, M. G., Oudmaijer, R. D., et al. 2011, A&A, 526, L5

Doty, S. D., van Dishoeck, E. F., van der Tak, F. F. S., & Boonman, A. M. S. 2002, A&A, 389, 446

Draine, B. T./ 2003, ARA&A, 41, 241

Dullemond, C. P., Hollenbach, D., Kamp, I, & D'Alessio, P. 2007, Protostars and Planets V, ed. Reipurth, Bo., Jewitt, David., & Keil, Klaus, University of Arizona Press, Tucson, 555

Dullemond, C. P, & Monnier, J. D. 2010, ARA&A, 48, 205

Dungee, R., Boogert, A., DeWitt, C. N., Montiel, E., et al. 2018, ApJL, 868, L10

Egan, M. P., Shipman, R. F., Price, S. D., et al. 1998, ApJ, 494, L199

Evans, N. J., Lacy, J. H., & Carr, J. S. 1991, ApJ, 383, 674

Faure, A., Hily-Blant, P., Le Galm R., et al. 2013, ApJL, 770, l2

Fedele, D., Pascucci, I., Brittain, S., et al. 2011, ApJ732, 106

Fedriani, R., Caratti o Garatti, A., Koutoulaki, M., et al. 2020, A&A, 633, A128
Gibb, E. L., Whittet, D. C. B., Boogert, A. C.. A., & Tielens, A. G. G. M. 2004, ApJS, 151, 35
Gieser, C., Semenov, D., Beuther, H., et al. 2019, A&A, A&A, 631, A142
Gordon, I. .E., Rothman, L. S., Hill, C. et al. 2017, JQSRT, 203, 3
Goto, M., Geballe, T. R., Harju, J., et al. 2019, A&A, 632, A29
Henning, T., Feldt, M., & Stecklum, B. 2002, Hot Star Workshop III: The Earliest Phases of Massive Star Birth, ed. Paul A. Crowther, ASP Conference Series, Vol 267
Herbst, E., van Dishoeck, E. F. 2009, ARA&A, 47, 427
Ilee, J. D., Wheelwright, H. E., Oudmaijer, R. D. 2013, MNRAS, 429, 2960
Ilee, J. D., Cyganowski, C. J., Nazari, P., et al. 2016, MNRAS, 462, 4386
Indriolo, N., Neufeld, D. A., Seifahrt, A., & Richter, M. J. 2013, ApJ, 776, 8
Indriolo, N., Neufeld., D. A., DeWitt, C. N., Richter, M. J., et al. 2015, ApJL, 802: L14
Indriolo, N., Neufeld, D. A., Barr, A. G., et al. 2020, ApJ, 894, 107
Johnston, K. G., Shepherd, D. S., Robitaille, T. P., & Wood, K. 2013, A&A, 551, A43
Johnston, K. G., Robitaille, T. P., Beuther, H., et al. 2015, ApJ, 813, L19
Kaźmierczak-Barthel, M., van der Tak, F. F. S., Helmich, F. P., et al. 2014, A&A, 567, A53
Keane, J. V., Boonman, A. M. S., Tielens, A. G. G. M., & van Dishoeck, E. F. 2001, A&A, 376, L5
Knez, C., Lacy, J. H., Evans, N. J., van Dishoeck, E. F., & Richter, M. J. 2013, ApJ, 696, 471
Kraus, S., Hofmann, K. H., Menten, K. M., et al. 2010, Nature, 466, 339
Kress, M. ., Tielens, A. G. G. M., & Frenklach, M. 2008, 5th Spitzer Conference. New Light on Young Stars: Spitzer's View of Circumstellar Disks, poster 31
Lacy, J. H., Knacke, R., Geballe, T. R., Tokunaga, A. T. 1994, ApJ, 428, L69
Lacy, J. H., Richter, M. J., Greathouse, T., Jaffe, D. T., & Zhu, Q. 2002, PASP, 114, 153
Lacy, J. H., Richter, M. J., Greathouse, T., et al. 2003, Society of Photo-Optical Instrumentation Engineers (SPIE) Conference Series, 4841, 1572
Lacy, J. H. 2013, ApJ, 765, 130
Lahuis, F., van Dishoeck, E. F. 2000, A&A, 355, 699
Lumsden, S. L., Hoare, M. G., Urquhart, J. S., et al. 2013, ApJS, 208, 11
Lynden-Bell, D., & Pringle, J. E. 1974, MNRAS, 168, 603
Mandell, A. M., Bast, J., van Dishoeck, E. F., Blake, G. A., et al. 2012, ApJ, 747, 92
Markwick, A., Ilgner, M., Millar, T. J., & Henning, Th. 2002, A&A, 385, 632
Maud, L. T., Cesaroni, R., Kumar, M. S. N., van der Tak, F. F. S., et al. 2018, A&A, 620, A31
Maud, L. T., Cesaroni, R., Kumar, M. S. N., Rivilla, V. M., et al. 2019, A&A, A&A, 627, L6
McElroy, D., Walsh, C., Markwick, A. J., et al. 2013, A&A, 550, A36
Mihalas, D. 1978, Stellar Atmospheres, (2nd Edition; W. H. Freeman; pg 211-213)
Mitchell, G. F., Curry, C., Maillard, J., & Allen, M. 1989, ApJ, 341, 1020
Mitchell, G. F., Maillard, J., Allen, M. 1990, ApJ, 363, 554
Mitchell, G. F., Maillard, J., & Hasewaga, T. I. 1991, ApJ, 371, 342
Monnier, J. D., Tuthill, P. G., Ireland, M., et al. 2009, ApJ, 700, 491
Moscadelli, L., & Goddi, C. 2014, A&A, 566, A150
Moscadelli, L., Sanna, A., Cesaroni, R., et al. 2019, A&A, 622, A206
Murakawa, K., Preibisch, T., Krau, S., & Weigelt, G./ 2008, A&A, 490, 673
Murukawa, K., Lumsden, S. L., Oudmaijer, R. D., et al. 2013, MNRAS, 436, 511
Olmi L., Cesaroni R., Hofner P., Kurtz S., et al. 2003, A&A, 407, 225
Ormel, C. W., Min, M., Tielens, A. G. G. M., et al. 2011, A&A, 532, A43
Padovani, M., Hennebelle, P., Marcowith, A., & Ferriére, K. 2015, A&A, 582, L13
Padovani, M., Hennebelle, P., Marcowith, A., & Ferriére, K. 2016, A&A, 590, A8
Patel, N. A., Curiel, S., Sridharan, T. K., et al. 2005, Nature, 437, 576
Peimbert, M., Luridiana, V., & Peimbert, A. 2007, ApJ, 666, 636
Pontoppidan, K. M., Salyk, C., Blake, G. A., et al. 2010, ApJ, 720, 887
Pontoppidan, K. M., Blake, G. A., & Smette, A. 2011, ApJ, 733, 84
Pontoppidan, K, M., Salyk, C., Banzatti, A., et al. 2019, ApJ, 874, 92
Preibisch, T., Balega, Y. Y., Schertl, D, & Weigelt, G. 2003, A&A, 412, 735
Rangwala, N., Colgan, S. W. J., Le Gal, R., Acharyya, K., et al. 2018, ApJ, 856, 9

Rayner, J. T., Tokunaga, A., Jaffe, D., Bonnet, G., Ching, M., et al. 2016, SPIE, 9908E, 84R

Richter, M. et al. 2018, Journal of Astronomical Instrumentation, 7,4

Rothman, L. S., Gordon, I. E., Babikov, Y., et al. 2013, JQSRT, 130, 4

Rygl K. L. J. et al. 2012, A&A, 539, 79

Sandell, G., Wright, M., Forster, J. R. 2003, ApJ, 590 L45

Sanna, A., Reid, M. J., Carrasco-González, C., et al. 2012, ApJ, 745, 191

Schwarz, K. R., & Bergin, E. A. 2014, ApJ, 797, 113

Setterholm, B. R., Monnier, J. D., Davies, C. L., Kreplin, A., et al. 2019, ApJ, 869, 164

Šimečková, M., Jacquemart, D., Rothman, L. S., et al. 2006, Journal of Quantitative Spectroscopy & Radiative Transfer 98, 130

Sollins P. K., Zhang Q., Keto E., and Ho P. T. P. 2005, 631, 399

Spoon H. W. W., Farrah D., Lebouteiller V., González-Alfonso E., et al. 2013, ApJ, 775, 127

Tan, J. C. 2017, Astrochemistry VII, Proceedings IAU Symposium No. 322

Tamura, M., & Yamashita, T. 1992, ApJ, 391, 710

Tielens, A. G. G. M., & Hollenbach, D. 1985, ApJ, 291, 722

Tielens, A. G. G. M. 2005, The Physics and Chemistry of the Interstellar Medium (Cambridge University Press)

Trinidad, M. A., Curiel, S., Cantó, J., et al. 2003, ApJ, 589, 386

Urquhart, J. S., Hoare, M. G., Lumsden, S. L., et al. 2012, MNRAS, 420, 1656

Urquhart, J. S., Figura, C. C., Moore, T. J. T., et al. 2014, MNRAS, 437, 1791

van der Tak, F. F S., van Dishoeck, E. F., Evans, N. J., & Bakker, E. J. 1999, ApJ, 522, 991

van der Tak, F. F. S., Boonman A. M. S., Braakman, R., & van Dishoeck, E. F. 2003, A&A, 412, 133

van der Tak, F. F. S. 2003, Star Formation at High Angular Resolution ASP Conference Series, Vol. S-221

van der Tak, F. . .S., & Menten, K. M. 2005, A&A, 437, 947

van der Tak, F. F. S., Walmsley, C. M., Herpin, F., & Ceccarelli, C. 2006, A&A, 447, 1011

Villanueva, G. L., Smith, M. D., Protopapa, S., Faggi, S., & Mandell, A. M. 2018, JQSRT, 217, 86

Walsh, C., Millar, T. J., & Nomura, H. 2010, ApJ, 722, 1607

Walsh, C., Nomura, H., & van Dishoeck, E. F. 2015, A&A, 582, A88

Wang, K. S., van der Tak, F. F. .S., & Hogerheijde, M. R. 2012, A&A, 543 A22

Willacy, K., & Woods, P. M. 2009, ApJ, 703, 479

Williams, J. P., & Cieza, L. A. 2011, ARA&A, 49, 67

Young, E. T., Becklin, E. E., Marcum, P. M., et al. 2012, ApJL, 749, L17

Zapata, L. A., Garay, G., Palau, A. 2019, ApJ, 872, 176

Zinnecker, H., & Yorke H. W. 2007, ARA&A, 45, 481

Table 4. Line Parameters for AFGL 2591. E_l is the energy of the lower level of the transition, g_l is the statistical weight of the lower level, A_{ij} is the Einstein A coefficient of the transition, v_{lsr} is the centroid velocity of the line, Δv is the FWHM of the line, τ_0 is the optical depth at line centre and N_l/N_H is the abundance in the lower level of the transition. Line data were taken from the HITRAN database (Gordon et al. 2017).

Species	Transition	λ (μm)	E_l (K)	g_l	A_{ij} (s^{-1})	v_{lsr} (kms^{-1})	Δv (kms^{-1})	τ_0	N_l/N_H ($\times 10^{-7}$)
^{13}CO v=0-1	P(1)	4.7792	5.2	6	32.4	-9.4 ±0.2	1.5	0.50 ±0.04	72.4 ±7.3
	P(2)	4.7877	15.8	10	21.5	-9.3 ±0.1	1.5	0.57 ±0.02	77.5 ±3.6
	R(2)	4.7463	15.8	10	14.2	-9.7 ±0.3	1.5	0.68 ±0.07	67.0 ±8.0
	R(3)	4.7383	31.7	14	14.8	-9.3 ±0.1	1.5	0.70 ±0.02	68.6 ±2.7
	P(3)	4.7963	31.7	14	19.3	-9.3 ±0.2	1.5	0.61 ±0.04	79.0 ±6.2
	P(4)	4.8050	52.8	18	18.2	-9.3 ±0.2	1.5	0.57 ±0.03	72.4 ±5.2
	R(5)	4.7227	79.3	22	15.5	-8.3 ±0.2	1.5	0.44 ±0.06	38.6 ±5.7
	R(6)	4.7150	111.0	26	15.8	-9.1 ±0.3	1.5	0.31 ±0.06	29.3 ±5.9
	R(9)	4.6927	237.9	38	16.4	-12.1 ±0.7	10.5	0.14 ±0.01	56.5 ±7.5
	P(9)	4.8501	237.9	38	16.4	-13.2 ±0.8	10.5	0.10 ±0.01	42.7±6.3
	R(10)	4.6853	290.8	42	16.5	-10.5 ±0.6	10.5	0.10 ±0.01	41.4 ±6.3
	R(11)	4.6782	349.0	46	16.7	-12.0 ±0.5	10.5	0.11 ±0.01	39.0 ±5.0
	P(11)	4.8689	349.0	46	16.1	-13.0 ±0.6	10.5	0.05 ±0.01	23.9 ±3.8
	R(12)	4.6711	412.3	50	16.8	-12.0 ±0.6	10.5	0.09 ±0.01	38.9 ±3.8
	R(13)	4.6641	481.1	54	16.9	-12.0 ±0.4	10.5	0.09 ±0.01	37.7 ±3.8
	R(16)	4.6437	718.8	66	17.3	-10.8 ±0.5	10.5	0.10 ±0.01	38.9 ±3.8
^{12}CO v=1-2	R(6)	4.6675	3199.5	13	33.2	-9.9 ± 0.6	7.6 ± 0.7	0.107 ± 0.007	42.7 ± 3.8
	R(7)	4.6598	3237.9	15	33.7	-8.3 ± 0.7	7.7 ± 0.8	0.112 ± 0.008	41.4 ± 6.3
	R(8)	4.6523	3281.8	17	34.1	-9.2 ± 0.4	7 ± 0.4	0.128 ± 0.006	38.9 ± 6.3
	R(9)	4.6448	3331	19	34.4	-8.6 ± 0.4	6.8 ± 0.4	0.116 ± 0.005	40.2 ± 2.5
	R(17)	4.5887	3922.5	35	36.6	-8.6 ± 0.3	6.2 ± 0.4	0.105 ± 0.005	27.6 ± 2.5
	R(18)	4.8948	4020.9	37	31.7	-7.2 ± 0.3	4.8 ± 0.4	0.086 ± 0.004	27.6 ± 2.5
	R(19)	4.9054	4124.8	39	31.4	-9.9 ± 0.8	5.2 ± 1.6	0.105 ± 0.009	30.1 ± 5.0
	R(20)	4.5694	4234.4	41	37.2	-6.3 ± 0.4	5.8 ± 0.5	0.088 ± 0.005	25.1 ± 3.8
CS v=0-1	P(8)	7.9443	84.6	17	8.1	-10.9 ± 0.5	9.7 ± 1.5	0.055 ± 0.006	12.6 ± 2.5
	R(3)	7.8212	14.1	7	7.2	-11.9 ± 0.5	8.3 ± 1.5	0.031 ± 0.004	5.0 ± 1.3
	R(4)	7.8116	23.5	9	7.4	-9.4 ± 0.5	6.2 ± 1.3	0.032 ± 0.004	5.0 ± 1.3
	R(5)	7.802	35.3	11	7.6	-10.1 ± 0.5	7.8 ± 1.3	0.039 ± 0.004	6.3 ± 1.3
	R(7)	7.7833	65.8	15	7.8	-10.4 ± 0.2	6.4 ± 0.6	0.056 ± 0.003	8.8 ± 1.3
	R(9)	7.7649	105.8	19	8	-9.5 ± 0.6	11.2 ± 1.8	0.051 ± 0.005	11.3 ± 2.5
	R(10)	7.7559	129.2	21	8	-11.1 ± 0.3	10.4 ± 0.9	0.061 ± 0.004	12.6 ± 1.3
	R(11)	7.7469	155.1	23	8.1	-12.1 ± 0.3	9.9 ± 0.8	0.06 ± 0.003	12.6 ± 1.3
	R(18)	7.6868	401.8	37	8.5	-12 ± 0.4	11 ± 1.2	0.063 ± 0.004	13.8 ± 2.5
	R(22)	7.6545	594.5	45	8.7	-12.4 ± 0.9	11.3 ± 3.7	0.081 ± 0.015	17.6 ± 6.3
	R(23)	7.6467	648.5	47	8.8	-10.3 ± 0.7	8.4 ± 1.7	0.064 ± 0.009	11.3 ± 3.8
	R(24)	7.6389	704.7	49	8.8	-5.2 ± 0.8	15.2 ± 2.2	0.06 ± 0.006	16.3 ± 5.0
	R(26)	7.6237	824.5	53	8.9	-8.4 ± 0.6	7.9 ± 2.1	0.048 ± 0.007	7.5 ± 2.5
	R(27)	7.6162	887.8	55	9	-11.2 ± 0.4	4.9 ± 1	0.076 ± 0.008	10.0 ± 2.5
	R(28)	7.6088	953.4	57	9	-10 ± 0.6	6.8 ± 1.5	0.055 ± 0.008	8.8 ± 2.5
	R(29)	7.6015	1021.5	59	9.1	-11 ± 0.4	6.7 ± 1.2	0.078 ± 0.008	12.6 ± 2.5
	]R(31)	7.5871	1164.5	63	9.2	-7.9 ± 0.9	11.5 ± 4.2	0.024 ± 0.005	5.0 ± 2.5
	R(33)	7.5731	1316.8	67	9.2	-9.1 ± 0.6	5.2 ± 1.5	0.051 ± 0.009	7.5 ± 2.5
HCN ν_2 v_2=0-1	R(11e)	13.3796	280.6	138	1.2	-11.7 ± 0.4	8.5 ± 1.1	0.098 ± 0.009	26.4 ± 3.8
	R(12e)	13.3271	331.7	150	1.2	-11.7 ± 0.7	9.4 ± 1.8	0.078 ± 0.011	23.9 ± 6.3

Table 4. continued.

Species	Transition	λ (μm)	E_l (K)	g_l	A_{ij} (s^{-1})	v_{lsr} (kms^{-1})	Δv (kms^{-1})	τ_0	N_l/N_H ($\times 10^{-7}$)
	R(13e)	13.275	387	162	1.3	-11.1 ± 0.3	8.7 ± 0.8	0.102 ± 0.007	28.9 ± 3.8
	R(14e)	13.2233	446.4	174	1.3	-9.5 ± 0.3	10.1 ± 0.8	0.096 ± 0.005	30.1 ± 3.8
	R(16e)	13.1213	578.2	198	1.3	-8.4 ± 0.6	9.1 ± 1.4	0.102 ± 0.012	30.1 ± 6.3
	R(17e)	13.0709	650.5	210	1.3	-7.7 ± 0.3	6.5 ± 0.8	0.07 ± 0.006	16.3 ± 2.5
	R(18e)	13.0209	727	222	1.3	-8.7 ± 0.2	8.8 ± 0.6	0.09 ± 0.004	26.4 ± 2.5
	R(19e)	12.9713	807.8	234	1.3	-7.7 ± 0.4	7.7 ± 0.9	0.077 ± 0.007	20.1 ± 3.8
	R(20e)	12.9221	892.7	246	1.3	-9.4 ± 0.2	8.5 ± 0.7	0.062 ± 0.004	17.6 ± 2.5
	R(21e)	12.8734	981.9	258	1.4	-9.4 ± 0.4	8.3 ± 1	0.058 ± 0.005	16.3 ± 2.5
	R(23e)	12.7771	1172.9	282	1.4	-8.3 ± 0.3	8 ± 0.7	0.05 ± 0.003	13.8 ± 1.3
	R(24e)	12.7295	1274.8	294	1.4	-9.5 ± 0.5	7.3 ± 1.3	0.039 ± 0.005	10.0 ± 2.5
	R(25e)	12.6823	1381	306	1.4	-8.5 ± 0.3	7 ± 0.7	0.05 ± 0.004	12.6 ± 1.3
	R(27e)	12.5891	1605.8	330	1.4	-8.2 ± 0.3	6 ± 0.9	0.034 ± 0.003	7.5 ± 1.3
	R(29e)	12.4974	1847.6	354	1.5	-6.1 ± 0.7	9.1 ± 1.7	0.028 ± 0.004	8.8 ± 2.5
	R(30e)	12.4521	1974.8	366	1.5	-8 ± 0.8	5.8 ± 2.1	0.026 ± 0.007	6.3 ± 2.5
	R(31e)	12.4072	2106.2	378	1.5	-10.3 ± 1.0	7.5 ± 2.6	0.021 ± 0.005	5.0 ± 2.5
	R(32e)	12.3627	2241.7	390	1.5	-6.4 ± 1.0	8.6 ± 2.7	0.013 ± 0.003	3.8 ± 1.3
	R(33e)	12.3185	2381.6	402	1.5	-6.3 ± 0.8	8.4 ± 2	0.013 ± 0.002	3.8 ± 1.3
	R(34e)	12.2747	2525.5	414	1.5	-9.4 ± 0.6	8.5 ± 1.5	0.015 ± 0.002	5.0 ± 1.3
HCN ν_2 v_2=0-2	P(14)	7.2923	446.4	174	1.1	-13 ± 0.4	12.7 ± 1.2	0.083 ± 0.005	208.5 ± 22.6
	P(13)	7.2775	387	162	1.1	-11.2 ± 0.4	9.3 ± 1.2	0.063 ± 0.005	126.0 ± 16.3
	P(12)	7.2627	331.7	150	1.1	-11.2 ± 0.3	10.5 ± 0.7	0.078 ± 0.003	169.6 ± 12.6
	P(10)	7.2332	233.9	126	1.1	-10.9 ± 0.6	9.8 ± 1.5	0.076 ± 0.008	154.5 ± 27.6
	P(9)	7.2184	191.4	114	1.1	-10.9 ± 0.3	12.2 ± 1	0.074 ± 0.004	189.7 ± 17.6
	P(8)	7.2037	153.1	102	1.1	-10.9 ± 0.4	12.9 ± 1.9	0.078 ± 0.007	178.4 ± 27.6
	P(6)	7.1741	89.2	78	1.2	-11.8 ± 0.4	7.9 ± 1	0.092 ± 0.007	170.8 ± 21.4
	P(5)	7.1593	63.8	66	1.2	-11.1 ± 0.3	9.1 ± 0.9	0.059 ± 0.004	126.9 ± 13.8
	P(4)	7.1445	42.5	54	1.2	-12.4 ± 0.4	13 ± 0.2	0.069 ± 0.005	197.2 ± 16.3
	P(3)	7.1297	25.5	42	1.3	-11 ± 0.6	13 ± 1.5	0.05 ± 0.004	152.0 ± 21.4
	P(2)	7.1148	12.7	30	1.4	-10.3 ± 0.8	10.6 ± 2	0.046 ± 0.006	124.3 ± 27.6
	R(0)	7.0702	0	6	0.7	-22.2 ± 0.5	5.5 ± 1.2	0.083 ± 0.01	59.0 ± 10.0
	R(2)	7.0404	12.7	30	0.9	-11.3 ± 0.9	10.1 ± 2.8	0.078 ± 0.014	139.4 ± 41.4
	R(4)	7.0106	42.5	54	1	-11.7 ± 0.4	11 ± 0.9	0.102 ± 0.006	207.2 ± 1.6
	R(5)	6.9956	63.8	66	1	-11.1 ± 0.7	13 ± 2.3	0.06 ± 0.018	147.0 ± 46.5
	R(8)	6.9509	153.1	102	1.1	-9.8 ± 0.4	5.5 ± 0.4	0.095 ± 0.009	129.4 ± 15.1
	R(9)	6.936	191.4	114	1.1	-12.7 ± 0.4	13 ± 0.5	0.08 ± 0.009	204.7 ± 25.1
	R(10)	6.9211	233.9	126	1.1	-12.9 ± 0.5	8.8 ± 1.3	0.079 ± 0.007	148.2 ± 22.6
	R(12)	6.8914	331.7	150	1.1	-13.6 ± 0.4	11.7 ± 1.2	0.096 ± 0.007	222.3 ± 25.1
	R(13)	6.8766	387	162	1.1	-13.8 ± 0.8	10.8 ± 2.6	0.067 ± 0.01	149.5 ± 36.4
	R(14)	6.8619	446.4	174	1.1	-12.6 ± 0.7	9.2 ± 1.8	0.08 ± 0.011	162.0 ± 35.2
	R(15)	6.8472	510.3	186	1.1	-11.1 ± 0.6	13 ± 0.7	0.083 ± 0.007	218.5 ± 26.4
HCN ν_1 v= 0 − 1	P(18)	3.0721	727.0	222	40.9	-9.2±0.9	4.6±2.4	0.008±0.003	–
	P(17)	3.0690	650.5	210	41.0	-9.9±0.8	4.6±0.8	0.012±0.003	–
	P(16)	3.0659	578.2	198	41.2	-9.8±0.6	4.6±0.5	0.014±0.005	–
	P(14)	3.0598	446.4	174	41.5	-9.6±0.2	5.9±0.6	0.022±0.002	–
	P(13)	3.0568	387.0	162	41.7	-9.0±0.5	5.5±1.2	0.022±0.003	–
	P(12)	3.0538	331.7	150	41.9	-9.4±0.3	5.9±0.7	0.029±0.002	–

Table 4. continued.

Species	Transition	λ (μm)	E_l (K)	g_l	A_{ij} (s^{-1})	v_{lsr} (kms^{-1})	Δv (kms^{-1})	τ_0	N_l/N_H ($\times 10^{-7}$)
	P(11)	3.0508	280.6	138	42.2	-10.4±0.5	7.3±1.3	0.025±0.003	–
	P(10)	3.0479	233.9	126	42.5	-9.6±0.2	5.3±0.6	0.026±0.002	–
	P(8)	3.0421	153.1	102	43.1	-9.3±0.3	7.9±0.8	0.034±0.003	–
	P(6)	3.0363	89.2	78	44.3	-10.3±0.6	9.9±1.5	0.029±0.003	–
	P(4)	3.0307	42.5	54	46.5	-9.8±0.4	8.7±1.0	0.029±0.002	–
	P(3)	3.0280	25.5	42	48.9	-10.1±0.2	5.3±0.5	0.028±0.002	–
	P(2)	3.0252	12.7	30	54.4	-9.1±0.6	6.1±1.6	0.016±0.003	–
	R(0)	3.0171	0.0	6	27.3	-10.2±0.7	4.6±1.5	0.013±0.003	–
	R(3)	3.0092	25.5	42	36.5	-8.8±0.2	6.5±0.6	0.035±0.002	–
	R(5)	3.0041	63.8	66	38.0	-8.4±0.2	5.0±0.5	0.045±0.003	–
	R(6)	3.0016	89.2	78	38.5	-9.8±0.2	6.3±0.5	0.024±0.001	–
	R(8)	2.9966	153.1	102	39.1	-10.6±0.6	8.5±1.6	0.038 ±0.005	–
	R(11)	2.9893	280.6	138	39.7	-9.5±0.4	6.7±1.1	0.015±0.002	–
	R(13)	2.9845	387.0	162	40.0	-10.6±0.8	11.1±0.5	0.022±0.004	–
p-C_2H_2 ν_5	R(10e)	13.245	186.2	21	3.5	-9.8 ± 0.3	8.4 ± 0.9	0.079 ± 0.006	7.9 ± 1.0
	R(12e)	13.1632	264.1	25	3.5	-10 ± 0.4	9.6 ± 1.1	0.073 ± 0.006	8.8 ± 1.3
	R(14e)	13.0825	355.5	29	3.6	-8.4 ± 0.3	7.9 ± 0.8	0.072 ± 0.006	8.3 ± 1.0
	R(16e)	13.0028	460.4	33	3.6	-7.7 ± 0.3	5.1 ± 0.8	0.06 ± 0.006	4.9 ± 0.8
	R(20e)	12.8466	710.8	41	3.8	-10 ± 0.5	7.3 ± 1.3	0.038 ± 0.005	4.6 ± 0.8
	R(22e)	12.77	856.2	45	3.9	-8.1 ± 0.3	6.8 ± 0.8	0.047 ± 0.003	4.1 ± 0.5
	R(24e)	12.6944	1015.2	49	3.9	-7.6 ± 0.4	7.4 ± 1.2	0.039 ± 0.004	4.1 ± 0.6
	R(26e)	12.6198	1187.6	53	4	-8.3 ± 0.5	9.4 ± 1.9	0.035 ± 0.005	4.3 ± 1.0
	R(28e)	12.5461	1373.4	57	4.1	-8.1 ± 0.5	9 ± 1.8	0.029 ± 0.004	2.6 ± 0.8
o-C_2H_2 ν_5	R(9e)	13.2862	152.3	57	3.5	-9.4 ± 0.9	6 ± 2.4	0.106 ± 0.027	7.5 ± 2.5
	R(11e)	13.2039	223.4	69	3.5	-9.9 ± 0.8	7.9 ± 3.1	0.083 ± 0.02	7.5 ± 2.5
	R(13e)	13.1227	308	81	3.6	-9.8 ± 0.3	9.6 ± 0.7	0.132 ± 0.007	13.8 ± 1.3
	R(15e)	13.0425	406.3	93	3.6	-10 ± 0.2	9.6 ± 0.5	0.133 ± 0.005	13.8 ± 1.0
	R(17e)	12.9634	517.9	105	3.7	-9.9 ± 0.3	8.8 ± 0.8	0.108 ± 0.007	10.0 ± 1.1
	R(19e)	12.8853	643	117	3.7	-9.3 ± 0.3	9 ± 0.7	0.102 ± 0.006	10.0 ± 1.1
	R(21e)	12.8082	781.7	129	3.8	-9.4 ± 0.2	10.5 ± 0.6	0.085 ± 0.004	10.0 ± 0.8
	R(23e)	12.7321	934	141	3.9	-9.1 ± 0.2	8 ± 0.5	0.072 ± 0.003	6.3 ± 0.5
	R(25e)	12.657	1099.6	153	4	-8.8 ± 0.3	7.4 ± 0.7	0.061 ± 0.004	5.0 ± 0.6
	R(27e)	12.5828	1278.8	165	4.1	-8.7 ± 0.8	11.9 ± 2.1	0.057 ± 0.007	7.5 ± 0.1
	R(29e)	12.5097	1471.4	177	4.2	-7.2 ± 0.5	8.2 ± 1.3	0.038 ± 0.004	3.8 ± 0.8
	R(31e)	12.4374	1677.5	189	4.3	-8.1 ± 0.5	8.5 ± 1.2	0.033 ± 0.003	3.8 ± 0.6
	R(33e)	12.3661	1896.9	201	4.4	-7.8 ± 0.5	7.9 ± 1.3	0.025 ± 0.003	2.5 ± 0.5
	R(35e)	12.2958	2129.8	213	4.5	-9.5 ± 0.6	8.9 ± 1.5	0.017 ± 0.002	1.3 ± 0.4
	R(37e)	12.2263	2376.1	225	4.6	-7 ± 0.8	8.1 ± 2.1	0.018 ± 0.003	1.3 ± 0.6
o-C_2H_2 $2\nu_5 - \nu_5$	R(10e)	13.2341	1235.5	63	3.6	-9 ± 0.6	8.5 ± 1.8	0.061 ± 0.009	4.6 ± 1.1
	R(11f)	13.2028	1273.6	69	4.1	-9.6 ± 0.7	7.4 ± 1.9	0.047 ± 0.008	4.4 ± 1.0
	R(12e)	13.1479	1313.4	75	3.3	-8 ± 1.2	6 ± 2.5	0.026 ± 0.019	2.9 ± 1.3
	R(14e)	13.0619	1404.7	87	3.1	-9 ± 0.4	9 ± 1	0.029 ± 0.002	4.8 ± 0.5
	R(15f)	13.0411	1457.1	93	4.1	-9.2 ± 0.4	9.6 ± 1.1	0.045 ± 0.004	4.4 ± 0.6
	R(16e)	12.9761	1509.6	99	2.9	-7.5 ± 0.5	9.9 ± 1.3	0.026 ± 0.003	4.6 ± 0.8
	R(17f)	12.9619	1569.2	105	4.1	-8.1 ± 0.4	7.7 ± 1.1	0.033 ± 0.003	2.8 ± 0.5
	R(19f)	12.8838	1694.9	117	4.2	-8.3 ± 0.5	10.2 ± 2	0.031 ± 0.004	2.6 ± 0.8

Table 4. continued.

Species	Transition	λ (μm)	E_l (K)	g_l	A_{ij} (s^{-1})	v_{lsr} (kms^{-1})	Δv (kms^{-1})	τ_0	N_l/N_H ($\times 10^{-7}$)
	R(21f)	12.8066	1834	129	4.3	-8.3 ± 0.3	7.4 ± 1	0.029 ± 0.003	2.8 ± 0.4
	R(23f)	12.7305	1986.9	141	4.4	-7 ± 0.4	8.4 ± 1.1	0.022 ± 0.002	2.3 ± 0.4
	R(25f)	12.6555	2153.1	153	4.5	-8 ± 0.6	8.3 ± 1.6	0.029 ± 0.004	3.0 ± 0.6
	R(27f)	12.5814	2333	165	4.6	-9.9 ± 1.3	8.3 ± 3.4	0.028 ± 0.008	2.5 ± 1.3
p-C_2H_2 $(\nu_4+\nu_5)^2-\nu_4^1$	R(11f)	13.1697	1104.4	23	2.2	-6.3 ± 0.6	6.7 ± 1.8	0.027 ± 0.005	3.8 ± 1.3
	R(14e)	13.0289	1235.3	29	1.8	-12.8 ± 1.1	5.8 ± 2.7	0.019 ± 0.006	2.5 ± 1.3
	R(16e)	12.9437	1340.1	33	1.7	-10.6 ± 1	9.7 ± 2.8	0.017 ± 0.004	3.8 ± 1.3
	R(17f)	12.9311	1399.8	35	2.3	-7.4 ± 0.6	6.3 ± 1.6	0.02 ± 0.004	3.1 ± 0.9
	R(23f)	12.7022	1817.3	47	2.6	-9.7 ± 0.7	8 ± 2.1	0.017 ± 0.003	3.3 ± 0.9
o-C_2H_2 $(\nu_4+\nu_5)^2-\nu_4^1$	R(10f)	13.2104	1067.1	63	2.2	-9.2 ± 0.9	10.4 ± 2.5	0.056 ± 0.01	10.0 ± 3.8
	R(11e)	13.157	1103.5	69	1.9	-8.2 ± 0.5	10.4 ± 1.3	0.043 ± 0.004	10.0 ± 1.3
	R(12f)	13.1292	1145.3	75	2.2	-9 ± 0.8	11.9 ± 2.6	0.052 ± 0.008	7.5 ± 2.5
	R(13e)	13.0715	1188	81	1.8	-6.7 ± 0.4	6 ± 1.5	0.029 ± 0.004	5.0 ± 1.3
	R(17e)	12.9012	1397.5	105	1.7	-8.5 ± 0.4	6 ± 0.5	0.04 ± 0.009	7.5 ± 1.3
	R(19e)	12.8162	1522.6	117	1.6	-7.3 ± 0.3	9.9 ± 1	0.031 ± 0.002	7.7 ± 1.1
	R(20f)	12.8155	1593.4	123	2.4	-8.3 ± 0.5	7.2 ± 1.7	0.039 ± 0.006	5.0 ± 1.3
C_2H_2 $\nu_2+(\nu_4+\nu_5)$	P(17e)	3.0857	517.9	105	26.1	-7.1±0.9	7.8±2.2	0.014±0.003	–
	P(15e)	3.0810	406.3	93	25.9	-7.6±0.3	2.5±0.8	0.019±0.003	–
	P(13e)	3.0763	308.1	81	25.7	-7.2±0.7	5.4±1.7	0.012±0.003	–
	P(11e)	3.0717	223.5	69	25.6	-7.8±0.4	5.0±1.1	0.016±0.002	–
	P(5e)	3.0581	50.8	33	26.4	-7.1±0.4	4.2±1.0	0.012±0.002	–
	R(1e)	3.0427	3.4	9	18.9	-7.4±0.4	2.5±1.0	0.011±0.003	–
	R(11e)	3.0216	223.5	69	23.2	-7.9±0.3	3.7±1.2	0.019±0.003	–
	R(13e)	3.0176	308.1	81	23.5	-6.9±0.4	2.8±1.0	0.019±0.004	–
p-NH_3 ν_2 v_2=0-1	sP(8,2) E' E'	12.3805	1002.5	102	4.6	-6.9 ± 0.7	7.8 ± 1.7	0.024 ± 0.004	2.6 ± 0.9
	s(8,1) E" E"	12.3782	1018	102	4.8	-6.7 ± 0.9	6.2 ± 2.4	0.015 ± 0.004	1.6 ± 0.8
	aP(6,4) E' E"	12.3107	514.3	78	3.1	-8.4 ± 0.5	6.3 ± 1.2	0.02 ± 0.003	4.1 ± 0.8
	aP(6,1) E" E'	12.2491	593.5	78	5.4	-6 ± 0.3	4.5 ± 0.5	0.039 ± 0.006	3.3 ± 0.5
o-NH_3 ν_2 v_2=0-1	aP(8,3) A1" A2'	12.8487	977.2	204	4	-6.4 ± 0.4	6.1 ± 1.1	0.028 ± 0.003	2.8 ± 0.6
	aP(8,0) A1' A2"	12.8112	1023.9	204	4.7	-6.7 ± 0.2	9.5 ± 0.7	0.032 ± 0.002	3.9 ± 0.4
	aP(6,3) A1" A2'	12.2814	551.3	156	4.2	-9.4 ± 0.4	8.5 ± 1.1	0.033 ± 0.003	5.7 ± 0.9
	aP(6,0) A1' A2"	12.2451	598.7	156	5.5	-7.3 ± 0.5	7.2 ± 1.4	0.044 ± 0.006	4.4 ± 1.1

Table 5. Line Parameters for AFGL 2136. E_l is the energy of the lower level of the transition, g_l is the statistical weight of the lower level, A_{ij} is the Einstein A coefficient of the transition, v_{lsr} is the centroid velocity of the line, Δv is the FWHM of the line, τ_0 is the optical depth at line centre and N_l/N_H is the abundance in the lower level of the transition. Line data were taken from the HITRAN database (Gordon et al. 2017).

Species	Transition	λ (μm)	E_l (K)	g_l	A_{ij} (s^{-1})	v_{lsr} (kms^{-1})	Δv (kms^{-1})	τ_0	N_l/N_H ($\times 10^{-7}$)
$C^{18}O$ v=0-1	P(2)	4.7967	15.7	5	21.3	22.6 ± 0.1	2 ± 0.2	0.218 ± 0.01	37.7 ± 2.5
	P(1)	4.7882	5.2	3	32.2	22.1 ± 0.1	2.4 ± 0.2	0.167 ± 0.007	25.1 ± 2.5
	R(0)	4.7716	0	1	10.8	22.1 ± 0.1	2.8 ± 0.3	0.265 ± 0.015	16.3 ± 1.3
	R(3)	4.7473	31.5	7	14.7	21.9 ± 0.2	3 ± 0.5	0.198 ± 0.017	23.9 ± 3.8
	R(4)	4.7395	52.7	9	15.1	22.5 ± 0.2	1.6 ± 0.5	0.178 ± 0.019	17.6 ± 2.5
	R(5)	4.7317	79	11	15.4	22.2 ± 0.3	2.5 ± 0.8	0.151 ± 0.022	17.6 ± 3.8

Table 5. continued.

Species	Transition	λ (μm)	E_l (K)	g_l	A_{ij} (s^{-1})	v_{lsr} (kms^{-1})	Δv (kms^{-1})	τ_0	N_l/N_H ($\times 10^{-7}$)
	P(17)	4.9369	805.5	35	15.1	27.2 ± 0.3	11.2 ± 1	0.054 ± 0.003	18.8 ± 2.5
	P(15)	4.9168	631.9	31	15.4	27.1 ± 0.2	11.3 ± 0.7	0.061 ± 0.002	21.4 ± 1.3
	P(12)	4.8874	410.7	25	15.8	26.8 ± 0.7	12.8 ± 2.3	0.075 ± 0.009	30.1 ± 6.3
	R(6)	4.724	110.5	13	15.7	26.3 ± 0.4	9.8 ± 1.2	0.11 ± 0.009	30.1 ± 3.8
	R(11)	4.6872	347.6	23	16.5	25.9 ± 0.3	13 ± 1	0.09 ± 0.005	32.7 ± 2.5
	R(12)	4.6801	410.7	25	16.7	25.8 ± 0.7	14.3 ± 0.7	0.117 ± 0.028	47.7 ± 11.3
	R(14)	4.6662	552.9	29	16.9	27.3 ± 0.2	13.1 ± 0.8	0.08 ± 0.003	28.9 ± 2.5
	R(15)	4.6594	631.9	31	17	26.3 ± 0.1	10.9 ± 0.7	0.058 ± 0.002	15.1 ± 1.3
	R(16)	4.6527	716.1	33	17.1	27.8 ± 0.4	11.4 ± 1.1	0.06 ± 0.004	20.1 ± 2.5
	R(17)	4.6461	805.5	35	17.2	28.1 ± 0.3	11.8 ± 1.1	0.056 ± 0.003	18.8 ± 2.5
	R(18)	4.6396	900.2	37	17.3	30 ± 0.6	14.3 ± 0.8	0.046 ± 0.007	18.8 ± 2.5
	R(20)	4.6268	1105.3	41	17.5	27.8 ± 0.4	10.7 ± 1.3	0.038 ± 0.003	11.3 ± 1.3
	R(21)	4.6206	1215.6	43	17.6	27.5 ± 0.2	10.2 ± 0.7	0.034 ± 0.001	10.0 ± 1.3
	R(22)	4.6145	1331.2	45	17.7	28 ± 0.3	11.1 ± 1	0.025 ± 0.001	7.5 ± 1.3
^{12}CO v=1-2	P(19)	4.9054	4124.8	39	31.4	26.2 ± 0.2	13.4 ± 0.6	0.165 ± 0.005	36.4 ± 2.5
	P(18)	4.8948	4020.9	37	31.7	27 ± 0.3	12.6 ± 0.7	0.163 ± 0.006	25.2 ± 2.5
	P(17)	4.8843	3922.5	35	31.9	27.1 ± 0.1	11.1 ± 0.4	0.171 ± 0.004	31.4 ± 1.3
	P(16)	4.8739	3829.4	33	32.2	27.6 ± 0.2	11.8 ± 0.7	0.17 ± 0.006	33.9 ± 2.5
	P(15)	4.8637	3741.9	31	32.5	27.6 ± 0.2	12.8 ± 0.7	0.181 ± 0.006	38.9 ± 2.5
	P(8)	4.7954	3281.8	17	34.9	27.2 ± 0.2	11.7 ± 0.5	0.213 ± 0.006	41.1 ± 2.5
	P(7)	4.7861	3237.9	15	35.5	27.3 ± 0.3	11.7 ± 1	0.227 ± 0.012	44.0 ± 3.8
	P(5)	4.7678	3166.7	11	37	28 ± 0.3	12 ± 0.9	0.189 ± 0.01	42.7 ± 3.8
	P(4)	4.7589	3139.2	9	38.3	27.5 ± 0.4	10.6 ± 1	0.18 ± 0.011	35.2 ± 3.8
	P(3)	4.75	3117.3	7	40.5	28 ± 0.6	14.6 ± 1.7	0.133 ± 0.01	36.4 ± 5.0
	P(2)	4.7413	3100.9	5	45.2	27.8 ± 0.3	6.6 ± 0.7	0.129 ± 0.009	18.8 ± 2.5
	P(1)	4.7327	3089.8	3	68.2	27.1 ± 0.2	9.7 ± 0.5	0.063 ± 0.002	16.3 ± 1.3
	R(4)	4.6832	3139.2	9	32	27.8 ± 0.3	12.3 ± 0.9	0.195 ± 0.009	35.2 ± 2.5
	R(5)	4.6753	3166.7	11	32.7	27.1 ± 0.1	13 ± 0.4	0.222 ± 0.004	40.2 ± 1.3
	R(6)	4.6675	3199.5	13	33.2	26.7 ± 0.2	14 ± 0.5	0.234 ± 0.006	46.5 ± 2.5
	R(7)	4.6598	3237.9	15	33.7	28.4 ± 0.3	12.8 ± 0.9	0.223 ± 0.01	40.2 ± 3.8
	R(8)	4.6523	3281.8	17	34.1	27.2 ± 0.2	12.1 ± 0.5	0.227 ± 0.006	40.2 ± 2.5
	R(12)	4.623	3511.9	25	35.3	27.4 ± 0.4	11.7 ± 0.9	0.246 ± 0.013	41.5 ± 3.8
	R(12)	4.616	3583	27	35.6	27.5 ± 0.2	12.6 ± 0.5	0.215 ± 0.006	40.2 ± 1.3
	R(16)	4.5954	3829.4	33	36.3	28.3 ± 0.4	10.7 ± 1.2	0.191 ± 0.015	32.7 ± 3.8
	R(17)	4.5887	3922.5	35	36.6	28.1 ± 0.2	13 ± 0.5	0.192 ± 0.005	37.7 ± 1.3
	P(24)	4.9603	4726.1	49	30.3	26.5 ± 0.2	9.3 ± 0.4	0.103 ± 0.003	17.6 ± 1.3
	P(25)	4.9716	4862.7	51	30.1	27 ± 0.3	11.4 ± 0.8	0.08 ± 0.004	16.3 ± 1.3
	P(26)	4.9831	5004.6	53	29.8	27 ± 0.4	6.7 ± 0.9	0.07 ± 0.007	8.8 ± 1.3
	P(27)	4.9947	5151.9	55	29.6	26.9 ± 0.2	8.5 ± 0.6	0.064 ± 0.003	10.0 ± 1.3
	P(28)	5.0065	5304.8	57	29.4	26.2 ± 0.3	11.1 ± 0.9	0.065 ± 0.004	12.6 ± 1.3
CS v=0-1	R(2)	7.8309	7.1	5	6.9	25.7 ± 0.4	8 ± 1	0.037 ± 0.003	5.0 ± 1.0
	R(3)	7.8212	14.1	7	7.2	25.1 ± 0.5	8.7 ± 1.2	0.042 ± 0.004	6.3 ± 1.1
	R(4)	7.8116	23.5	9	7.4	25.2 ± 0.4	6.2 ± 1.1	0.044 ± 0.005	5.0 ± 1.3
	R(5)	7.802	35.3	11	7.6	25.4 ± 0.3	9.2 ± 0.8	0.057 ± 0.003	8.8 ± 1.0
	R(7)	7.7833	65.8	15	7.8	25.4 ± 0.2	8.2 ± 0.5	0.089 ± 0.003	12.6 ± 6.3
	R(8)	7.774	84.6	17	7.9	26.3 ± 0.1	7.7 ± 0.4	0.1 ± 0.003	13.8 ± 3.8

Table 5. continued.

Species	Transition	λ (μm)	E_l (K)	g_l	A_{ij} (s^{-1})	v_{lsr} (kms^{-1})	Δv (kms^{-1})	τ_0	N_l/N_H ($\times 10^{-7}$)
	R(10)	7.7559	129.2	21	8	26.5 ± 0.2	10.3 ± 0.5	0.112 ± 0.003	18.8 ± 6.3
	R(11)	7.7469	155.1	23	8.1	26 ± 0.3	10.3 ± 0.7	0.098 ± 0.004	16.3 ± 11.3
	R(23)	7.6467	648.5	47	8.8	25 ± 0.4	2 ± 1.1	0.059 ± 0.008	5.0 ± 0.4
	R(25)	7.6313	763.5	51	8.9	31.3 ± 1	8.6 ± 2.7	0.054 ± 0.011	7.5 ± 1.0
	R(26)	7.6237	824.5	53	8.9	27.3 ± 0.6	5.9 ± 1.6	0.053 ± 0.008	6.3 ± 0.3
	R(27)	7.6162	887.8	55	9	24.9 ± 0.5	6.5 ± 1.3	0.048 ± 0.005	6.3 ± 0.3
	R(31)	7.5871	1164.5	63	9.2	28.3 ± 0.5	4.9 ± 1.2	0.045 ± 0.006	5.0 ± 0.3
HCN ν_2 v_2=0-1	R(7e)	13.5941	119	90	1.2	26.4 ± 0.2	12.3 ± 0.7	0.155 ± 0.006	50.2 ± 3.8
	R(10e)	13.4326	233.9	126	1.2	26.3 ± 0.2	9.6 ± 0.6	0.151 ± 0.006	42.7 ± 2.5
	R(11e)	13.3796	280.6	138	1.2	26.5 ± 0.2	10.1 ± 0.6	0.156 ± 0.007	46.5 ± 3.8
	R(12e)	13.3271	331.7	150	1.2	25.3 ± 0.4	11.5 ± 1.5	0.117 ± 0.009	40.2 ± 6.3
	R(14e)	13.2233	446.4	174	1.3	27.8 ± 0.2	11.5 ± 0.6	0.145 ± 0.005	49.0 ± 2.5
	R(16e)	13.1213	578.2	198	1.3	26.7 ± 0.3	12.4 ± 0.9	0.166 ± 0.008	61.5 ± 5.0
	R(17e)	13.0709	650.5	210	1.3	27.7 ± 0.3	11.8 ± 0.8	0.106 ± 0.005	37.7 ± 2.5
	R(18e)	13.0209	727	222	1.3	27.6 ± 0.2	10.3 ± 0.5	0.121 ± 0.004	38.9 ± 2.5
	R(19e)	12.9713	807.8	234	1.3	28.2 ± 0.4	13 ± 1.2	0.085 ± 0.005	33.9 ± 3.8
	R(20e)	12.9221	892.7	246	1.3	28 ± 0.2	11.2 ± 0.6	0.079 ± 0.003	27.6 ± 1.3
	R(21e)	12.8734	981.9	258	1.4	27.2 ± 0.2	12.2 ± 0.7	0.083 ± 0.003	31.4 ± 2.5
	R(23e)	12.7771	1172.9	282	1.4	28 ± 0.2	11.6 ± 0.5	0.069 ± 0.002	25.1 ± 1.3
	R(24e)	12.7295	1274.8	294	1.4	26.5 ± 0.3	9.2 ± 0.9	0.048 ± 0.004	15.1 ± 1.3
	R(25e)	12.6823	1381	306	1.4	26.7 ± 0.2	9.7 ± 0.5	0.073 ± 0.003	22.6 ± 1.3
	R(26e)	12.6355	1491.2	318	1.4	26.5 ± 1	10.8 ± 2.7	0.036 ± 0.007	12.6 ± 3.8
HCN ν_2 v_2=0-2	P(16)	7.3219	578.2	198	1.1	27.2 ± 0.4	8.2 ± 1	0.073 ± 0.006	126.9 ± 18.8
	P(14)	7.2923	446.4	174	1.1	28.5 ± 0.3	10 ± 0.9	0.087 ± 0.005	170.8 ± 18.8
	P(13)	7.2775	387	162	1.1	25.3 ± 0.7	7.6 ± 0	0.07 ± 0.013	118.1 ± 20.1
	P(12)	7.2627	331.7	150	1.1	26.5 ± 0.3	10.8 ± 0.9	0.097 ± 0.005	207.2 ± 21.4
	P(11)	7.248	280.6	138	1.1	26.3 ± 0.5	9.9 ± 1.9	0.062 ± 0.007	118.1 ± 26.4
	P(10	7.2332	233.9	126	1.1	26.2 ± 0.6	9.4 ± 1.6	0.071 ± 0.008	133.1 ± 26.4
	P(9)	7.2184	191.4	114	1.1	25.5 ± 0.9	7.6 ± 2.8	0.068 ± 0.035	113.0 ± 71.6
	P(8)	7.2037	153.1	102	1.1	26.7 ± 0.4	8.3 ± 1	0.077 ± 0.006	136.9 ± 20.1
	P(6)	7.1741	89.2	78	1.2	25.2 ± 0.5	7.9 ± 1.1	0.064 ± 0.006	113.0 ± 20.1
	P(5)	7.1593	63.8	66	1.2	27.7 ± 0.4	8.8 ± 0.9	0.087 ± 0.006	169.6 ± 21.4
	P(4)	7.1445	42.5	54	1.2	27.3 ± 0.5	10.7 ± 1.4	0.069 ± 0.006	159.5 ± 26.4
	P(3)	7.1297	25.5	42	1.3	26.3 ± 0.4	7.6 ± 1.1	0.08 ± 0.008	149.5 ± 26.4
	P(2)	7.1148	12.7	30	1.4	26 ± 0.5	9.3 ± 1.3	0.054 ± 0.005	129.4 ± 21.4
	R(0)	7.0702	0	6	0.7	23.2 ± 0.5	7.8 ± 1.4	0.094 ± 0.011	76.6 ± 16.3
	R(2)	7.0404	12.7	30	0.9	25.8 ± 0.6	10.9 ± 2	0.086 ± 0.01	150.7 ± 32.7
	R(3)	7.0255	25.5	42	1	25.4 ± 0.3	10.6 ± 0.9	0.082 ± 0.005	149.5 ± 15.1
	R(5)	6.9956	63.8	66	1	26.7 ± 0.5	10.9 ± 3.3	0.063 ± 0.013	98.0 ± 36.4
	R(8)	6.9509	153.1	102	1.1	27.4 ± 0.4	7.7 ± 1.5	0.099 ± 0.011	153.2 ± 35.2
	R(9)	6.936	191.4	114	1.1	24.3 ± 0.4	9 ± 1	0.09 ± 0.006	162.0 ± 21.4
	R(10)	6.9211	233.9	126	1.1	28.2 ± 0.4	7.6 ± 1.3	0.082 ± 0.008	133.1 ± 26.4
	R(12)	6.8914	331.7	150	1.1	24.9 ± 0.7	9.6 ± 1.9	0.07 ± 0.009	135.6 ± 33.9
	R(13)	6.8766	387	162	1.1	24.5 ± 0.6	9.4 ± 2	0.089 ± 0.012	167.0 ± 42.7
	R(14)	6.8619	446.4	174	1.1	24.9 ± 0.6	7.6 ± 1.6	0.103 ± 0.014	173.3 ± 45.2
	R(15)	6.8472	510.3	186	1.1	26.4 ± 0.7	7.7 ± 3.5	0.078 ± 0.015	123.1 ± 61.5

Table 5. continued.

Species	Transition	λ (μm)	E_l (K)	g_l	A_{ij} (s^{-1})	v_{lsr} (kms^{-1})	Δv (kms^{-1})	τ_0	N_l/N_H ($\times 10^{-7}$)
	R(16)	6.8326	578.2	198	1.1	27.4 ± 0.6	7.6 ± 1.8	0.063 ± 0.009	108.0 ± 30.1
	R(17)	6.818	650.5	210	1.1	24.3 ± 1	8.2 ± 2.2	0.065 ± 0.014	116.8 ± 41.4
p-C_2H_2 ν_5	R(6e)	13.4118	71.1	13	3.4	25.4 ± 0.5	9.4 ± 1.5	0.131 ± 0.014	12.6 ± 2.5
	R(10e)	13.245	186.2	21	3.5	27 ± 0.2	11.4 ± 0.8	0.093 ± 0.004	11.3 ± 1.3
	R(12e)	13.1632	264.1	25	3.5	27 ± 0.2	11.6 ± 0.7	0.093 ± 0.004	11.3 ± 1.3
	R(14e)	13.0825	355.5	29	3.6	28.7 ± 0.4	11.4 ± 1.3	0.104 ± 0.008	12.6 ± 1.3
	R(16e)	13.0028	460.4	33	3.6	27.1 ± 0.2	10 ± 0.6	0.071 ± 0.003	10.0 ± 1.3
	R(24e)	12.6944	1015.2	49	3.9	26.4 ± 0.5	12.1 ± 1.5	0.052 ± 0.005	6.3 ± 1.3
o-C_2H_2 ν_5	Q(9e)	13.7069	152.4	57	6.1	25.8 ± 0.3	12.7 ± 1.1	0.221 ± 0.011	15.1 ± 1.3
	Q(21e)	13.6758	781.8	129	6.1	26 ± 0.4	13.3 ± 1.7	0.147 ± 0.012	11.3 ± 1.3
	R(11e)	13.2039	223.5	69	3.5	25 ± 0.9	9.6 ± 2.8	0.196 ± 0.037	20.1 ± 6.3
	R(13e)	13.1227	308.1	81	3.6	28.1 ± 0.2	11.2 ± 0.8	0.173 ± 0.008	20.1 ± 1.3
	R(15e)	13.0425	406.3	93	3.6	26.9 ± 0.2	11.9 ± 0.6	0.162 ± 0.006	20.1 ± 1.3
	R(17e)	12.9634	517.9	105	3.7	26.9 ± 0.1	12.3 ± 0.5	0.14 ± 0.003	17.6 ± 1.3
	R(19e)	12.8853	643.1	117	3.7	27.2 ± 0.1	11.4 ± 0.4	0.131 ± 0.003	15.1 ± 1.3
	R(21e)	12.8082	781.8	129	3.8	27.3 ± 0.2	10.4 ± 0.4	0.108 ± 0.003	12.6 ± 1.3
	R(23e)	12.7321	934	141	3.9	28.1 ± 0.1	10.9 ± 0.5	0.08 ± 0.002	10.0 ± 1.3
	R(25e)	12.657	1099.7	153	4	27.4 ± 0.1	10.4 ± 0.3	0.092 ± 0.002	10.0 ± 1.3
o-C_2H_2 $(2\nu_5 - \nu_5)$	R(6e)	13.4074	1120.4	39	4.1	26.3 ± 0.5	9.2 ± 2.2	0.035 ± 0.005	2.6 ± 0.8
	R(10e)	13.2341	1235.5	63	3.6	27.5 ± 0.5	9.9 ± 0.1	0.045 ± 0.007	6.7 ± 0.9
	R(14e)	13.0619	1404.7	87	3.1	25.5 ± 0.8	9.9 ± 0.9	0.019 ± 0.006	3.0 ± 1.0
	R(15f)	13.0411	1457.1	93	4.1	25.6 ± 0.3	4.6 ± 0.8	0.033 ± 0.004	3.3 ± 0.4
	R(16e)	12.9761	1509.6	99	2.9	27.6 ± 0.4	9.9 ± 0.5	0.03 ± 0.003	5.1 ± 0.6
	R(17f)	12.9619	1569.2	105	4.1	28.5 ± 0.5	10 ± 1.4	0.026 ± 0.003	2.8 ± 0.5
	R(19f)	12.8838	1694.9	117	4.2	24.9 ± 0.5	4.8 ± 1.3	0.022 ± 0.004	2.1 ± 0.4
	R(21f)	12.8066	1834	129	4.3	26.2 ± 0.6	7.8 ± 1.8	0.024 ± 0.004	2.8 ± 0.6
	R(23f)	12.7305	1986.9	141	4.4	27.2 ± 0.3	8.4 ± 1.1	0.024 ± 0.002	1.6 ± 0.3
	R(25f)	12.6555	2153.1	153	4.5	27 ± 0.4	8.3 ± 1.1	0.019 ± 0.002	1.4 ± 0.3
o-C_2H_2 $(\nu_4 + \nu_5)^2 - \nu_4^1$	R(6f)	13.3762	951.6	39	2.2	26.4 ± 0.2	7.9 ± 0.7	0.06 ± 0.004	5.5 ± 0.5
	R(9e)	13.2428	1032.4	57	2	27.3 ± 0.7	9.7 ± 1.8	0.035 ± 0.005	6.3 ± 1.3
	R(10f)	13.2104	1067.1	63	2.2	28.5 ± 0.7	8.1 ± 2	0.033 ± 0.006	4.5 ± 0.9
	R(11e)	13.157	1103.5	69	1.9	28 ± 0.6	8.9 ± 2.2	0.022 ± 0.003	0.5 ± 1.0
	R(14f)	13.0492	1236.9	87	2.2	25.9 ± 0.6	9.9 ± 1.6	0.025 ± 0.003	4.4 ± 0.6
	R(16f)	12.9702	1342.1	99	2.3	27.9 ± 0.6	4.3 ± 1.7	0.031 ± 0.007	2.8 ± 0.8
	R(18f)	12.8923	1461	111	2.3	28.6 ± 0.6	5.8 ± 1.6	0.033 ± 0.006	2.6 ± 0.8
o-C_2H_2 $(\nu_4 + \nu_5)^0 - \nu_4^1$	R(10f)	13.2493	1067.1	63	1.4	27.8 ± 0.8	4.7 ± 2.2	0.029 ± 0.008	5.0 ± 2.5
	R(16f)	13.007	1342.1	99	1.6	26.5 ± 0.4	9.4 ± 1.1	0.028 ± 0.002	7.9 ± 1.0
	R(18f)	12.9284	1461	111	1.6	28.6 ± 0.5	6.9 ± 1.3	0.018 ± 0.003	4.3 ± 09
	R(20f)	12.8509	1593.4	123	1.6	28.1 ± 0.4	9.5 ± 1.4	0.018 ± 0.002	5.5 ± 0.8
	R(22f)	12.7745	1739.3	135	1.6	26.9 ± 0.8	12.4 ± 3	0.012 ± 0.002	3.8 ± 1.3
	R(24f)	12.6991	1898.8	147	1.6	25.6 ± 0.7	8.2 ± 1.9	0.015 ± 0.003	4.5 ± 1.0
o-C_2H_2 $(\nu_4 + \nu_5)$	P(17e)	7.7579	517.9	105	2.1	25.1 ± 0.1	6.1 ± 0.4	0.121 ± 0.004	42.7 ± 2.5
	P(15e)	7.7308	406.3	93	2.1	25.3 ± 0.4	7.4 ± 1	0.054 ± 0.004	40.2 ± 6.3
	P(11e)	7.677	223.5	69	2.2	27.3 ± 0.3	10.4 ± 2.6	0.122 ± 0.026	50.2 ± 15.1
	P(5e)	7.5966	50.8	33	2.4	24.8 ± 0.3	11.2 ± 1	0.121 ± 0.007	130.6 ± 12.6
	P(3e)	7.5698	20.3	21	2.6	24.8 ± 0.3	11.8 ± 1.2	0.084 ± 0.006	104.2 ± 12.6

Table 5. continued.

Species	Transition	λ (μm)	E_l (K)	g_l	A_{ij} (s^{-1})	v_{lsr} (kms^{-1})	Δv (kms^{-1})	τ_0	N_l/N_H ($\times 10^{-7}$)
	R(7e)	7.423	94.8	45	2.1	24.8 ± 0.3	9.7 ± 1	0.113 ± 0.007	96.7 ± 11.3
	R(11e)	7.37	223.5	69	2.2	25.7 ± 1.4	6.7 ± 3.4	0.064 ± 0.02	41.4 ± 21.4
	R(13e)	7.3436	308.1	81	2.2	28.2 ± 0.2	5.6 ± 0.7	0.082 ± 0.005	50.2 ± 6.3
	R(15e)	7.3174	406.3	93	2.2	29.4 ± 0.5	7.1 ± 1.3	0.075 ± 0.008	52.8 ± 10.0
	R(17e)	7.2913	517.9	105	2.2	26.5 ± 0.5	7.7 ± 1.5	0.067 ± 0.008	51.5 ± 10.0
	R(19e)	7.2654	643.1	117	2.2	23.8 ± 0.6	10.4 ± 1.5	0.051 ± 0.005	47.3 ± 8.8
	R(21e)	7.2398	781.8	129	2.2	26.4 ± 0.7	5.6 ± 1.9	0.049 ± 0.009	31.4 ± 10.0
p-NH_3 ν_2 v_2=0-1	aP(7,4) E' E"	12.5906	713.5	90	3.4	29 ± 0.5	4.2 ± 1.4	0.025 ± 0.005	2.4 ± 0.6
	sP(8,5) E" E"	12.3956	892.5	102	3.0	29.5 ± 0.3	4.6 ± 0.9	0.021 ± 0.003	2.0 ± 0.1
	sP(8,4) E' E'	12.3894	939.8	102	3.7	28.5 ± 0.4	6.9 ± 1.1	0.024 ± 0.002	3.3 ± 0.4
	sP(8,1) E" E"	12.3782	1018	102	4.8	28.4 ± 0.4	5.1 ± 1.1	0.023 ± 0.003	2.3 ± 0.3
	aP(6,5) E" E'	12.35	466.7	78	1.7	28.8 ± 0.3	6.3 ± 0.9	0.03 ± 0.003	6.9 ± 0.9
	aP(6,4) E"E"	12.3107	514.3	78	3.1	28.3 ± 0.2	6.2 ± 0.4	0.043 ± 0.002	5.5 ± 0.4
	aP(6,2) E' 'E'	12.261	577.7	78	4.9	27.1 ± 0.5	7.8 ± 1.3	0.06 ± 0.007	5.4 ± 1.0
	aP(6,1) E" E'	12.2491	593.5	78	5.4	29.7 ± 0.2	6.6 ± 0.5	0.048 ± 0.002	4.5 ± 0.5
	sP(7,5) E" E"	12.094	665.2	90	2.7	28.3 ± 0.4	5.6 ± 1.0	0.026 ± 0.003	4.0 ± 0.6
	sP(7,4) E' E'	12.089	712.7	90	3.6	28.4 ± 0.4	7.3 ± 1.0	0.032 ± 0.003	4.5 ± 0.5
	sP(7,1) E" E"	12.0797	791.4	90	5.2	29.3 ± 0.5	7.9 ± 1.5	0.026 ± 0.003	3.1 ± 0.5
	aP(5,4) E' E"	12.0387	343.4	66	2.2	28.2 ± 0.3	5.8 ± 0.8	0.03 ± 0.003	6.0 ± 0.8
	aP(5,1) E" E'	11.9786	422.8	66	5.8	28.1 ± 0.2	7.7 ± 0.5	0.054 ± 0.003	4.9 ± 0.4
	sP(6,5) E" E"	11.8057	465.6	78	1.8	26.9 ± 0.6	5.8 ± 1.6	0.024 ± 0.004	5.1 ± 1.3
	sP(6,4) E' E'	11.8017	513.3	78	3.2	28.0 ± 0.5	6.6 ± 1.4	0.032 ± 0.004	4.3 ± 0.9
	sP(6,2) E' E'	11.7958	576.8	78	5.2	27.8 ± 0.4	5.7 ± 1.0	0.045 ± 0.005	4.5 ± 0.6
	sP(6,1) E" E"	11.7942	592.6	78	5.7	29.1 ± 0.3	5.6 ± 0.9	0.046 ± 0.005	3.0 ± 0.5
	aP(4,1) E" E'	11.7158	280.3	54	6.3	28.0 ± 0.1	7.6 ± 0.4	0.065 ± 0.002	5.8 ± 0.3
	sP(5,4) E' E	11.5271	342.2	66	2.3	30.6 ± 0.1	6.9 ± 0.5	0.031 ± 0.001	6.4 ± 0.5
	sP(5,2) E' E'	11.5224	406	66	5.3	27.4 ± 0.3	6.1 ± 0.8	0.039 ± 0.004	4.9 ± 0.5
	aP(3,2) E' E'	11.4714	150.1	42	4.2	32.5 ± 0.3	4.3 ± 0.7	0.035 ± 0.003	4.1 ± 0.5
	aP(3,1) E" E'	11.4604	166.1	42	6.7	28.4 ± 0.2	7.6 ± 0.6	0.043 ± 0.002	4.3 ± 0.4
	sP(4,2) E' E'	11.2613	263.4	54	5.2	26.0 ± 0.3	6.0 ± 0.8	0.038 ± 0.003	4.6 ± 0.5
	sP(4,1) E" E"	11.2603	279.3	54	6.5	25.0 ± 0.3	6.3 ± 0.7	0.04 ± 0.003	2.9 ± 0.4
	aP(2,1) E" E'	11.2122	80.4	30	6.7	24.4 ± 0.2	7.7 ± 0.6	0.041 ± 0.002	5.4 ± 0.4
	aQ(8,7) E" E'	10.7789	766.8	102	10.4	28.9 ± 0.5	7.7 ± 1.3	0.031 ± 0.004	1.6 ± 0.3
	sQ(2,1) E" E"	10.7732	79.3	30	6.9	26.4 ± 0.5	6.5 ± 1.4	0.032 ± 0.005	3.8 ± 0.9
	aQ(5,5) E" E'	10.7671	295.3	66	12.7	25.2 ± 0.5	6.6 ± 1.4	0.068 ± 0.009	3.4 ± 0.5
	aQ(4,4) E' E"	10.7539	200.5	54	12.2	27.6 ± 0.2	9.0 ± 0.7	0.079 ± 0.004	4.4 ± 0.3
	aQ(6,5) E" E'	10.7491	466.7	78	9.1	26.3 ± 0.6	10.0 ± 1.8	0.04 ± 0.005	3.6 ± 0.6
	aQ(5,4) E' E"	10.7391	343.4	66	8.1	27.1 ± 0.4	6.0 ± 1.2	0.043 ± 0.006	3.6 ± 0.5
	aQ(1,1) E" E'	10.7339	23.2	18	7.6	25.5 ± 0.4	8.9 ± 1.2	0.047 ± 0.004	4.3 ± 0.5
o-NH_3 ν_2 v_2=0-1	aP(7,3) A1" A2'	12.5607	750.4	180	4.2	29.0 ± 0.4	6.6 ± 1.2	0.062 ± 0.007	5.1 ± 1.0
	sP(8,3) A2" A2"	12.3843	976.3	204	4.2	30.2 ± 0.3	6.1 ± 0.8	0.047 ± 0.004	4.5 ± 0.5
	aP(6,3) A1" A2'	12.2814	551.3	156	4.2	27.6 ± 0.2	8.2 ± 0.5	0.067 ± 0.003	7.7 ± 0.6
	aP(6,0) A1' A2"	12.2451	598.7	156	5.5	28.6 ± 0.2	7.8 ± 0.4	0.074 ± 0.003	6.9 ± 0.4
	sP(7,6) A2' A2'	12.0997	606.7	180	1.4	28.6 ± 0.2	5.2 ± 0.6	0.03 ± 0.002	7.9 ± 0.8
	sP(7,3) A2" A2"	12.0848	749.5	180	4.4	27.8 ± 0.3	6.7 ± 0.7	0.047 ± 0.003	4.8 ± 0.5
	sP(7,0) A2' A2'	12.0791	796.6	180	5.3	28.6 ± 0.3	5.8 ± 1	0.045 ± 0.005	2.6 ± 0.1

Table 5. continued.

Species	Transition	λ (μm)	E_l (K)	g_l	A_{ij} (s^{-1})	v_{lsr} (kms^{-1})	Δv (kms^{-1})	τ_0	N_l/N_H ($\times 10^{-7}$)
	aP(5,3) A1" A2'	12.0101	380.5	132	3.9	27.8 ± 0.3	9.0 ± 0.8	0.069 ± 0.004	10.9 ± 1.0
	sP(6,3) A2" A2"	11.7983	550.5	156	4.4	28.2 ± 0.2	6.3 ± 0.4	0.061 ± 0.003	6.7 ± 0.4
	aP(4,0) A1' A2"	11.7121	285.7	108	6.6	27.5 ± 0.1	8.3 ± 0.4	0.101 ± 0.003	9.0 ± 0.5
	sP(5,3) A2" A2"	11.5245	379.5	132	4.1	31.7 ± 0.2	8.0 ± 0.5	0.052 ± 0.002	7.7 ± 0.5
	aP(4,3) A2" A1"	11.2628	236.7	108	3.0	25.3 ± 0.2	8.0 ± 0.7	0.049 ± 0.003	11.1 ± 1.0
	aP(2,0) A1' A2"	11.2088	85.8	60	8.9	24.5 ± 0.1	8.4 ± 0.4	0.065 ± 0.002	7.0 ± 0.4
	aQ(3,3) A1" A2?'	10.7439	123.5	84	11.4	24.8 ± 0.3	9.9 ± 1	0.086 ± 0.006	5.3 ± 0.5
	aQ(8,6) A1' A2"	10.7397	835.6	204	7.6	26.5 ± 1	9.8 ± 3.1	0.025 ± 0.006	3.6 ± 1.1
	aQ(4,3) A1" A2'	10.7322	237.7	108	6.8	27.6 ± 0.3	10.2 ± 0.8	0.067 ± 0.004	6.8 ± 0.6
	aQ(5,3) A1" A2'	10.7182	380.5	132	4.5	26.4 ± 0.4	10.6 ± 1.4	0.05 ± 0.004	8.0 ± 1.1